# SCANNING ACOUSTIC MICROSCOPY MODELING FOR MICROMECHANICAL MEASUREMENTS OF COMPLEX SUBSTRATES

BY

C2010
Orestes Marangos

Submitted to the graduate degree program in Civil, Environmental, and Architectural Engineering and the Graduate Faculty of the University of Kansas in partial fulfillment of the requirements for the degree of Doctor of Philosophy in Civil Engineering

Chairperson _____ Dr. Anil Misra

Committee Members _____
Dr. Paulette Spencer

_____
Dr. Craig Adams

_____
Dr. Sarah L. Kieweg

_____
Dr. Jie Han

_____
Dr. Robert L. Parsons

Date Defended: _____

The Dissertation Committee for Orestes Marangos certifies
that this is the approved version of the following dissertation:

SCANNING ACOUSTIC MICROSCOPY MODELING FOR MICROMECHANICAL MEASUREMENTS OF COMPLEX SUBSTRATES

Chairperson Dr. Anil Misra

Date Approved: _____

# ABSTRACT

The Scanning Acoustic Microscope (SAM) is a powerful tool for understanding the mechanical characteristics of substrates with micro-scale near-surface graded layers. To interpret the SAM results from such substrates, a theoretical model was developed that incorporated the interaction of focused ultrasonic field, with a substrate having a near-surface graded layer. The focused ultrasonic field model was formulated in terms of spherical wave expansions. The substrate wave propagation was computed with a multilayered stiffness method. The bridging between the two models was accomplished by utilizing the angular spectrum. A commercial SAM was used to characterize a dentin substrate subjected to acid-etching. Calibration and a homotopic measurement protocol were developed for data accuracy and meaningful data comparison from pre and post etching states. The reflection coefficients from the SAM measurement for the etched dentin exhibited frequency dependent attenuation. The developed theoretical model was successfully applied to explain the observed frequency dependent phenomenon.

# TABLE OF CONTENTS

# LIST OF FIGURES

# LIST OF TABLES

# ACKNOWLEDGEMENTS

I would like to express my deepest gratitude to my advisor and mentor Prof. Anil Misra, for his invaluable help and guidance throughout the course of this work. Also, I am greatly thankful to Prof. Paulette Spencer for her continuous support and for introducing me to the very intricate and fascinating world of dental materials. Also, I would like to thank Prof. Adams, Dr. Kieweg, Prof. Han and Dr. Parsons for serving as members of my committee, and for taking the time to share their comments that contributed to the final version of this dissertation. Special thanks to Prof. J. Lawrence Katz for introducing me to acoustic microscopy and for taking the time from his busy schedule to attend my dissertation defense. In addition, I would like to acknowledge the National Institutes of Health/National Institute of Dental and Craniofacial Research (NIH/NIDCR) for providing partial financial support for this work (DE014392 PI: P Spencer, R13 DK069504 PI: P Spencer).

Thank you to good friends and colleagues that have stood by me during these years. Thank you to Geraldine, for being by my side with encouragement and patience from the very beginning of my Ph. D studies. Finally, I would like to thank my mother for her endless and unconditional love, my father and brothers for their care and support.

# 1.0 INTRODUCTION

## 1.1 Background

Material science and many engineering applications rely heavily on experimental methods to quantitatively evaluate materials. Focus is set on experimental techniques that are non-destructive in nature, in the sense that they do not cause permanent alterations to the specimen examined. Such non-destructive techniques provide a unique ability to devise experimental protocols that involve a number of complementary evaluation techniques so that a more complete "picture" of a material may be formed. Scanning acoustic microscopy (SAM) is such a non-destructive technique that is sensitive to the mechanical properties of a material.

SAM appeared in the early 1970's (Lemons and Quate 1974) as a new research technique that could provide images of elastic properties of a substrate with spatial resolution comparable to that of optical instruments. Since then, it has received great attention and has been used in numerous applications for imaging as well as quantitative characterization (Briggs 1992). However, for biological materials scanning acoustic microscopy has been predominantly used for imaging, and quantitative efforts for measurement of elastic properties are scarce.

Elastic property characterization using acoustic microscopy is typically based upon surface acoustic wave velocity measurements. However, there are cases where the aperture of the acoustic objective does not favor the generation of leaky Rayleigh waves or any other type of surface waves from the specimen. In such cases one relies only on the reflected signal amplitude to recover the elastic properties of the material. Moreover, the bulk of SAM work has been carried out using either tone-burst or broadband excitation.

It is well-accepted that natural and engineered materials have varying structure and composition at different spatial scales which is responsible for how material properties manifest in experimental measurements. In order to observe a material property, we "probe" and measure the reaction. The observable property is thus intimately linked to the size of the "probe". For example, in acoustic microscopy, the probe is a focused acoustic field produced by a piezoelectric transducer/lens system. The spatial resolution of this probe is a function of the operating frequency and the lens dimensions. Consequently, the properties measured using SAM are strongly dependent upon the lens characteristics as well as the volume of material interrogated by the focused acoustic field. The ability to interrogate different material volumes allows for characterization of complex substrates with varying microstructures.

Complex substrates that possess microstructure are known to exhibit dissipative properties that manifest as a dispersion or spreading of acoustic pulses as they propagate through the thickness of a material (Ophir and Jaeger 1982). A related wave propagation phenomenon is the frequency dependence of reflection coefficients. However, since the reflection process involves interaction with a material volume with the dimensions comparable to an acoustic wavelength (wavelength in the coupling fluid for SAM), severe attenuation needs to occur in order for frequency dependence to be detected. For example, it has been shown that for viscoelastic polymeric materials, the frequency dependence of reflection coefficients becomes important as the contrast between the elastic reflection coefficients becomes small (Bourbie 1984). Significant attenuation in the reflection also occurs in the presence of roughness (Nagy and Adler 1987). Similar reflection phenomena are expected for substrates that have rapidly varying near-surface properties.

Many engineering applications require joining of materials through adhesive bonding. The interphases that the adhesives form with the materials, are thin (<100 micron) with significant spatial variations in material properties. Such interphases are of interest in biomedical engineering and particularly in dental composite restorations. In such restorations, the dentin substrate is acid-etched prior to adhesive application. The etching is expected to de-mineralize the dentin near-surface and expose the collagen into which the adhesive can infiltrate thus, producing an interphase. The etching, however, is a complex process that results in a transition zone to the native dentin through a graded partially de-mineralized layer. Therefore to understand the mechanical behavior of bond formed through this process it is critical to understand the properties of the etched layer.

## 1.2 Problem Statement

The problem driving this work is the characterization of the mechanical properties of the etched dentin near-surface layer. To understand the mechanical characteristics of the etched dentin layer, we use Scanning Acoustic Microscopy (SAM) where ultrasonic waves are focused to interrogate a specimen. We prefer SAM over more conventional indentation techniques because SAM is non-destructive and provides a range of spatial resolutions. Since small-amplitude waves are involved, the specimen is not affected by the measurement and it is preserved in its near natural state. In this way, we may subsequently subject the specimen to surface alterations, in this case etching, and directly observe the changes. Additionally, the same sample may be used in complementary destructive or non-destructive techniques to obtain physico/mechanical properties.

The determination of the mechanical properties of etched dentin with SAM requires proper interpretation. The ultrasonic wave-field that is received by the acoustic microscope's

objective includes the interactions with all materials and interfaces in its path. Therefore, in order to adequately interpret the ultrasonic signal, a theoretical model of the wave propagation process is required that describes the focused acoustic field and its reflection from the substrate. Acid etched dentin results in gradation of the near-surface material composition and properties. The relative contribution of these acid-etching induced microstructures to the received ultrasonic signals is not known. Moreover, the high resolution of SAM coupled with the complete transformation of the dentin near-surface after acid-etching, dictates that homotopic (same location) SAM measurements must be performed (Marangos et al 2009). Homotopic SAM measurements can provide useful information about the attenuation mechanisms at the etched-surface by utilizing acoustic fields of different wavelengths.

## 1.3 Objectives of the Study

In order to address the problem outlined above, the objectives were divided into two parts:

1. Theoretical Component – the theoretical component consists of the following 3 tasks:

*1) Modeling of focused ultrasonic field* –The outcome of this task will be a methodology for determining the focused ultrasonic field.

2) *Modeling of interaction of the ultrasonic field with a complex substrate* – The outcome of this task will be: (i) a model for wave propagation in the complex substrate, and (ii) a methodology for bridging the focused acoustic field determined in task 1 with the substrate model developed in task 2.

3) *Parametric studies to assess model capabilities* – The outcome of this task is to provide insight to the interaction of acoustics fields with near-surface graded layer.

2. Experimental component – the experimental component consists of the following 3 tasks:

*1) Calibration of SAM* – The outcome of this task will be a calibration methodology that separates the effects introduced by the instrument electronics from the material behavior and will include: (i) calibration curves and (ii) measurement error analysis.

*2) SAM measurement protocol* – The outcome of this task will be: (i) homotopic measurement device, (ii) specimen preparation protocol, (iii) data acquisition protocol, and (iv) data processing using custom developed software.

*3) Comparison of measured results with theoretical prediction* – The outcome of this task will be the interpretation of the measured data with the theoretical model.

## 1.4 Organization

The dissertation is organized in three chapters. Chapter 2 describes the results of the theoretical development, Chapter 3 describes the results of the experimental tasks as well the comparison of the experimental results and the theoretical model, and Chapter 4 includes a summary of the work accomplished and a synopsis of the main findings.

# 2.0 THEORY

## 2.1 Reflection scanning acoustic microscopy

### 2.1.1 Background

Scanning acoustic microscopy is the only non-destructive technique with the capability of measuring micro-scale mechanical properties of materials. A comprehensive review of acoustic microscopy is given in Briggs (1992). Here, we briefly describe the background and terminology that will be used in this dissertation. The principle of acoustic microscopy is quite simple in concept; mechanical waves are generated by a source and focused onto a specimen. One may then measure either the part of the signal that reflects from the specimen, hence the term reflection acoustic microscopy, or the part of the signal that transmits through the specimen, in which case the term transmission acoustic microscopy is used. Mechanical waves are generated by means of a piezoelectric transducer. The piezoelectric transducer when excited by an electrical potential, deforms and creates the mechanical waves. Acoustic microscopes may be classified into different types depending upon the location and shape of the piezoelectric element. In type I acoustic microscopes, the piezoelectric transducer is mounted at the end of cylindrical sapphire rod whose other end is shaped as a spherical surface as shown in Fig 2.1. The mechanical wave then propagates through the sapphire rod and interacts with the spherical surface, which acts as a lens, to create a converging wave-field in front of the lens where the specimen of interest is placed. In type II reflection microscopes, the piezoelectric element is

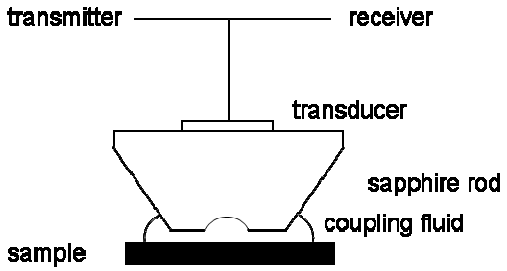


Figure 2.1 Reflection SAM setup

shaped as a concave surface in which case there is no need for additional buffer material. A coupling fluid, typically water, is required in order to facilitate ultrasound propagation from the lens to the specimen.

During SAM measurements, the specimen is typically immersed in a water or suitable coupling fluid bath. In reflection acoustic microscopy, which is the technique most relevant to this work, the ultrasonic field interacts with the near-surface of the material in question and part of it reflects back through the coupling medium to the lens. The lens redirects the field which, after travelling again through the sapphire rod, arrives at the piezoelectric transducer. The deformation of the piezoelectric element creates a potential difference which is amplified and displayed by an oscilloscope as a waveform. Such waveforms are called A-Scans. Typical A-

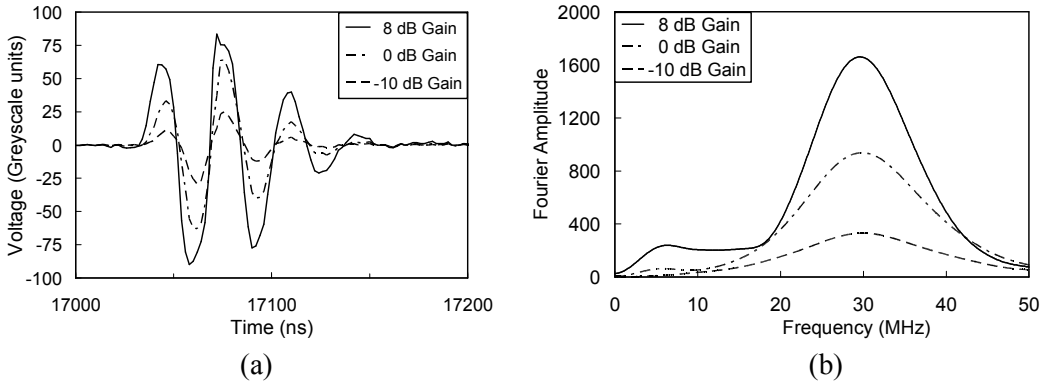


Figure 2.2 a) A-Scan and b) Fourier amplitude spectra

Scans are shown in Fig 2.2a and their Fourier amplitude spectra in Fig 2.2b for various amplification settings. The frequency content of the signal may be described by two parameters which is the central frequency and the bandwidth at the half-maximum amplitude (-6 dB). The central frequency parameter is always used by manufacturers to refer to a specific objective. The central frequency of an objective refers to the resonant frequency of the piezoelectric transducer.

However, it has been shown (Canumalla 1999) that water attenuates the higher frequencies and thus it is very likely that the central frequency of the received signal will be down-shifted.

The transducer and lens are located in the same housing which is termed the ultrasonic objective. In SAM, the objective is coupled with an x-y-z positioning system that enables raster scan over the specimen. As the objective is scanned over the specimen, an A-Scan signal is acquired for each scanned location and selected signal parameters may then be displayed as a grayscale image, termed a C-Scan.

### 2.1.2 Contrast Mechanism

The contrast in SAM images is generally related to the elastic properties and density of the substrate. However, the interaction of the wave-field with a specimen is usually quite complex and there are a number of waves that may be generated at the fluid-specimen interface that will contribute to the received signal amplitude. One such mechanism is based upon the generation of Rayleigh waves at the fluid-specimen interface and their constructive or destructive interference with the normally reflected ray as the objective is moved towards the specimen. This interference creates periodic fluctuations in the received voltage that vary as a function of depth. The wavelength of the oscillation corresponds to the Rayleigh wavelength. When such a measurement is taken at a single location the resulting curve is known as a V (z) curve. A C-Scan taken at various z-positions, provided that the substrate is isotropic, will

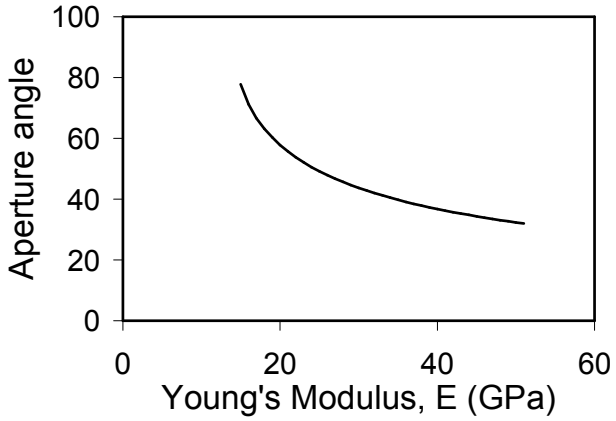

Figure 2.3 Relationship between lens aperture and elastic modulus

sometimes be dark and sometimes brighter. The generation of Rayleigh waves, however, depends on both the material properties of the substrate and the wave-field incident on the specimen which in turn depends on the aperture angle of the lens. This relationship is illustrated in Fig 2.3, where the substrate in an isotropic half-space. Points on the graph signify the smallest half-aperture angle $\alpha°$ at which Rayleigh waves will be generated for a specific Young's modulus value. The relationship immediately shows that for stiffer materials, Rayleigh waves are possible to be generated with smaller aperture lenses. For dentin, the reported elastic moduli do not exceed 30 GPa and practical issues make construction of lenses with half-aperture angles greater than 60° difficult. In relatively soft materials such as dentin and bone, there might be other waves that are generated such as the longitudinal surface skimming waves (LLCW). In the event that the lens aperture does not permit any surface wave generation, then only the specularly reflected longitudinal wave-field will be received by the transducer. In that case, a C-Scan image will be brightest when the specimen is placed at the focus.

## 2.2 Modeling Methodology

In order to develop theoretical models of the process of wave propagation in SAM, the following two-steps are followed: 1) determination of focused ultrasonic field, and 2) interaction of the ultrasonic field with a substrate and back-propagation of the reflected wave-field. From the viewpoint of describing the measured received signal, we consider the integral of the average reflected pressure field denoted by, $\overline{p}_{rec}$, which is expressed as:

$$\overline{p}_{rec}(\omega) = \int_{-a}^{a}\int_{-a}^{a}\left[\int_{-\infty}^{\infty}\int_{-\infty}^{\infty} P(k_x,k_y,z_0)R(k_x,k_y)e^{i(k_x x+k_y x)}e^{ik_z z_0}\,dk_x\,dk_y\right]dxdy \tag{2.1}$$

at a given frequency, ω, where $P(k_x, k_y, z_0)$ is the two-dimensional angular spectrum of the pressure field at the substrate-fluid interface ($z_0$) and $R(k_x, k_y)$ is the reflectance function of the substrate-water interface. The limits of the integral denote the integration over the surface of the receiving transducer. Thus, the determination of the angular spectrum of the focused pressure field and the reflectance function of the substrate-fluid interface form the two key problems of effective SAM modeling.

In the SAM modeling literature, a variety of approaches have been proposed for evaluating Eq 2.1. The approaches most frequently adopted are founded either on Fourier theory (Atalar 1978, Wikramasinghe 1979) or on ray theory (Bertoni 1984). Alternative approaches have also been proposed that include the finite element methods (Winkler and Davies, 1986 a, b), combination of the finite element and boundary element methods (Liu et al 1992), distributed point source methods (Kundu 2006) and frequency domain methods (Nagy and Adler 1990). More rigorous diffraction theories (Li et al 1991) and asymptotic approximations (Rebinsky and Harris 1992 a, b) have also been used. In addition, various substrates have also been modeled, such as anisotropic half-spaces (Somekh et al 1984), layered systems (Kundu et al 1985, Lee et al 1993), elastic discontinuities such as cracks (Ilett et al 1984) and rough surfaces (Pecorari and Briggs 1996, Li 1993). The theoretical foundations of these approaches have been developed more than a century ago in the fields of optics (Sommerfeld 1954, Born & Wolf 1999), acoustics and elastodynamics (Rayleigh 1945, Achenbach 1973). As seen from Eq 2.1, the evaluation of the reflected pressure field requires the computation of the angular spectrum and reflectance function. In general, these quantities can be computed independently. For angular spectrum calculation we require methods to obtain fields generated by concave transducers, while for the reflectance function we require wave propagation models appropriate to the substrate.

In recent years an alternative analytical approach for obtaining acoustic fields generated by concave transducers has been presented by Coulouvrat (1993). The computational effort required for this approach is significantly smaller than the numerical methods such as the finite element and the finite difference methods for results of similar accuracy. In addition, this approach has the advantage of the boundary element method in reducing the dimensionality of the problem, although the method does not rely on the Green's function which does not exist for concave geometries. Coulouvrat's method has not been widely applied since its appearance in 1993, however in the recent past the method has been used to evaluate the thermal effects of focused ultrasound on biological tissue due to the advantage this method offers over other numerical methods (Feng et al 2005).

Similarly, a number of approaches (too numerous to report here) have been discussed in the literature that can be applied to model complex substrates. This work considers substrates with strong near-surface heterogeneity in the normal direction to the surface. Substrates with such vertical inhomogeneities occur in various applications that include natural and engineered systems at both the large scale and the laboratory scale, such as in ocean bottom prospecting, near-surface earthquake wave propagation, etched surface characterization, osteoporotic bone characterization, and functionally graded material characterization (FGM). The approaches used to address these problems can be classified into 3 categories: (1) numerical simulation using finite difference or finite elements (Vollman et al 2006, Haiat et al 2009, Berezovski et al 2003, Zhang et al 2007), (2) analytical methods (Robins 1990, 1998) and (3) semi-analytical methods such as ray theory and multi-layer theory (Thomson 1950, Haskell 1953, Rokhlin 2004). For the type of problem we are addressing, the multi-layer theory with plane-wave propagation is most

attractive since they are relatively straightforward to implement and have a lower computational demand compared to the numerical simulations.

The bridging of the acoustic field model and the substrate model require further considerations since these methods are typically developed in different coordinate systems. The acoustic field solutions are represented as spherical wave expansions while the substrate solutions are represented as plane wave expansions. To couple the acoustic field solution with the substrate solution, therefore requires either plane wave representation of the acoustic field or vice versa. The approach adopted in this work uses angular spectrum representation of the computed acoustic field. This plane wave representation is then used to obtain the reflected field from the substrate model.

Finally, we note that Eq 2.1 is for a monochromatic wave, however, in the acoustic microscope relevant to this work the source (or the input signal) is a broad band pulse. To study these polychromatic (multi-frequency) waves, we consider the time dependence of the pressure field to be a synthesis of monochromatic functions as:

$$p(t) = \frac{1}{2\pi} \int_{-\infty}^{\infty} v(\omega) \overline{p}_{rec}(\omega) e^{-i\omega t} d\omega \qquad (2.2)$$

where v(ω) is frequency spectrum of the normal velocity, ω is the angular frequency, related to frequency by $\omega=2\pi f$ and the pressure is considered to have a harmonic time dependence to be $\exp(-i\omega t)$.

### 2.2.1 Determination of focused ultrasonic field

Several approximate theories have been used in scanning acoustic microscopy to model the field to account for the effects of focusing by the lens. In the majority of these works, the point of departure is the Rayleigh integral of the scalar theory of diffraction. This may be derived from

Green's identity and the fact that the ultrasonic scalar field must satisfy the Helmholtz equation (Baker and Copson 1987). The Rayleigh integral is written as:

$$v_P = \frac{1}{4\pi}\iint_S \left\{ \frac{e^{ikr}}{r}\frac{\partial v}{\partial n} - v\frac{\partial}{\partial n}\left(\frac{e^{ikr}}{r}\right)\right\} dS \tag{2.3}$$

where v is is the value of the pressure field on S, while v is the value of the pressure at an evaluation point P. Eq 2.3 allows us to evaluate the total field at a point P if we know the value of the field and its normal derivative on the boundary S, which is an spherical surface in the case of a spherically focused lens. In reality the boundary values in Eq 2.3 are not known and very often the Kirchhoff approximation is employed. However, it has been shown that the Kirchoff approximation does not correctly reproduce the assumed boundary conditions (Stamnes 1986). Alternatively, the Rayleigh-Sommerfeld integral may be used which only requires the value of the function on the boundary:

$$v_P(r) = \frac{1}{i\lambda}\iint_S v\left(\frac{e^{ikr}}{r}\right)\cos(n,r)dS \tag{2.4}$$

This approach is known to be an exact formulation of Huygens principle only for plane boundaries (Sommerfeld 1954). For curved boundaries, it is an approximation that assumes that the dimensions of the curvature are small compared to the wavelength in the medium. Under this assumption, the integral of Eq 2.4, represents a superposition of hemi-spherical wavelets that radiate independently. Stated in another way, the hemi-spherical wavelets are assumed not to suffer secondary diffraction because of the surface curvature. O'Neil (1949) used direct integration of Eq 2.4 to evaluate the acoustic fields from concave radiators. In SAM models based upon this approach, either the lens curvature was taken into account but not the exact boundary conditions (Li et al 1991, Ardebili 1995), or the lens surface is replaced by equivalent sources at the aperture plane (Liang et al 1985, Chou and Kino 1987, Lucas and Muir 1982,

Atalar 1978, Wickramasinghe 1979). In contrast to these above approaches, Coulouvrat's method takes into account secondary reflections from the lens curvature that are not captured by the Rayleigh integral. In addition, the exact boundary conditions on the baffle surface can be applied.

#### 2.2.1.1 Principle of Coulouvrat's method

The method presented by Coulouvrat (1993) and used in this dissertation, draws upon earlier work by Keller and Givoli (1989) for solution of acoustic scattering in unbounded domains. Typically, in such problems the Sommerfeld radiation condition must be satisfied at infinity. In addition, the numerical solution is facilitated by the introduction of an artificial boundary, separating the computational domain into an interior region and an exterior region. On the artificial boundary, a boundary condition is imposed such that waves are allowed through it without generating any spurious reflections. In this fashion, the computational domain is reduced to the interior domain, where it is possible to use interior numerical methods such as finite elements or finite differences to obtain a solution.

#### 2.2.1.2 Geometry, definitions and equations

The geometry of the problem is illustrated in Fig 2.4. The lens used to focus the ultrasonic field in acoustic microscopy may be viewed as an axially symmetric spherical cap, $\Gamma s$, mounted on an infinite plane baffle, $\Gamma_B$. The spherical cap is defined by the radius of curvature, R, and aperture angle, $\chi$, which measures the angular extent of the spherical surface. Point O is defined as the point on the spherical cap for which the inward surface normal is identical to the normal to the baffle surface. Point F is the geometrical focus, which is defined as the point of intersection of lines directed normally to the spherical surface. The line that contains points O and C is defined

as the acoustic axis z. Point C, which is the point of intersection between the acoustic axis and the baffle plane, is used as the origin of a cylindrical coordinate system (z, R) and a spherical coordinate system (r, θ). A hemisphere with surface $\Gamma_L$ centered at C and of radius *a*, separates domain Ω in two sub-domains, the interior sub-domain $\Omega_I$ and the exterior sub-domain

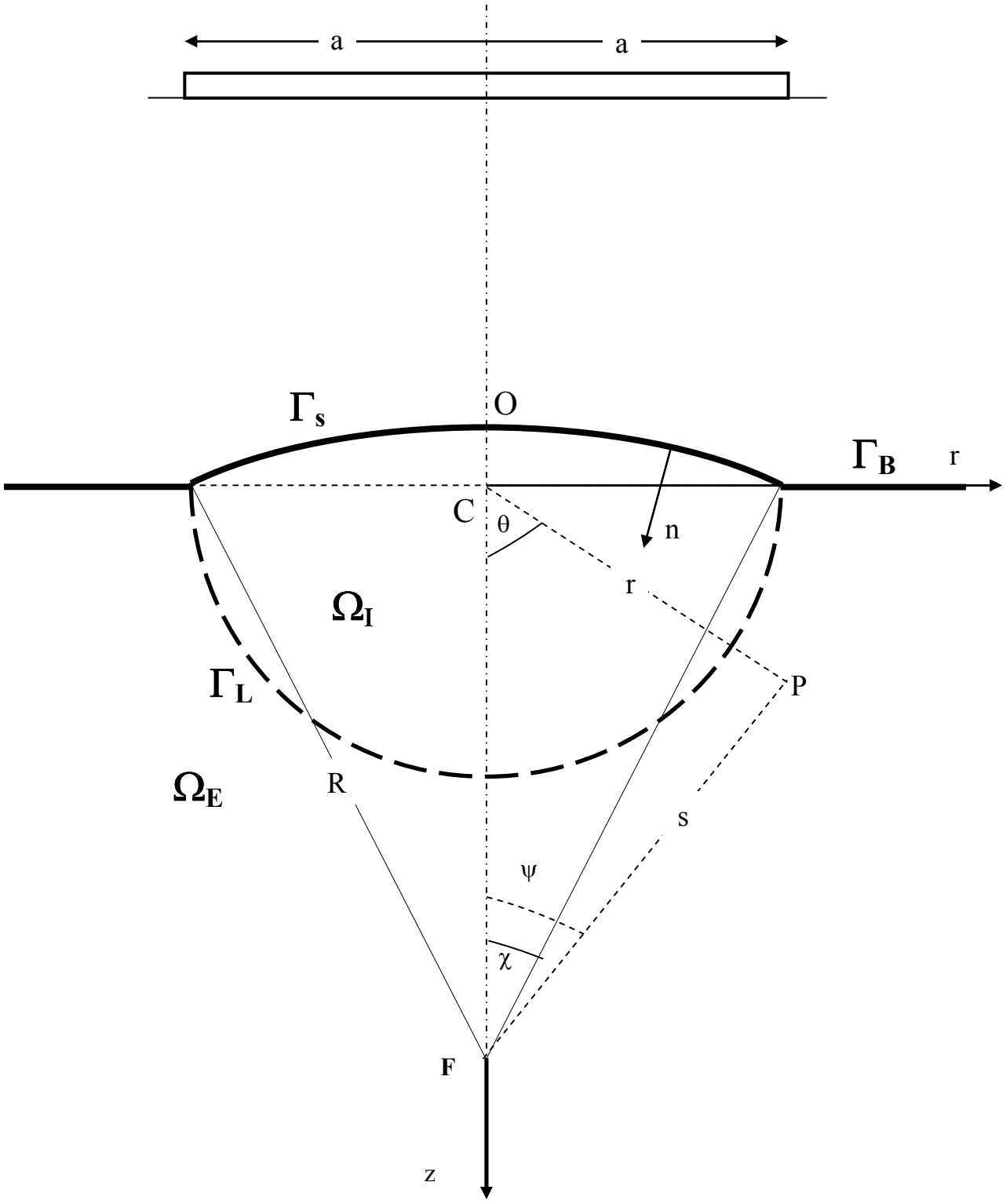


Figure 2.4 Problem geometry

$\Omega_E$. The fluid in domain $\Omega$ is considered to be homogeneous, isotropic and non-viscous with material density $\rho_f$ and sound velocity $v_f$. If small amplitudes are considered, non-linear effects may be neglected. Then, the pressure, p(r, θ, t), at any observation point P, satisfies the acoustic wave equation (Williams, 1999)

$$\nabla^2 p(r,\theta,t) - \frac{1}{v_f^{\,2}} \frac{\partial^2 p(r,\theta,t)}{\partial t^2} = 0 \tag{2.5}$$

Additionally, the particle velocity υ (r, θ, t) at P satisfies Euler's equation

$$\rho_f \frac{\partial \vec{\upsilon}(r,\theta,t)}{\partial t} = -\nabla p(r,\theta,t) \tag{2.6}$$

By considering harmonic time dependence for the pressure and velocity fields of the type $e^{(-i\omega t)}$ the well known scalar Helmholtz equation is obtained as:

$$\nabla^2 p(r,\theta,\omega) + k^2 p(r,\theta,\omega) = 0 \tag{2.7}$$

and Euler's equation

$$\nabla p(r,\theta,\omega) = i\omega\rho_f \vec{v}(r,\theta,\omega) \tag{2.8}$$

in the frequency domain where $k=\omega/v_f$ is the acoustic wavenumber. Solution of the Helmholtz equation (Eq 2.5) in spherical coordinates for the axi-symmetric geometry of the problem yields the pressure for the inner domain in terms of radial functions (spherical Bessel functions of first, $j_n$, and second kind, $y_n$) and Legendre polynomials,$P_n$, (Arfken and Webber, 2005):

$$p^{(i)} = \sum_{n=0}^{+\infty} b_n P_n(\cos\theta) j_n(kr) + \sum_{n=0}^{+\infty} c_n P_n(\cos\theta) y_n(kr) \qquad r \le a \tag{2.9a}$$

In the exterior domain the solution is written in terms of spherical Hankel functions of the first and second kind:

$$p^{(e)} = \sum_{n=0}^{+\infty} d_n P_n(\cos\theta) h_n^{(1)}(kr) + \sum_{n=0}^{+\infty} e_n P_n(\cos\theta) h_n^{(2)}(kr) \qquad r > a \tag{2.9b}$$

where the spherical Hankel functions are defined as:

$$h_n^{(1)}(kr) = j_n(kr) + iy_n(kr) \qquad (1^{st} \text{ kind}) \tag{2.10a}$$

$$h_n^{(2)}(kr) = j_n(kr) - iy_n(kr) \qquad (2^{nd} \text{ kind}) \tag{2.10b}$$

and

$$j_n(kr) = \sqrt{\frac{\pi}{2kr}} J_{n+\frac{1}{2}}(kr) \tag{2.10c}$$

$$y_n(kr) = \sqrt{\frac{\pi}{2kr}} Y_{n+\frac{1}{2}}(kr) \tag{2.10d}$$

where J and Y are the ordinary Bessel functions of 1st and and 2nd kind, respectively. The solution to Helmholtz equation may in fact be given by a linear combination of any two radial functions, since they are all independent. However, since it is required that the pressure is finite at the origin, $c_n$ is set to zero as $y_n(kr)$ has a singularity at the origin. Similarly, in the exterior domain, spherical Hankel functions are more appropriate solutions since large values of the arguments (far from the origin) represent travelling waves, whereas spherical Bessel functions represent standing waves. However, the choice of the appropriate Hankel function is based on the satisfaction of the Sommerfeld radiation condition at infinity.

$$\lim_{r\to\infty}\left(\frac{\partial p}{\partial r} - ikp\right) = 0 \tag{2.11}$$

The interpretation of the radiation condition is that in order to obtain a unique solution to the acoustic radiation problem, in unbounded domains, it is not sufficient that the functions decay to zero at infinity, but also they have to be outgoing. Therefore, for the time dependence given by $e^{-i\omega t}$ , coefficients $e_n$=0 in Eq 2.9b, and spherical Hankel functions of 1st kind, $h_n^{(1)}(kr)$, are chosen.

2.2.1.3 Boundary conditions

The boundary conditions on the spherical cap are given in terms of the normal velocity as:

$$\frac{\partial p}{\partial n} = i\omega\rho_f v(r,\theta) \tag{2.12}$$

where the normal $\vec{n}$ is pointing towards the fluid medium, and v(r, θ) is the velocity distribution on the spherical cap surface. Alternatively, a pressure boundary condition may be specified on the spherical cap. On the baffle plane, the inward normal velocity is considered to be zero.

$$\frac{\partial p}{\partial n} = 0\Big|_{\theta=\pi/2} \tag{2.13}$$

The inward normal on the spherical cap boundary is given by:

$$\vec{n} = \hat{e}_s = \cos(\theta+\psi)\hat{e}_r - \sin(\theta+\psi)\hat{e}_\theta \tag{2.14}$$

The normal derivative of the pressure on the spherical cap surface is therefore:

$$\frac{\partial p}{\partial n} = \vec{n}\cdot\nabla p = (\cos(\theta+\psi)\hat{e}_r - \sin(\theta+\psi)\hat{e}_\theta).(\frac{\partial p}{\partial r}\hat{e}_r + \frac{1}{r}\frac{\partial p}{\partial \theta}\hat{e}_\theta) \tag{2.15}$$

which simplifies to:

$$\frac{\partial p}{\partial n} = \cos(\theta+\psi)\frac{\partial p}{\partial r} - \sin(\theta+\psi)\frac{1}{r}\frac{\partial p}{\partial \theta} \tag{2.16}$$

Similarly, on the baffle plane

$$\frac{\partial p}{\partial n} = \vec{n}\cdot\nabla p = -\hat{e}_\theta.(\frac{\partial p}{\partial r}\hat{e}_r + \frac{1}{r}\frac{\partial p}{\partial \theta}\hat{e}_\theta) = -\frac{1}{r}\frac{\partial p}{\partial \theta} \tag{2.17}$$

For convenience, the baffle surface $\Gamma_B$ lies in the exterior domain (see Fig 2.4) and therefore by substituting Eq 2.9b in Eq 2.13, we obtain:

$$\frac{\partial p}{\partial n} = -\frac{1}{r}\frac{\partial}{\partial \theta}\left[\sum_{n=0}^{+\infty} e_n P_n(\cos\theta) h_n^{(1)}(kr)\right] = 0 \tag{2.18}$$

Performing the differentiation of the Legendre polynomials:

$$\frac{\partial p}{\partial n} = -\frac{1}{r}\left[\sum_{n=0}^{+\infty} e_n \left.\frac{\partial P_n(\cos\theta)}{\partial \theta}\right|_{\theta=\pi/2} h_n^{(1)}(kr)\right] = 0$$

The derivative of a Legendre polynomial at θ=π/2 vanish for even orders (Bell, 1968), as:

$$\frac{\partial P_{2n}(0)}{\partial \theta} = 0 \tag{2.19a}$$

Therefore,

$$\frac{\partial p}{\partial n} = -\frac{1}{r}\left[\sum_{n=0}^{+\infty} e_n \frac{\partial P_n(0)}{\partial \theta} h_n^{(1)}(kr)\right] = \frac{1}{r}\left[\sum_{n=0}^{+\infty} e_{2n+1} \frac{(-1)^n (2n+1)!}{2^{2n}(n!)^2} h_n^{(1)}(kr)\right] = 0 \tag{2.19b}$$

The only possibility for Eq. 2.19b to be equal to zero is that the odd coefficients of the expansion must vanish. The pressure in the exterior domain may thus be expressed as:

$$p^{(e)} = \sum_{n=0}^{+\infty} a_{2n} P_{2n}(\cos\theta) h_{2n}^{(1)}(kr) \tag{2.20}$$

2.2.1.4 Boundary conditions on the artificial surface

On the artificial surface, continuity conditions of normal velocity and pressure are satisfied such that:

$$\left.\frac{\partial p^{(i)}}{\partial n}\right|_{r=ka} = \left.\frac{\partial p^{(e)}}{\partial n}\right|_{r=ka} \tag{2.21a}$$

and

$$\left. p^{(i)}\right|_{r=ka} = \left. p^{(e)}\right|_{r=ka} \tag{2.21b}$$

By substitution of Eqs 2.9a and 2.20 in Eq 2.21, a relationship is obtained between the even and the odd coefficients of the inner series ($b_n$) given as:

$$b_{2n} = i(4n+1)(ka)^2 \sum_{m=0}^{\infty} \left[j_{2m+1}(ka) h_{2n}'^{(1)}(ka) - j_{2m+1}'(ka) h_{2n}'^{(1)}(ka)\right] b_{2m+1} I_{m,n} \tag{2.22}$$

Also, a relationship between the coefficients of the outer series ($a_n$) is obtained as

$$a_n = \frac{1}{h_{2n}^{(2)}(ka)}\left( b_{2n} j_{2n}(ka) + (4n+1)\sum_{m=0}^{\infty} b_{2m+1} j_{2m+1}(ka) I_{m,n} \right) \tag{2.23}$$

where

$$I_{m,n} = \int_0^{\pi/2} P_{2m}(\cos\theta) P_n(\cos\theta) \sin\theta d\theta \tag{2.24}$$

To obtain a solution to the boundary value problem, the infinite series of Eqs 2.9a and 2.20 are truncated keeping the first $N_B$ and $N_A$ coefficients, respectively. Eq 2.22 provides $N_A$ equations with $N_B$ coefficients while the boundary condition of Eq 2.12. is discretized by boundary collocation, to provide another set of $N_P$ equations also with $N_B$ coefficients.

2.2.1.5 Normalization of the matrix system

The method described above results in a system of $N_B$ equations with unknowns as the coefficients of the inner series (Coulouvrat, 1993). For accurate numerical solutions, the resultant system of equations has to be normalized. The normalization procedure has not been discussed in Coulouvrat's paper. Therefore, the matrix partitioning and the rearrangement of terms followed in this work is different from that presented in Coulouvrat's paper.

To ensure that no zero entries lie on the main diagonal, we carry out a column rearrangement such that columns corresponding to the odd coefficients, $b_O$, appear first, followed by the even coefficients, $b_E$. This column rearrangement leads to a partitioning of Eqs 2.12 and 2.22 as:

$$\left[\begin{array}{c|c} A_{N_O \times N_O} & B_{N_O \times N_E} \\ \hline C_{N_E \times N_O} & D_{N_E \times N_E} \end{array}\right] \left\{\begin{array}{c} \overline{b}_{O\, N_O \times 1} \\ \hline \overline{b}_{E\, N_E \times 1} \end{array}\right\} = \left\{\begin{array}{c} \overline{P}_{O\, N_O \times 1} \\ \hline \overline{P}_{E\, N_E \times 1} \end{array}\right\} \tag{2.25}$$

where the coefficients of the inner series have been normalized, $N_O$ is the number of odd terms of the inner series and $N_E$ is the number of the even terms of the inner series, calculated as:

$$N_O = \begin{cases} \dfrac{N_B}{2} & \text{for } N_B \text{ even} \\ \dfrac{N_B - 1}{2} & \text{for } N_B \text{ odd} \end{cases} \tag{2.26}$$

and

$$N_E = N_B - N_O$$

The normalized coefficients are related to the coefficients of Eq 2.9a by:

$$\bar{b}_n = \begin{cases} b_n & n = 1, N_O + 1 \\ b_n \prod_{p=1}^{n-1} \dfrac{j_p(ka)}{j_{p-1}(ka)} & n \neq 1, N_O + 1 \end{cases} \tag{2.27}$$

By considering normalized coefficients of the inner series, we ensure that the resultant matrix M is non-singular as we consider higher orders of the basis functions and accuracy of solution of the system of equations (Eq 2.25) is maintained. We note that alternative normalization for the system of equations arising from Coulouvrat's method has been suggested by Sapozhnikov and Sinilo (2002), similar to the one used by Schmidt (1993) for the solution of global stiffness matrices from spherically stratified shells.

Partition [A] is further subdivided into two partitions $[A^1]$, associated with the collocation points $N_P$ and $[A^2]$ associated with the terms in excess of $N_B/2$.

$$[A] = \begin{bmatrix} {A^1}_{N_P \times N_O} \\ {A^2}_{(N_A - N_E) \times N_O} \end{bmatrix} \tag{2.28}$$

where

$$\begin{aligned} {A^1}_{m,n} &= N_{m,n} \left[ \alpha_m P_{2n-1}(\cos\theta_m) \frac{j'_{2n-1}(kr_m)}{j_{2n-2}(kr_m)} + \beta_m P'_{2n-1}(\cos\theta_m) \frac{j_{2n-1}(kr_m)}{j_{2n-2}(kr_m)} \right], \quad 1 \le n \le N_O \\ {A^2}_{NP+m,n} &= \left( \frac{j_{2n-1}(ka)}{j_{2n-2}(ka)} \frac{h'^{(1)}_{2(N_E+m-1)}(ka)}{h^{(1)}_{2(N_E+m-1)}(ka)} - \frac{j'_{2n-1}(ka)}{j_{2n-2}(ka)} \right), \quad \begin{matrix} 1 \le m \le (N_A - N_E) \\ 1 \le n \le N_O \end{matrix} \end{aligned} \tag{2.29}$$

Similar to [A], partition [B] is also subdivided into two partitions [$B^1$], associated with the collocation points $N_P$ and [$B^2$]=0 associated with the number of terms in excess of $N_B/2$.

$$[B]=\begin{bmatrix} {B^1}_{N_P\times N_O} \\ \hline [0]_{(N_A-N_E)\times N_O} \end{bmatrix} \tag{2.30}$$

$${B^1}_{m,n+N_O}=\begin{cases} \left[\alpha_m P_0(\cos\theta_m)\dfrac{j_0'(kr_m)}{j_0(kr_m)}+\beta_m P_{2n-1}'(\cos\theta_m)\right], & n=1 \\ N_{m,n}\left[\alpha_m P_{2(n-1)}(\cos\theta_m)\dfrac{j_{2(n-1)}'(kr_m)}{j_{2(n-1)-1}(kr_m)}+\beta_m P_{2n-1}'(\cos\theta_m)\dfrac{j_{2n-1}(kr_m)}{j_{2n-2}(kr_m)}\right] & 2\le n\le N_E \end{cases} \tag{2.31}$$

where

$$\alpha_m=-\sqrt{(\cos\theta_m\cos\chi)^2+\sin^2\chi}$$

and

$$\beta_m=\frac{\left(1-\cos^2\theta_m\right)\cos\theta_m\cos\chi}{(ka)\left(\cos\theta_m\cos\chi+\sqrt{(\cos\theta_m\cos\chi)^2+\sin^2\chi}\right)}$$

The advantage of presenting [$A^1$] and [$B^1$] in this form is that the terms are separated into two parts, the bracketed term that is always of order 1, and the factor $N_{m,n}$ which is computed separately as:

$$N_{m,s}=\begin{cases} 1 \quad s=1,2 \\ \displaystyle\prod_{p=1}^{s-1}\frac{j_p(kr_m)}{j_{p-1}(kr_m)}\frac{j_{p-1}(ka)}{j_p(ka)} & 2<s<NB \end{cases} \tag{2.32}$$

The factor $N_{m,s}$ decreases with increasing order and will eventually underflow.

Terms in partitions [C] and [D] are given as:

$$C_{N_O+m,n}=\left(\frac{j_{2n-1}(ka)}{j_{2n-2}(ka)}\frac{h_{2(m-1)}'^{(1)}(ka)}{h_{2(m-1)}^{(1)}(ka)}-\frac{j_{2n-1}'(ka)}{j_{2n-2}(ka)}\right)I_{m,n} \quad 1\le m\le N_E \tag{2.33}$$

$$D_{m+N_O,n+N_O} = diag\left(\begin{cases} \dfrac{i}{(ka)^2 j_0(ka) h_0^{(1)}(ka)} & m,n=1 \\ \dfrac{i}{(4m-3)(ka)^2 j_{2m-3}(ka) h_{2(m-1)}^{(1)}(ka)} & m,n \geq 2 \end{cases}\right) \tag{2.34}$$

The right hand-side vector $\overline{P}$ is given as:

$$\overline{P}_m = \begin{cases} \dfrac{i\rho^f v^f v(kr_m,\theta_m)}{j_0(kr_m)} & 1 \leq m \leq NP \\ 0 & m+1 \leq m \leq NB \end{cases} \tag{2.35}$$

As seen in Eqs 2.27-2.34, we need to compute a range of orders of the radial functions $j_q(x)$, and $h_q(x)$ for a specific argument. Similar requirements are found in applications that involve acoustic and electromagnetic scattering. It is well known that Bessel functions exhibit two distinctly different behaviors depending if the order is smaller or larger than their argument. When the order is smaller than the argument (q<x), the behavior of the spherical Bessel functions $j_q(x)$ is oscillating whereas, as soon as q>x it rapidly and monotonically decreases towards zero. On the other hand, spherical Bessel functions of the second kind (Neumann functions) that form the imaginary part of the Hankel functions, rapidly diverge to infinity as the order becomes greater than the argument. For computations performed in double precision, a floating point number according to IEEE standard can be represented if it lies between ~ $10^{308}$ and $10^{-308}$. Beyond these limits the radial functions cannot be computed, and overflow or underflow occurs. This puts a limitation to the maximum order of radial functions that we may compute. For example, for x=10, the maximum order we may compute is q~244 whereas for x=1000, q~1842. Since it is not known in advance how many terms need to be included for a solution to converge, we must be able to compute orders that are between 1-5 times greater than the argument as suggested by Coulouvrat and researchers following his method (Cathignol and Saposhznikov, 1999, Sapozhnikov and Sinilo 2002). Thus, rather than computing Bessel and Hankel functions

directly, we chose to re-formulate the terms in the matrix system of Eq 2.25 by combinations of Bessel and Hankel functions which are more amenable for computation (Babenko et al 2003).

$$T_q(x) = \frac{j'_{q+1}(x)}{j_q(x)} \qquad R_q(x) = \frac{j_{q+1}(x)}{j_q(x)} \qquad H_q = \frac{h'^{(1)}{}_q(x)}{h^{(1)}{}_q(x)} \qquad G_q = j_{q-1}(x)h_q^{(1)}(x)$$

These combinations appear as a result of the normalization of the coefficients of the inner series and facilitate accurate estimation of the matrix coefficients. For example, the ratio $T_q(x)$ behaves well as the q>x which is the root cause of numerical overflow/underflow problem. $T_q(x)$ asymptotically approaches ½ as q>x. By considering the ratio $R_q$, we ensure that the underflow delayed considerably. $H_q(x)$ yields numbers whose real parts are on the order of 0.1, however the imaginary part can still decrease to very small numbers. $G_q(x)$ has a similar behavior as $H_q(x)$ where the imaginary part is well behaved number of the order 0.1 whereas the real part decreases to small numbers.

2.2.1.5.1 Ratios $T_q(x)$ and $R_q(x)$

All radial wave functions follow recurrence relationships of the type

$$f_{q-1}(x) + f_{q+1}(x) = \frac{2q+1}{x} f_q(x) \tag{2.36}$$

$$f'_q(x) = f_{q-1} - \frac{q+1}{x} f_q(x) \tag{2.37}$$

where $f_q(x)=j_q(x)$, $y_q(x)$, $h^{(1)}{}_q(x)$ or $h^{(2)}{}_q(x)$. Dividing recurrence (11) by $j_q(x)$, we obtain:

$$\frac{j_{q+1}(x)}{j_q(x)} = \frac{q}{x} - \frac{j'_q(x)}{j_q(x)}$$

or

$$R_q(x) = \frac{q}{x} - D_q(x) \tag{2.38}$$

where we set

$$D_q(x) = \frac{j'_q(x)}{j_q(x)}$$

Recurrence (11) may be divided by $j_{q-1}(x)$ and written in the form:

$$\frac{j'_{q+1}(x)}{j_q(x)} = 1 - \left(\frac{q+2}{x}\right)\frac{j_{q+1}(x)}{j_q(x)}$$

or (2.39)

$$T_q(x) = 1 - \left(\frac{q+2}{x}\right)R_q(x)$$

Computation of Bessel functions of the first kind is unstable by upward recurrence of Eq 2.36 since it is performed in the direction which the function is decreasing (Gautschi 1967), whereas computation of the Neumann functions by the same recurrence is perfectly fine. For this reason, algorithms have been devised to compute the Bessel functions of the first kind by backward recurrence where then the obvious challenge is the determination of a starting value. Miller's method (Miller 1952) or "ratio" method (Corbato and Uretski 1959) suggest that an approximate starting value of $j_q(x)$ and $j_{q+1}(x)$ or their ratio may be used to initialize the downward recurrence starting however from a much higher order than the one we actually desire to compute. An alternative method to compute the starting value has been presented by Lentz (1976) using a continued fraction representation of the Bessel function ratio $[R_q(x)]^{-1}$. A modified approach presented by Barnett (1996) has been utilized in this work, given as:

$$D_q(x) = \frac{j'_q(x)}{j_q(x)} = \frac{q}{x} - \cfrac{1}{\cfrac{2q+3}{x} - \cfrac{1}{\cfrac{2q+5}{x} - \cfrac{1}{\cfrac{2q+7}{x} - \cdots}}} \qquad (2.40)$$

where q will take the value of the maximum order we want to compute.

Methods for computing continued fractions of the type given by:

$$F(x) = b_0 + \cfrac{a_1}{b_1 + \cfrac{a_2}{b_2 + \cfrac{a_3}{b_3 + \cdots}}} \tag{2.41}$$

have been discussed by Lentz (1976), Thompson and Barnett (1986) and Press et al. (1988). Such fractions carry on to infinity but may be truncated at any desired accuracy by considering terms up to the nth convergent $F_l(x)$ as:

$$F_l(x) = b_0 + \cfrac{a_1}{b_1 + \cfrac{a_2}{b_2 + \cfrac{a_3}{b_3 + \ldots + \cfrac{a_l}{b_l}}}} \tag{2.42}$$

In this work the algorithm developed by Thompson and Barnett (1986) and found in Press et al (1988 pg 169-172), has been utilized to compute the continued fraction of $D_q(x)$ in Eq 2.40. However in order to reduce the computational effort, we have used the even part of the continued fractions such that the terms in Eq 2.42 have the following form:

$$\begin{aligned} b_0 &= \frac{q}{x}, \quad a_1 = -\frac{x}{2q+3} \\ b_1 &= 1 - \frac{x^2}{(2q+3)(2q+5)} \\ a_l &= -\frac{x^4}{(2q+2l+1)(2q+2l+3)^2(2q+2l+5)} \\ b_l &= 1 - \frac{2x^2}{(2q+2l+1)(2q+2l+5)} \end{aligned} \tag{2.43}$$

Values of orders lower than the maximum order, $q_{max}$, are then computed through a downward recurrence given by:

$$D_{q-1}(x) = \frac{q-1}{x} - \frac{1}{D_q(x) + \frac{q+1}{x}}, \qquad q = q_{\max} \ldots 1 \tag{2.44}$$

where repeated use of Eq 2.11 is performed to derive Eq 2.44. Having computed all the orders of $D_q(x)$ we use Eqs 2.38 and 2.39 to compute $R_q(x)$ and $T_q(x)$ respectively.

2.2.1.5.2 Ratio $H_q(x)$

Along the lines of previous derivation, for $R_q(x)$ and $T_q(x)$, the ratio $H_q(x)$ is computed using an upward recurrence given as:

$$H_q(x) = -\frac{q+1}{x} - \frac{1}{H_{q-1}(x) - \frac{q-1}{x}}, \quad q = 1 \ldots q_{\max} \tag{2.45}$$

where the beginning term $H_0(x) = \frac{h_0'^{(1)}}{h_0^{(1)}} = i - \frac{1}{x}$ is used to initialize the recurrence.

2.2.1.5.3 Product $G_q(x)$

$G_q(x)$ is a product of a Hankel function of the first kind and a Bessel function of the next lower order. The product may be separated into real and imaginary parts as:

$$G_q(x) = \bar{J}_q(x) + \bar{Y}_q(x)i \tag{2.46}$$

where $\bar{J}_q(x) = j_q(x) j_{q-1}(x)$, $\bar{Y}_q(x) = y_q(x) j_{q-1}(x)$

To calculate $\bar{Y}_q(x)$ we can derive the following upward recurrence relation:

$$\bar{Y}_{q+1}(x) = \frac{1}{(q+1)} \bar{Y}_q(x)\left[1 - T_{q-1}(x)\right]\left[q - xS_{q-1}(x)\right], \quad q \geq 1 \tag{2.47}$$

where $S_{q-1}(x) = \frac{y'_{q-1}(x)}{y_{q-1}(x)}$.

The recurrence in Eq 2.47 may be initialized by:

$$\bar{Y}_0(x) = j_0(x)y_1(x) = -\frac{\sin(x)}{x^2}\left[\sin(x) + \frac{\cos(x)}{x}\right] \tag{2.48}$$

We note that even though the value in Eq 2.48 becomes infinity for x=0, such a case will not occur since the argument of $G_q(x)$ in the matrix system is never the origin.

The ratio $S_q(x) = \frac{y_q'(x)}{y_q(x)}$ is computed by upward recurrence:

$$S_q(x) = \frac{y_q'(x)}{y_q(x)} = \frac{q}{x} - \frac{y_{q+1}}{y_q} = \frac{q}{x} - \left[\frac{2q+1}{x} - \frac{y_{q-1}}{y_q}\right] \tag{2.49}$$

The recurrence in Eq 2.49 is initialized by $\frac{y_0(x)}{y_1(x)} = \frac{\sin(x)}{\cos(x)} + \frac{1}{x}$.

To compute $\bar{J}_q(x)$ we use a relationship of the type:

$$\frac{j_{q_{\max}}(x)}{j_{q_{\max}-1}(x)}\frac{j_{q_{\max}-1}(x)}{j_{q_{\max}-2}(x)}\cdots\frac{j_2(x)}{j_1(x)}\frac{j_1(x)}{j_0(x)} = R_{q_{\max}-1}(x)R_{q_{\max}-2}(x)\ldots R_1(x)R_0(x) \tag{2.50}$$

Taking logarithms on both sides yields:

$$\log\left[j_{q_{\max}}(x)j_{q_{\max}-1}(x)\right] = \log\left[j_0(x)j_1(x)\right] + \log\left[R_0(x)\right] + \log\left[R_{q_{\max}-1}(x)\right] + 2\sum_{p=2}^{q_{\max}-2}\log\left[R_p(x)\right] \tag{2.51}$$

where

$$j_0(x)j_1(x) = \bar{J}_1(x) = -\frac{\sin(x)}{x^3}\left[x\cos(x) - \sin(x)\right] \tag{2.52}$$

Thus

$$\bar{J}_{q_{\max}}(x) = 10^{\log\left[\bar{J}_1\right] + \log(R_0) + \log\left(R_{q_{\max}-1}\right) + 2\sum_{p=2}^{q_{\max}-2}\log\left[R_p(x)\right]} \tag{2.53}$$

For accurate computations, the mantissa and the characteristic of the logarithms in Eq 2.53 are computed separately.

2.2.1.5.4 Normalization Factors $N_{m,n}$

The normalization factor $N_{m,n}$ is computed using a relationship of the type of Eq 2.50 as:

$$\log(N_{m,n}) = \sum_{p=1}^{n-1} \{\log[R_{n-1}(kr_m)] - \log[R_{n-1}(ka)]\} \tag{2.54}$$

Thus, taking inverse logarithms, we obtain:

$$N_{m,n} = 10^{\sum_{p=1}^{n-1} \{\log[R_{n-1}(kr_m)] - \log[R_{n-1}(ka)]\}} \qquad n > 2 \tag{2.55}$$

### 2.2.2 Angular spectrum

The angular spectrum decomposition provides the means to couple the computed ultrasonic fields with a plane wave propagation model for the substrate. We consider the pressure field at the plane $z_0$ from the origin C as a superposition of elementary functions $\exp(i(k_x x+k_y y))$ as:

$$p(x, y, z_0) = \int_{-\infty}^{\infty} dk_x \int_{-\infty}^{\infty} P(k_x, k_y) e^{i(k_z z_0)} e^{i(k_x x + k_y y)} dk_y \tag{2.56}$$

where the amplitude spectrum $P(k_x, k_y)$ may be interpreted as a complex weight distribution that must be applied to each elementary function in order to construct the pressure field (Goodman, 1996). The elementary functions are regarded as plane waves of the form:

$$e^{i(k_x x + k_y y + k_z z) - i\omega t} = e^{i\vec{k}\cdot\vec{r} - i\omega t} \tag{2.57}$$

where $k=k_x e_1+k_y e_2+k_z e_3$ is the vector that defines the direction of propagation of the wavefront with components $k_x$, $k_y$ and $k_z$ in the x, y and z direction respectively. Vector $r=xe_1+ye_2+ze_3$ is the position vector of an observation point in the pressure field as shown in Fig 2.5.

In a spherical coordinate system, the components of the wave vector are given as:

$$\begin{aligned} k_x &= k \sin\alpha \cos\beta \\ k_y &= k \sin\alpha \sin\beta \\ k_z &= k \cos\alpha \end{aligned} \tag{2.58}$$

where, $k=\omega/v_f$ and the angles $\alpha$ and $\beta$ as shown in Fig 2.5.

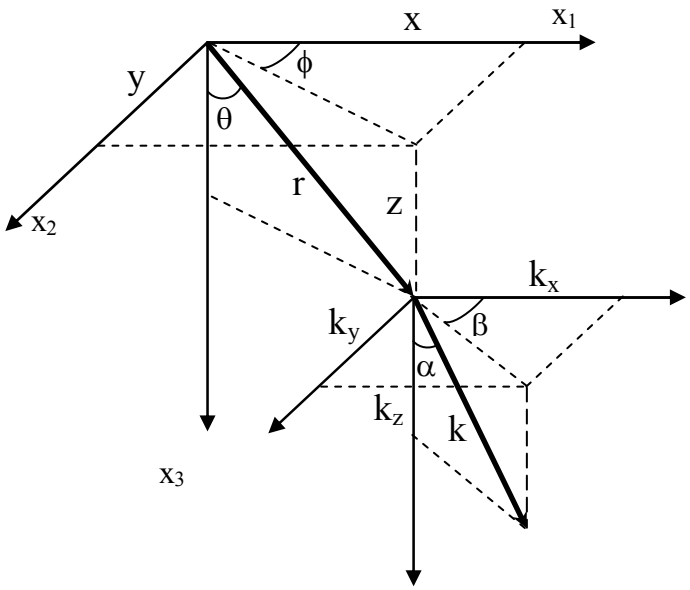


Figure 2.5 Definition of wave vector and position vector

The $k_z$ component is dependent upon $k_x$ and $k_y$ as:

$$k_z = \pm\sqrt{k^2 - k_x^2 - k_y^2} \tag{2.59a}$$

In Eq 2.59a, it is possible that the quantity underneath the square root may become negative, rendering $k_z$ complex. In that case, waves are called evanescent and Eq 2.59a then becomes:

$$k_z = \pm i\sqrt{k_x^2 + k_y^2 - k^2} \tag{2.59b}$$

The amplitude $P(k_x, k_y)$ of each plane wave in all directions of propagation is called the angular spectrum of the pressure field at a plane.

2.2.2.1 Details of computation of the angular spectrum of pressure fields at a plane

In order to evaluate the amplitude $P(k_x, k_y)$ of each plane wave, we utilize a two-dimensional Fourier transform of the form:

$$P(k_x, k_y, z_0) = \int_{-\infty}^{\infty} dx \int_{-\infty}^{\infty} p(x, y, z_0) e^{-i(k_x x + k_y y)} dy \tag{2.60}$$

Eq 2.60 can be evaluated using a two-dimensional fast Fourier transform (2-D FFT) ( Orofino and Pedersen, 1993). To this end, the pressure field at a plane $z_0$ is computed at N×N uniformly sampled locations over a square discretization region of size L×L. The sampling interval in the spatial domain is given as:

$$\Delta x = \Delta y = \frac{L}{N} \tag{2.61}$$

For convenience, the sampling interval is chosen as powers of 2. Introducing integer indices $l, m, p, q = 0,1,\cdots N-1$ the spatial domain and wave-number domains are then discretized as:

$$\begin{aligned} x(l) &= \left(l - \frac{N}{2} + 1\right)\Delta x \qquad & k_x(p) &= \frac{1}{N(\Delta x)}\left(p - \frac{N}{2} + 1\right) \\ y(m) &= \left(m - \frac{N}{2} + 1\right)\Delta y \qquad & k_y(q) &= \frac{1}{N(\Delta y)}\left(q - \frac{N}{2} + 1\right) \end{aligned} \tag{2.62}$$

The spatial domain was discretized in this fashion so that the spatial coordinates are centered at the origin of the acoustic axis. Similarly, the wavenumber domain was discretized so that the spatial scale will allow both positive and negative angles. The angular spectrum of Eq 2.60 then takes the following discrete form:

$$\tilde{P}(p,q) = (-1)^{p+q} \sum_{l=0}^{N-1} \sum_{m=0}^{N-1} \tilde{p}(m,n) e^{-i2\pi \frac{(pm+qn)}{N}} \tag{2.63}$$

where we used tilde to distinguish between the discrete and the continuous angular spectra. The two-dimensional angular spectrum evaluated numerically through MATLAB® two-dimensional FFT routine.

The spatial sampling interval, as specified by the Nyquist criterion, ultimately determines the highest spatial frequency present in the angular spectrum. Thus, if the highest spatial frequency $k_{max}$, is known in advance, then the sampling interval in the spatial domain should be:

$$\Delta x = \Delta y \leq \frac{1}{2k_{\max}} \tag{2.64}$$

However, it is known that in the case of a system with a finite source, the angular spectrum is not band-limited, but contains an infinite number of spatial frequencies, which makes the Nyquist criterion impossible to meet. In the case of aperture limited focused systems, as shown by the Debye approximation (Stamnes, 1986), the angular spectrum is mostly concentrated in the directions of propagation that fall within the aperture angle. The sampling interval calculation criterion in this case can be simply stated in terms of the aperture as L=4a along with Eq 2.61.

### 2.2.3 Focused ultrasonic field results

Using the method described above, the acoustic fields of the ultrasonic objectives used in this work were computed for the ultrasonic objectives that were used in the experimental part of this dissertation. The speed of sound in water was considered as $v^f$=1490 m/s while the ultrasonic objective geometrical parameters considered for the two transducers were: half aperture angle, $\chi$= 13.4º and aperture radius a=3mm for transducer 1 and while for transducer 2, $\chi$= 10º and aperture radius a=1.4 mm. The number of terms in the external series used were NA =610 while the internal series was truncated at NB=1200. Truncation was decided by performing convergence studies. Figs 2.6 and 2.7 give the trace of the ultrasonic pressure fields along the axis of the lens generated from the acoustic objectives used in this work at three chosen

frequencies of their frequency spectrum. We note the focus, represented by the peak amplitude has a dependence upon the frequency.

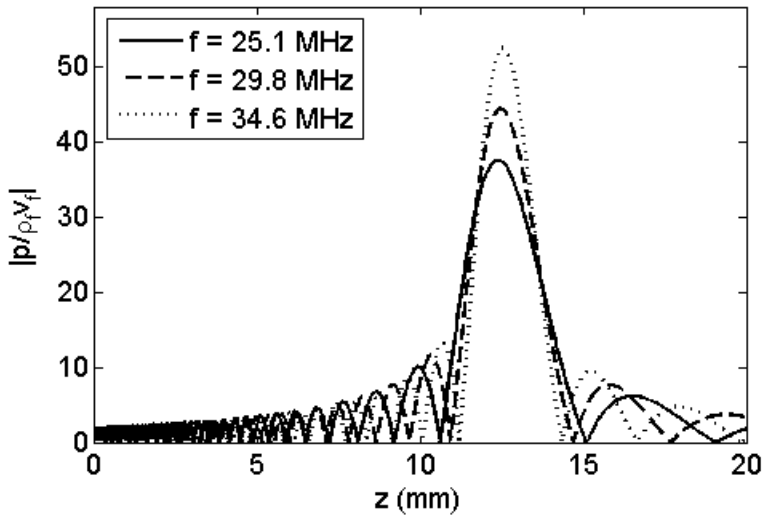


Figure 2.6 Axial fields for transducer 1

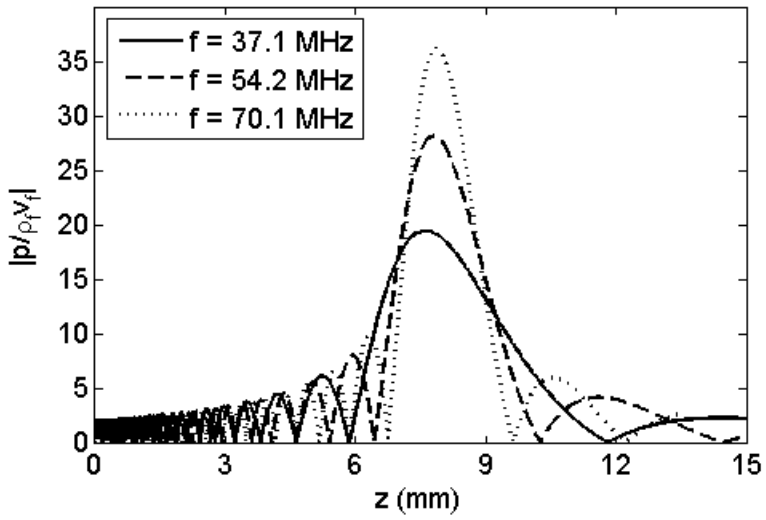


Figure 2.7 Axial fields for transducer 2

In Fig 2.8 two-dimensional contours of the focused acoustic field along the plane x-r are shown for transducer 2 at frequencies 37.1 MHz, 54.2 MHz and 70.1 MHz. We observe that the focal region of the lens becomes narrower with increasing frequency.

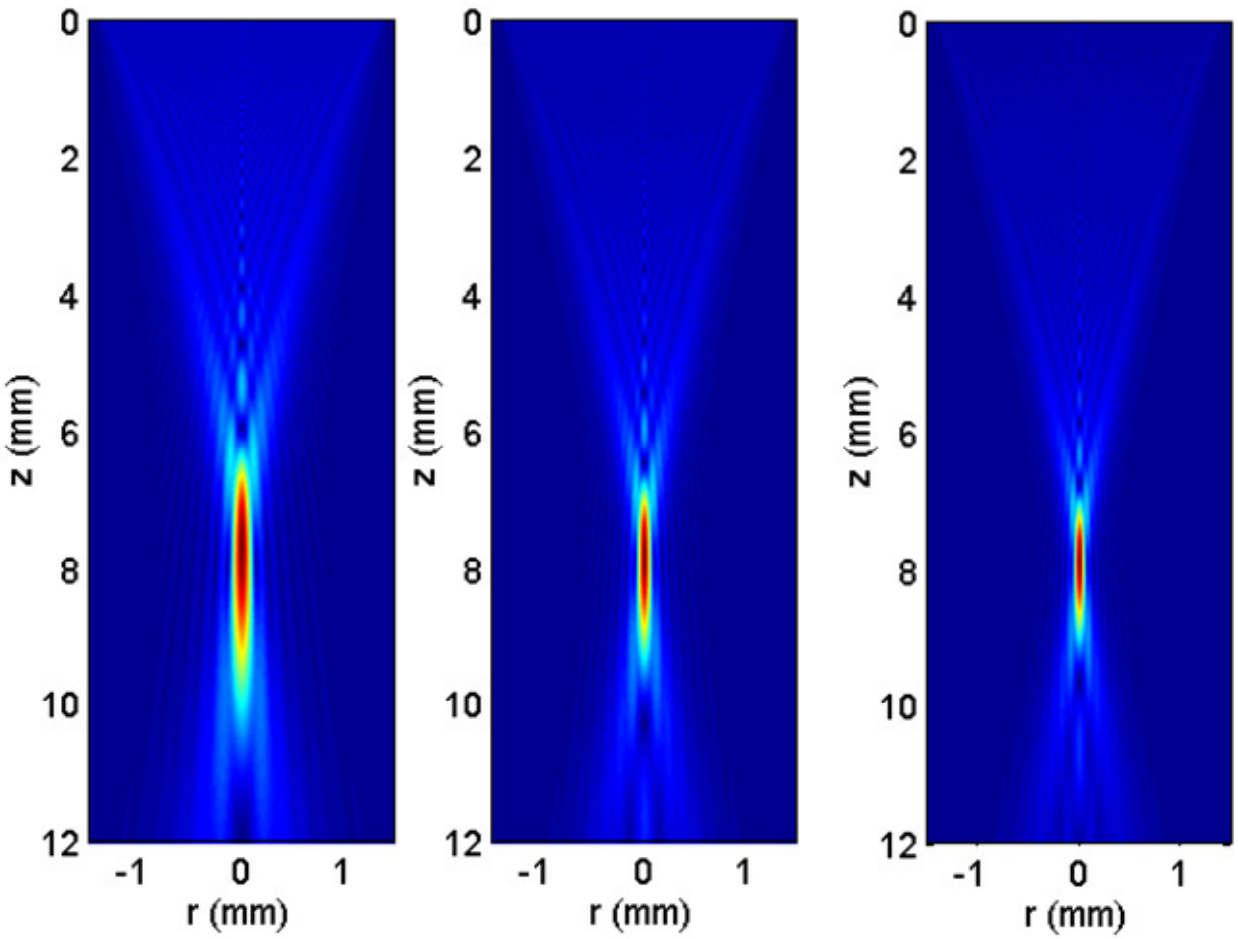


Figure 2.8 Two-dimensional contours of pressure field for transducer 2 at (a) 37.1 MHz, (b) 54.2 MHz and (c) 70.1 MHz

The fields perpendicular to the lens axis were evaluated at a plane near the focus and are presented in Fig 2.9. In pulse-echo measurements, the specimen is held at a fixed distance from the acoustic objective. Since, broadband transducers were used in this work and the focal plane

is frequency dependent, the specimen will not be in focus at all frequencies. The plane at which the pressure fields were computed, was chosen to lie between the focal planes at the two edge frequencies of the frequency spectrum. Thus, for the transducer 1 (30 MHz objective), the pressures were computed at $z_0$=12.4 mm while for the transducer 2 (110 MHz objective), $z_0$=7.7 mm. Spatial resolutions at the computation plane for the transducer 1 at -3 dB (70 % of the peak amplitude) were calculated from the pressure fields as 130 microns, 105 microns, 92 microns for temporal frequencies of 25.1 MHz, 29.8 MHz and 34.7 MHz respectively. Similarly, for the transducer 2, the -3 dB spatial resolutions are 115 microns, 80 microns and 60 microns for frequencies of 37.1 MHz, 54.2 MHz and 70.1 MHz respectively. This indicates that a polychromatic ultrasonic field is able to interrogate material volumes of different sizes and consequently the received signal contains contributions from multiple scales. Thus modeling accurately the ultrasonic field becomes important, when we study complex materials with microstructure especially when this microstructure is of the order of the spatial resolution. The angular spectra corresponding to the ultrasonic fields of Fig 2.9 are plotted in Fig 2.10. We note that since the angular spectrum is axisymmetric, we only need to plot the angular spectrum on the line $k_y$=0. The number of samples, N, for the calculations was chosen as 512 after convergence studies. It is important to note here that the ultrasonic pressure fields and the angular spectra are different representations of the same quantity but they provide us with different insights. The pressure fields give us explicitly information about the area of the specimen that interacts with the ultrasonic field. The angular spectrum on the other hand provides information about the directionality of the field. Thus it becomes more useful for analysis as plane wave directions of propagation may be used as angles of incidence, which is the usual way we think of reflection and transmission. For transducer 1, 90 % of the amplitude

spectra lie within 18º, while for transducer 2 approximately 90% of the angular spectra lie within 14º. However, the variation of the amplitude within these angles is quite complicated and has an oscillating behavior. This non-monotonic behavior shows that aspects of the received amplitude are ignored if a smooth function is used to model the angular spectrum, such as Gaussian distribution. Thus, another advantage of the model presented in section 2.2.1 is that it may be used to assess the errors that are made when simpler functions are used to approximate angular spectra.

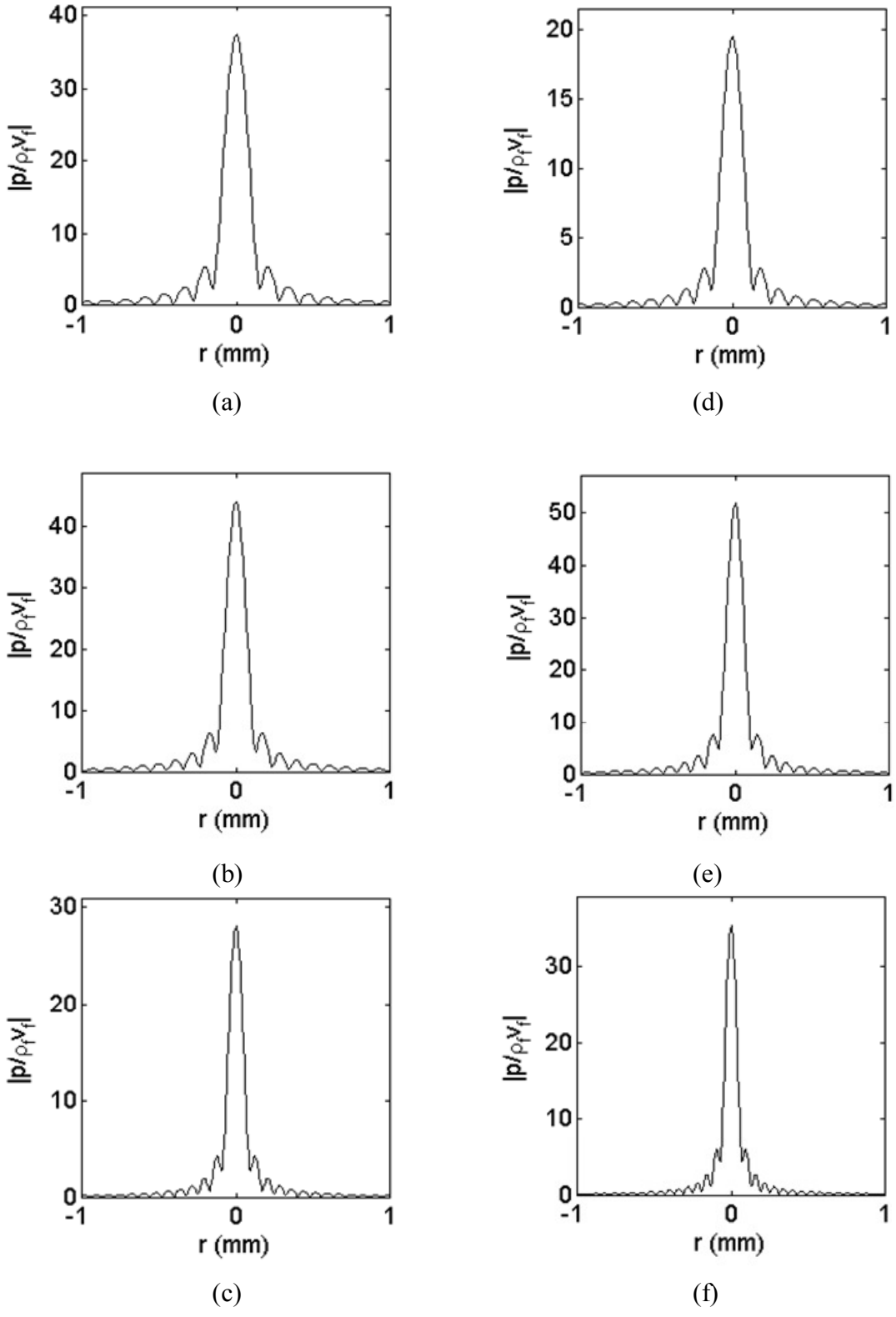


Figure 2.9 Amplitude of radial pressure fields at (a) 25.1 MHz, (b) 29.8 MHz, (c) 34.7 MHz for transducer 1 and (d) 37.1 MHz, (e) 54.2 MHz and (f) 70.1 for transducer 2.

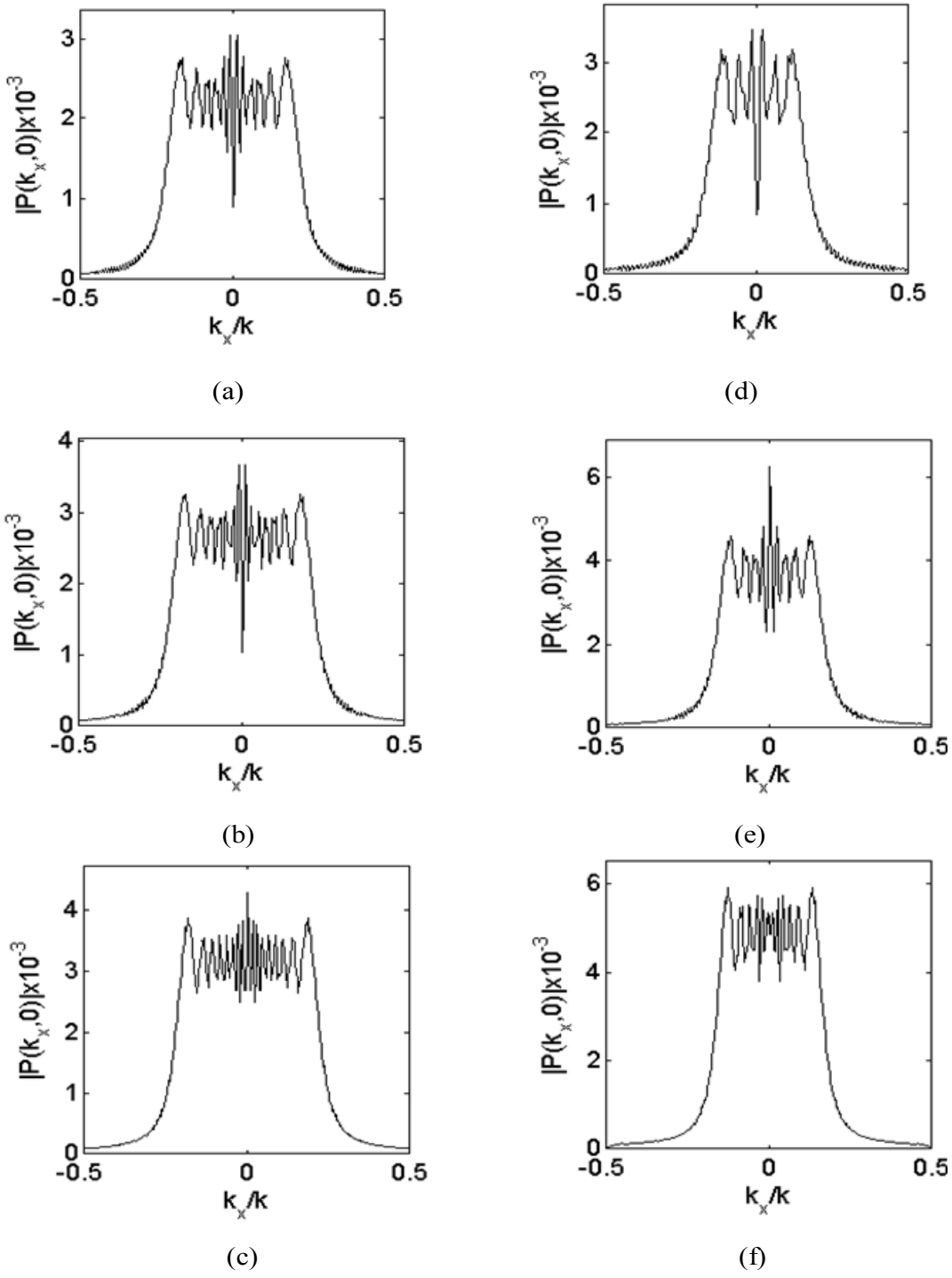


Figure 2.10 Amplitude of angular spectra at (a) 25.1 MHz, (b) 29.8 MHz, (c) 34.7 MHz for transducer 1 and (d ) 37.1 MHz, (e) 54.2 MHz and (f) 70.1 for transducer 2.

### 2.2.4 Substrate Model

It is common in acoustic microscopic studies that the substrate is idealized as a homogeneous half-space. This implies that the transition in elastic properties between the coupling fluid and the substrate is abrupt. In this case, and especially when the two materials are elastic and isotropic, the reflection coefficient amplitude achieves the well-known form of the Rayleigh-Fresnel reflection coefficients (Achenbach 1971). Such reflection coefficients, though dependent on the angle of the incident plane wave, are independent of its frequency. However, there are many instances when the substrate's elastic properties are not constant but vary with depth from the surface. In these cases, the profile as well as the extent of the depth variation is highly dependent on the process by which the property profile developed. In ion-etching processes for example (Zinin et al 1999), one finds a layer of finite thickness over which the material properties vary before gradually transitioning to the native homogeneous material. In other cases, such as for functionally graded materials (FGM), gradual variations in microstructure and composition are engineered to alleviate mechanical stress concentrations usually by graded distributions of particles embedded in a matrix. Such material systems are found in many engineering applications, including naturally occurring geomaterials, armor for military applications, and tissue engineered biomaterials.

A distinctive feature of the reflectance behavior of substrates that have graded layers is the frequency dependence of the reflection coefficients. This is especially true when the thickness of the graded layer is of the same order as the wavelengths of the incident field (Robins 1990). Using micro-Raman spectroscopy, it has been found that dentin etching results in a layer of graded composition whose thickness ranges from 20-100 μm (Wieliczka et al 1997). These observations lead us to idealize the etched dentin substrate as an inhomogeneous material where

the inhomogeneity is only along the direction normal to the surface, while the initial dentin surface is considered as homogeneous before etching. While the source of the inhomogeneity can be traced to the depletion of apatitic mineral from the dentin matrix by the acid diffusion and reaction, the profile of the mineral distribution remains largely undefined. It is reasonable though to assume that the mineral distribution is continuous or at least perceived as continuous up to a certain scale much smaller than the wavelength of the interrogating ultrasonic waves.

The reflection behavior of graded materials is far more complex compared to their homogeneous counterpart. Firstly, the idealization of the microstructure for modeling wave propagation phenomena in complex substrates is not straightforward, especially when such models are used to predict their overall dynamic behavior (Berezovski et al 2003). Secondly, finite computational resources prohibit from including all the elements of the microstructure in a single model and simplifying assumptions and averaging procedures are always required. In addition, the solutions for plane wave propagation in continuously graded substrates in closed form are not easily obtained, especially for substrates with gradients in shear moduli (Robins 1998). The main difficulty in obtaining a general closed form solution, is the fact that the solution of the elastic wave equation for inhomogeneous media (Karal and Keller 1959) cannot be expressed as displacement potentials that define purely irrotational and solenoidal fields (Hook 1961a and b) as is the case for the displacement fields in homogeneous media. However, this limitation can be circumvented by considering elastic wave propagation in discretely layered substrates of homogeneous material property in each layer. The basis for such an approximation has its foundations on a theorem by Volterra (Gilbert and Backus 1966, Aki and Richards 1980) which proves that it is possible to model wave propagation in substrates with continuous

variations in materials properties (density and elastic moduli) by considering the elastic wave solution in discretely layered systems in the limit when the number of layers becomes infinite.

Several approaches have been presented over the past few decades for plane wave propagation in discretely layered solids. This review is not aimed to be comprehensive, but it offers a background on plane wave methods in multilayered media. Thomson (1950) and Haskell (1953), who corrected a minor error in Thomson's development, used a transfer matrix method to study the transmission of elastic waves and dispersion of surface waves in stratified solid homogeneous media. The transfer matrix, relates the traction and displacement vectors at the top of the layer surface with respect to those at the bottom layer surface. The transfer matrix of the whole layer was then obtained by multiplication of each layer matrix. It was shown by Gilbert and Backus (1966) that the transfer matrix is a special case of the propagator matrix. In this case the stress and displacement vectors, and the constitutive equations with inhomogeneity dependent only on a single direction, were formulated as a system of first order differential equations. Numerical integration of the system of differential equations results in the same interpretation as the layer transfer matrix products. In spite of its simplicity, the transfer matrix method was found to be unstable for high frequencies/layer thickness products. The delta matrix approach, proposed first by Dunkin (1965) was able to overcome the numerical instabilities of the transfer matrix method, however, at the expense of higher computational effort. A different approach was developed by Knopoff (1964) known as the 'global matrix' method, where a single matrix, represents the layered system. The matrix system is formed by satisfying continuity conditions at each layer interface. This method, which does not suffer from the transfer matrix instabilities, was modified by Kausel and Roesset (1981) to utilize the layer stiffness matrix. The layer stiffness matrix, in contrast to the transfer matrix, relates the traction vector at the top

and bottom surfaces of a layer to the respective displacement vector. The layer matrices are then assembled in a similar fashion as stiffness matrices in structural analysis. Recently, Rokhlin and Wang (2001, 2002) have presented a recursive algorithm for assembling the global stiffness matrix from the layer stiffness matrix. For this work we adopt the method by Rokhlin and Wang since it is computationally efficient and stable for very thin layers.

#### 2.2.4.1 Substrate idealization

In order to model the reflection process from substrates with near-surface graded layer, such as etched dentin, a three-material model is adopted as shown in Fig 2.11.

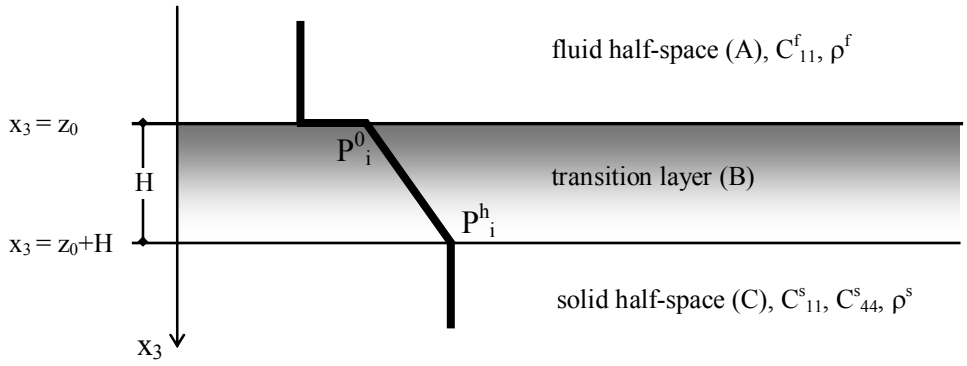


Figure 2.11 Three-material system idealization

The upper half-space, A, is considered as a homogeneous non-viscous fluid corresponding to the coupling fluid in the acoustic microscope water bath. The second material, B, is a transition layer of depth H used to represent the etched layer. This material is inhomogeneous only along the direction of $x_3$ and has isotropic elastic properties. The property variation for this material is taken to be linear with $x_3$ given by the following relationship:

$$P_i(x_3) = -\frac{\left(P_i^0 - P_i^h\right)}{H}(z_0 - x_3) + P_i^0, \qquad z_0 \le x_3 \le z_o + H \qquad \text{and} \qquad \text{i=1…3} \tag{2.65}$$

where $P_i^0$ is the $i^{th}$ material property at the top of material B, $P_i^h$ is the $i^{th}$ material property at the bottom of material B, $P_1$ = material density ($\rho$), $P_2$ = constrained modulus $C_{11}$, $P_3$ = shear modulus $C_{44}$, The variation of elastic isotropic moduli, $C_{11}$ and $C_{44}$, is such that the positive definiteness of strain energy at any material point along the $x_3$ axis is satisfied. The third material, C, is considered as a homogeneous solid half-space which represents the native dentin substrate.

We consider the second material (B) to be subdivided into N layers as shown in Fig 2.12.

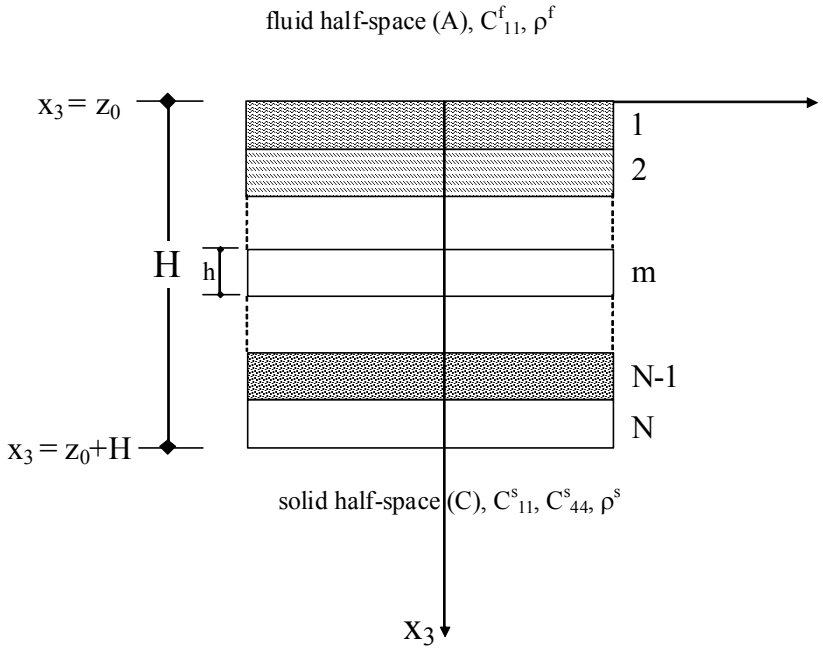


Figure 2.12 Discretization of near-surface graded layer

The displacement $\mathbf{u}^m$ for the $m^{th}$ layer is composed of six partial waves and may be written as (Rokhlin and Wang 2002):

$$\mathbf{u}^m = \sum_{j=1}^{3}\left(A_j^+ \mathbf{d}^{j^+} e^{i\omega m_3^{+j}(x_3 - z_m)} + A_j^- \mathbf{d}^{j^-} e^{i\omega m_3^{-j}(x_3 - z_{m-1})}\right)_m e^{i\omega(m_1 x_1 + m_2 x_2)} e^{-i\omega t} \tag{2.66}$$

and corresponding traction vectors $\boldsymbol{\sigma}^m$ can be obtained from Eq 2.66 and Hooke's law as:

$$\boldsymbol{\sigma}^m = \sum_{j=1}^{3}\left(iA_j^+\mathbf{g}^{j^+}e^{i\omega m_3^{+j}(x_3-z_m)} + A_j^-\mathbf{g}^{j^-}e^{i\omega m_3^{-j}(x_3-z_{m-1})}\right)_m e^{i\omega(m_1x_1+m_2x_2)}e^{-i\omega t} \tag{2.67}$$

The positive and negative subscripts correspond to waves propagating in the positive or negative $x_3$ directions, $\mathbf{d}_j$ are the unit polarization vectors that determine the direction of particle motion, vectors $\mathbf{m}_j$ are the slowness vectors which determine the direction of propagation and $A_j$ are complex displacement amplitudes for each partial wave. For simplicity, the field is considered for a single frequency and a single direction of propagation. For isotropic materials, the slowness vector components $m_3^j$ have simple closed form solutions given as:

$$m_3^{j\pm} = \begin{Bmatrix} \pm\sqrt{\dfrac{\rho}{C_{11}} - (m_1)^2} \\ \pm\sqrt{\dfrac{\rho}{C_{44}} - (m_1)^2} \\ \pm\sqrt{\dfrac{\rho}{C_{44}} - (m_1)^2} \end{Bmatrix} \tag{2.68}$$

In Eq 2.68, superscript j=1 corresponds to a longitudinal (or compressional) wave for which the particle motion is along the direction of propagation, j=2 corresponds to an SV shear wave, where the direction of particle motion is normal to the direction of propagation, and j=3 corresponds to a SH wave where the direction of particle motion is also normal to the direction of propagation but it is confined within a plane orthogonal to the SV motion.

Vectors, $\mathbf{g}_j$ are related to the polarization vectors and the elastic properties of the layer as:

$$\mathbf{g}^{1\pm} = \begin{Bmatrix} iC_{44}\omega\left(m_3^{1\pm}d_1^{1-} + m_1d_3^{1\pm}\right) \\ iC_{44}\omega\left(m_3^{1\pm}d_2^{1\pm} + m_2d_3^{1\pm}\right) \\ i\omega\left[C_{11}\left(d_3^{1\pm}m_3^{1\pm} + d_1^{1\pm}m_1 + d_2^{1\pm}m_2\right) - 2C_{44}\left(d_1^{1\pm}m_1 + d_2^{1\pm}m_2\right)\right] \end{Bmatrix} \tag{2.69a}$$

$$\mathbf{g}^{2\pm} = \begin{Bmatrix} iC_{44}\omega\left(m_3^{2\pm}d_1^{2\pm} + m_1d_3^{2\pm}\right) \\ iC_{44}\omega\left(m_3^{2\pm}d_2^{2\pm} + m_2d_3^{2\pm}\right) \\ i\omega\left[C_{11}\left(d_3^{2\pm}m_3^{2\pm} + d_1^{2\pm}m_1 + d_2^{2\pm}m_2\right) - 2C_{44}\left(d_1^{2\pm}m_1 + d_2^{2\pm}m_2\right)\right] \end{Bmatrix} \tag{2.69b}$$

$$\mathbf{g}^{3\pm}=\begin{Bmatrix} iC_{44}\omega\left(m_3^{3\pm}d_1^{3\pm}+m_1 d_3^{3\pm}\right) \\ iC_{44}\omega\left(m_3^{3\pm}d_2^{3\pm}+m_2 d_3^{3\pm}\right) \\ i\omega\left[C_{11}\left(d_3^{3\pm}m_3^{3\pm}+d_1^{3\pm}m_1+d_2^{3\pm}m_2\right)-2C_{44}\left(d_1^{3\pm}m_1+d_2^{3\pm}m_2\right)\right] \end{Bmatrix} \tag{2.69c}$$

The m[th] layer has two interfaces m-1 and m with which it communicates with the layer above and below respectively. Next the displacement (Eq 2.66) and stress vectors and (Eq 2.67) at the top and bottom interfaces are written in a matrix form as:

$$\begin{Bmatrix} u_{1,m-1} \\ u_{2,m-1} \\ u_{3,m-1} \\ \hdashline u_{1,m} \\ u_{2,m} \\ u_{3,m} \end{Bmatrix} = \left[\begin{array}{ccc:ccc} d_1^{1-} & d_1^{2-} & d_1^{3-} & d_1^{1+}e^{i\omega m_3^{1+}h_m} & d_1^{2+}e^{i\omega m_3^{2+}h_m} & d_1^{3+}e^{i\omega m_3^{3+}h_m} \\ d_2^{1-} & d_2^{2-} & d_2^{3-} & d_2^{1+}e^{i\omega m_3^{1+}h_m} & d_2^{2+}e^{i\omega m_3^{2+}h_m} & d_2^{3+}e^{i\omega m_3^{3+}h_m} \\ d_3^{1-} & d_3^{2-} & d_3^{3-} & d_3^{1+}e^{i\omega m_3^{1+}h_m} & d_3^{2+}e^{i\omega m_3^{2+}h_m} & d_3^{3+}e^{i\omega m_3^{3+}h_m} \\ \hdashline d_1^{1-}e^{-i\omega m_3^{1-}h_m} & d_1^{2-}e^{-i\omega m_3^{2-}h_m} & d_1^{3-}e^{-i\omega m_3^{3-}h_m} & d_1^{1+} & d_1^{2+} & d_1^{3+} \\ d_2^{1-}e^{-i\omega m_3^{1-}h_m} & d_2^{2-}e^{-i\omega m_3^{2-}h_m} & d_2^{3-}e^{-i\omega m_3^{3-}h_m} & d_2^{1+} & d_2^{2+} & d_2^{3+} \\ d_3^{1-}e^{-i\omega m_3^{1-}h_m} & d_3^{2-}e^{-i\omega m_3^{2-}h_m} & d_1^{3-}e^{-i\omega m_3^{3-}h_m} & d_3^{1+} & d_3^{2+} & d_3^{3+} \end{array}\right] \begin{Bmatrix} A_m^{1-} \\ A_m^{2-} \\ A_m^{3-} \\ \hdashline A_m^{1+} \\ A_m^{2+} \\ A_m^{3+} \end{Bmatrix} \tag{2.70}$$

or

$$\begin{Bmatrix} u_{m-1} \\ u_m \end{Bmatrix} = \begin{bmatrix} D^- & D^+H^+ \\ D^-H^- & D^+ \end{bmatrix} \begin{Bmatrix} A_m^- \\ A_m^+ \end{Bmatrix} = E_m^u A_m$$

$$\begin{Bmatrix} \sigma_{13,m-1} \\ \sigma_{12,m-1} \\ \sigma_{33,m-1} \\ \hdashline \sigma_{13,m-1} \\ \sigma_{12,m-1} \\ \sigma_{33,m-1} \end{Bmatrix} = \left[\begin{array}{ccc:ccc} g_1^{1-} & g_1^{2-} & g_1^{3-} & g_1^{1+}e^{i\omega m_3^{1+}h_m} & g_1^{2+}e^{i\omega m_3^{2+}h_m} & g_1^{3+}e^{i\omega m_3^{3+}h_m} \\ g_2^{1-} & g_2^{2-} & g_2^{3-} & g_2^{1+}e^{i\omega m_3^{1+}h_m} & g_2^{2+}e^{i\omega m_3^{2+}h_m} & g_2^{3+}e^{i\omega m_3^{3+}h_m} \\ g_3^{1-} & g_3^{2-} & g_3^{3-} & g_3^{1+}e^{i\omega m_3^{1+}h_m} & g_3^{2+}e^{i\omega m_3^{2+}h_m} & g_3^{3+}e^{i\omega m_3^{3+}h_m} \\ \hdashline g_1^{1-}e^{-i\omega m_3^{1-}h_m} & g_1^{2-}e^{-i\omega m_3^{2-}h_m} & g_1^{3-}e^{-\omega m_3^{3-}h_m} & g_1^{1+} & g_1^{2+} & g_1^{3+} \\ g_2^{1-}e^{-i\omega m_3^{1-}h_m} & g_2^{2-}e^{-i\omega m_3^{2-}h_m} & g_2^{3-}e^{-i\omega m_3^{3-}h_m} & g_2^{1+} & g_2^{2+} & g_2^{3+} \\ g_3^{1-}e^{-i\omega m_3^{1-}h_m} & g_3^{2-}e^{-i\omega m_3^{2-}h_m} & g_1^{3-}e^{-i\omega m_3^{3-}h_m} & g_3^{1+} & g_3^{2+} & g_3^{3+} \end{array}\right] \begin{Bmatrix} A_m^{1-} \\ A_m^{2-} \\ A_m^{3-} \\ \hdashline A_m^{1+} \\ A_m^{2+} \\ A_m^{3+} \end{Bmatrix} \tag{2.71}$$

$$\begin{Bmatrix} \sigma_{m-1} \\ \sigma_m \end{Bmatrix} = \begin{bmatrix} G^- & G^+H^+ \\ G^-H^- & G^+ \end{bmatrix} \begin{Bmatrix} A_m^- \\ A_m^+ \end{Bmatrix} = E_m^\sigma A_m$$

Substituting Eq 2.70 into 2.71 the stiffness matrix for a layer is obtained as:

$$\begin{Bmatrix} \sigma_{m-1} \\ \sigma_m \end{Bmatrix}_m = E_m^\sigma \left(E_m^u\right)^{-1} \begin{Bmatrix} u_{m-1} \\ u_m \end{Bmatrix}_m \tag{2.72}$$

$$K_m = E_m^\sigma \left(E_m^u\right)^{-1}$$

The stiffness matrices for each layer are subsequently assembled through a recursive algorithm as:

$$\begin{Bmatrix} \boldsymbol{\sigma}_1 \\ \boldsymbol{\sigma}_M \end{Bmatrix} = \left[\mathbf{K}^M\right] \begin{Bmatrix} \mathbf{u}_1 \\ \mathbf{u}_M \end{Bmatrix} = \left[\begin{array}{c|c} \mathbf{K}_{11}^M & \mathbf{K}_{12}^M \\ \hline \mathbf{K}_{21}^M & \mathbf{K}_{22}^M \end{array}\right] \begin{Bmatrix} \mathbf{u}_1 \\ \mathbf{u}_M \end{Bmatrix} \tag{2.73}$$

where

$$\begin{aligned} \mathbf{K}_{11}^M &= \mathbf{K}_{11}^{M-1} + \mathbf{K}_{12}^{M-1}\left(\mathbf{K}_{11}^m - \mathbf{K}_{22}^{M-1}\right)^{-1}\mathbf{K}_{21}^{M-1} \\ \mathbf{K}_{12}^M &= -\mathbf{K}_{12}^{M-1}\left(\mathbf{K}_{11}^m - \mathbf{K}_{22}^{M-1}\right)^{-1}\mathbf{K}_{12}^m \\ \mathbf{K}_{21}^M &= \mathbf{K}_{21}^m\left(\mathbf{K}_{11}^m - \mathbf{K}_{22}^{M-1}\right)^{-1}\mathbf{K}_{21}^{M-1} \\ \mathbf{K}_{22}^M &= \mathbf{K}_{22}^m - \mathbf{K}_{21}^m\left(\mathbf{K}_{11}^m - \mathbf{K}_{22}^{M-1}\right)^{-1}\mathbf{K}_{12}^m \end{aligned} \tag{2.74}$$

and $\mathbf{K}^{\mathbf{M}}$ is the total stiffness matrix of the top m layers, $K^{M-1}{}_{ij}$ is the total stiffness matrix of the top m-1 layers, and $K^{m}{}_{ij}$ is the stiffness matrix of the $m^{th}$ layer as given by Eq 2.72, with i, j=1..3. Through the recurrence algorithm of Eqs 2.73 and 2.74, a global stiffness matrix is formed that relates the stress and displacement vectors at the top interface of the first layer with the stresses and displacements at the bottom interface of the last layer. A global compliance matrix may also be defined as the inverse of the stiffness matrix, $S^N = \left[\mathbf{K}^N\right]^{-1}$ as:

$$\begin{Bmatrix} \mathbf{u}_1 \\ \mathbf{u}_N \end{Bmatrix} = \left[S^N\right] \begin{Bmatrix} \boldsymbol{\sigma}_1 \\ \boldsymbol{\sigma}_N \end{Bmatrix} \tag{2.75}$$

where $\boldsymbol{\sigma}_1 = \begin{Bmatrix} \sigma_{12}(x_3 = z_0) \\ \sigma_{13}(x_3 = z_0) \\ \sigma_{33}(x_3 = z_0) \end{Bmatrix}, \quad \mathbf{u}_1 = \begin{Bmatrix} u_1(x_3 = z_0) \\ u_2(x_3 = z_0) \\ u_3(x_3 = z_0) \end{Bmatrix}$

and $\boldsymbol{\sigma}_N = \begin{Bmatrix} \sigma_{12}(x_3 = z_0 + H) \\ \sigma_{13}(x_3 = z_0 + H) \\ \sigma_{33}(x_3 = z_0 + H) \end{Bmatrix}, \quad \mathbf{u}_N = \begin{Bmatrix} u_1(x_3 = z_0 + H) \\ u_2(x_3 = z_0 + H) \\ u_3(x_3 = z_0 + H) \end{Bmatrix}$ (2.76)

In order to obtain the effective reflection coefficient of the layered structure, we impose boundary conditions at interface 1 between the fluid half-space A and the $1^{st}$ layer of material B, and at the $N^{th}$ interface between the last layer of B and the underlying half-space C. For interface 1 the boundary conditions are:

$$u_3{}^A(x_3 = z_0) = u_3{}^B(x_3 = z_0) \tag{2.77a}$$

$$\sigma_{12}{}^A(x_3 = z_0) = \sigma_{12}{}^B(x_3 = z_0) = 0 \tag{2.77b}$$

$$\sigma_{13}{}^A(x_3 = z_0) = \sigma_{13}{}^B(x_3 = z_0) = 0 \tag{2.77c}$$

For interface N,

$$\begin{aligned} u_1{}^B(x_3 = z_0 + H) &= u_1{}^C(x_3 = z_0 + H) \\ u_2{}^B(x_3 = z_0 + H) &= u_2{}^C(x_3 = z_0 + H) \\ u_3{}^B(x_3 = z_0 + H) &= u_3{}^C(x_3 = z_0 + H) \end{aligned} \tag{2.78a}$$

$$\begin{aligned} \sigma_{12}{}^B(x_3 = z_0 + H) &= \sigma_{12}{}^C(x_3 = z_0 + H) \\ \sigma_{13}{}^B(x_3 = z_0 + H) &= \sigma_{13}{}^C(x_3 = z_0 + H) \\ \sigma_{33}{}^B(x_3 = z_0 + H) &= \sigma_{33}{}^C(x_3 = z_0 + H) \end{aligned} \tag{2.78b}$$

Substituting Eqs 2.77b, c in Eq 2.73 we obtain:

$$\begin{Bmatrix} u_3^B(x_3 = z_0) \\ u_1^B(x_3 = z_0 + H) \\ u_2^B(x_3 = z_0 + H) \\ u_3^B(x_3 = z_0 + H) \end{Bmatrix} = \begin{bmatrix} S_{33}^N & S_{34}^N & S_{35}^N & S_{36}^N \\ S_{43}^N & S_{44}^N & S_{45}^N & S_{46}^N \\ S_{53}^N & S_{54}^N & S_{55}^N & S_{56}^N \\ S_{63}^N & S_{64}^N & S_{65}^N & S_{66}^N \end{bmatrix} \begin{Bmatrix} \sigma_{33}^B(x_3 = z_0) \\ \sigma_{12}^B(x_3 = z_0 + H) \\ \sigma_{13}^B(x_3 = z_0 + H) \\ \sigma_{33}^B(x_3 = z_0 + H) \end{Bmatrix} \tag{2.79}$$

Next, the displacement fields in the fluid as $u^A$ and the bottom half-space, $u^C$, are introduced as:

$$\mathbf{u}^A(x_3 = z_0) = A^0 \begin{Bmatrix} d_1^0 \\ d_2^0 \\ d_3^0 \end{Bmatrix} e^{i\omega\left(m_3^0 z_0\right)} e^{i\omega(m_1 x_1)} e^{-i\omega t} + R \begin{Bmatrix} d_1^R \\ d_2^R \\ d_3^R \end{Bmatrix} e^{i\omega(m_1 x_1)} e^{-i\omega t} \tag{2.80}$$

and

$$\mathbf{u}^C(x_3 = z_0 + H) = \left[ T_P \begin{Bmatrix} d_1^{T_P} \\ d_2^{T_P} \\ d_3^{T_P} \end{Bmatrix} + T_{SV} \begin{Bmatrix} d_1^{T_{SV}} \\ d_2^{T_{SV}} \\ d_3^{T_{SV}} \end{Bmatrix} + T_{SH} \begin{Bmatrix} d_1^{T_{SH}} \\ d_2^{T_{SH}} \\ d_3^{T_{SH}} \end{Bmatrix} \right] e^{i\omega(m_1 x_1)} e^{-i\omega t} \tag{2.81}$$

In Eq 2.80, $A^0$ is the amplitude of the incident field and $R(k_x, k_y)$ is the reflectance function defined in Eq 2.1, where the wave vector components $k_x$, and $k_y$ are defined in Eq 2.58, while in

Eq 2.81, $T_p$, $T_{SV}$, and $T_{SH}$, are the corresponding transmittance functions. Utilizing Eqs 2.80 and 2.81 and elastic properties, the pressure $p^A$ field in the fluid and the stress vector in the bottom solid half-space $\sigma^C$ can be obtained. Thus, using Eqs 2.79-2.81, we can solve for the reflectance function.

2.2.4.2 Layer discretization and Convergence

Since we are using a model for wave propagation in a discretely layered medium to approximate a continuously layered medium, an iterative discretization criterion is utilized to achieve solution convergence. Thus, the computation for each incidence angle and frequency begins with a single layer and subsequently, the layer is subdivided into equal thickness increments, where the material properties are assigned to the $m^{th}$ layer using the following equation:

$$P_i(m) = -\frac{\left(P_i^0 - P_i^h\right)(2m-1)}{2N} + P_i^0, \qquad 1 \le m \le N \tag{2.82}$$

N is the total number of layers and property P follows the notation of the Eq. 2.65. The number of layers in the subdivision is incremented by a predefined quantity until the difference in the amplitude of the reflection coefficient at the $i^{th}$ and $i^{th}$-1 step was less than a specified tolerance, ε, as:

$$\left|R\right|^i - \left|R\right|^{i-1} < \varepsilon \tag{2.83}$$

In the computations performed in this work, the tolerance was set to $e=10^{-5}$. This procedure always provided a converged solution, however, the number of layers required to converge depends both on the angle of incidence and the temporal frequency considered, as well as the steepness of the profile.

### 2.2.5 Parametric Studies

We performed parametric studies in order to understand the effects of gradation in material properties to the frequency dependence of the reflection coefficients. In our parametric study, we have considered that material B transitions with no discontinuity to the underlying half-space C so that $P_1^h=\rho^h=\rho^s$, $P_2^h=C_{11}^h=C_{11}^s$ and $P_3^h=C_{44}^h=C_{44}^s$. However, the material properties at the top material B, were allowed to differ from the overlying fluid half-space such that $\rho^f \leq \rho^0 \leq \rho^s$, $C_{11}^f \leq C_{11}^0 \leq C_{11}^s$ and $0 \leq C_{44}^0 \leq C_{44}^s$. Furthermore, we have considered a specific set of material properties appropriate for dentin so as to keep the results relevant to the substrate used in our experimental studies. For the water half-space, the bulk modulus, $C_{11}^f$ was considered as 2.22 GPa, and density $\rho^f = 1.0$ Mg/m$^3$. The material density of the dentin substrate was taken as $\rho^s$=2.1 Mg/m$^3$, while the elastic moduli are taken as, $C_{11}^s$=38.6 GPa, and $C_{44}^s$=8.03 GPa. Dentin elastic properties were adapted from a Kinney et al (2004). The density of the dentin substrate was computed using literature values for the collagen and mineral

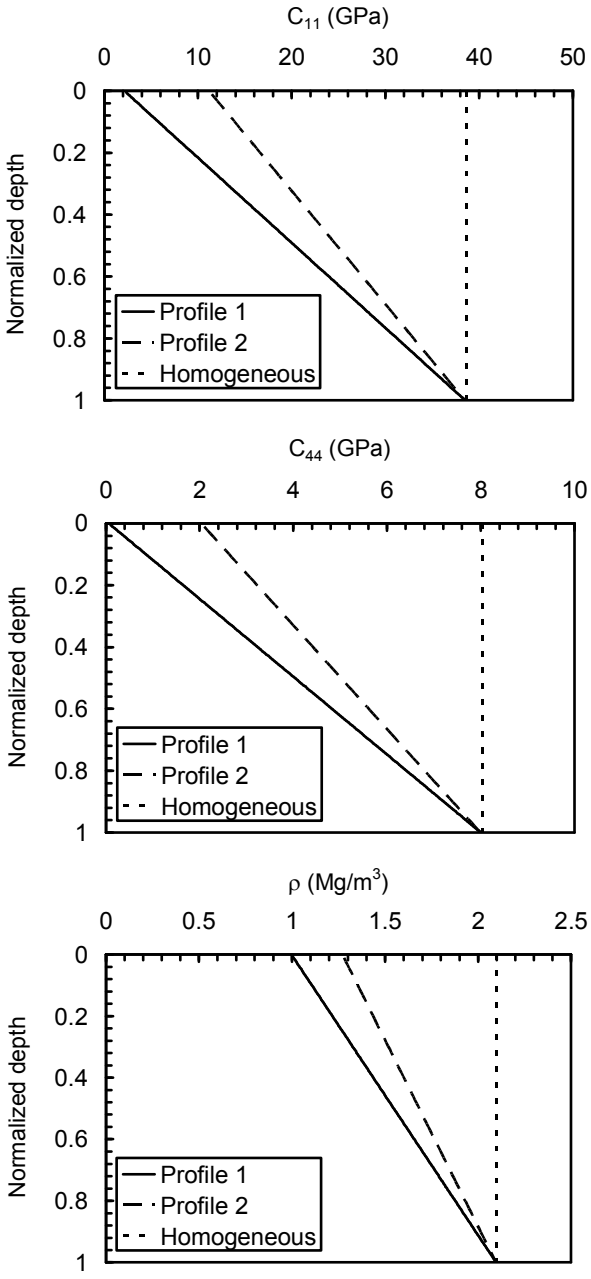


Figure 2.13 Material property profiles used in the parametric study

components and porosity for mid-coronal dentin (Marangos et al 2009). Example profiles for the graded layer (material B) are shown in Fig 2.13.

In the following discussion, we use the wavenumber-thickness product, $k^f H = \omega H / v^f$. The dimensionless number $k^f H$ is a relative measure that relates the depth of the transition layer, H, with respect to the wavelength in water. For example, for $k^f H = 40$ indicates that the layer thickness is approximately 6.37 times larger than the wavelength in water. Such a notation eliminates the need to have separate plots for different thickness or frequencies.

We first examine the effect of the angle of incidence on the amplitude of the reflection coefficients. In the case of a homogeneous half-space, the reflectance function is frequency independent, and as shown in Fig 2.14, we observe very distinct regions. First, at an angle of approximately 20.4º the amplitude of the reflection coefficient becomes unity. This is the longitudinal wave critical angle and it signifies that longitudinal wave has become a surface wave. At an angle of 50 º we observe the again the same phenomenon, but this time, the shear wave also has become a surface wave. The longitudinal wave and the shear wave at this angle combine to give rise to the Rayleigh surface wave, and the angle at which it appears is the Rayleigh angle. These characteristics are universal to all isotropic materials. The angles at which the surface waves occur however do depend on the material properties. We recall from the results of section 2.2.3

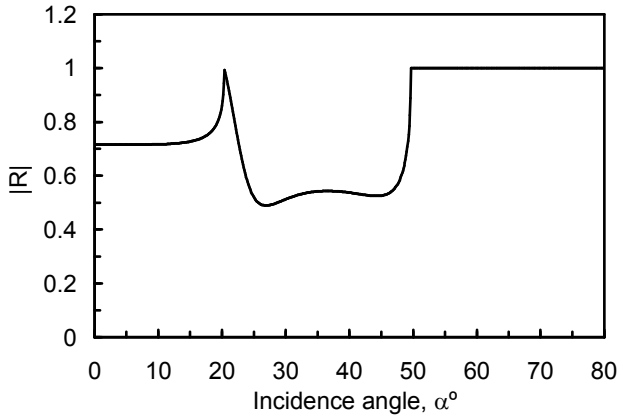


Figure 2.14 Amplitude of reflection coefficient with incidence angle for a homogeneous substrate

that for the acoustic objectives used in this work, the most significant contribution to the angular spectra comes from incidence angles not more than 18º. Therefore, it is expected that the effect of such waves will not be captured by these objectives. For the homogeneous substrate, and for angles <10º there is hardly any difference in the reflection coefficient amplitude compared to normal incidence. Between 10-20º the reflection coefficient amplitude rapidly rises to unity. Between the longitudinal and the Rayleigh angle, the amplitude of the reflection coefficient drops rapidly and has an undulating behavior. Beyond the Rayleigh angle, the amplitude of the reflection coefficient remains unity.

In Fig 2.15 we show the amplitudes of the reflection coefficients for a substrate with graded layer, for values of $k^f H$ of 0.42, 10.6, 29.6 and 42.2. On each plot, we superimpose the

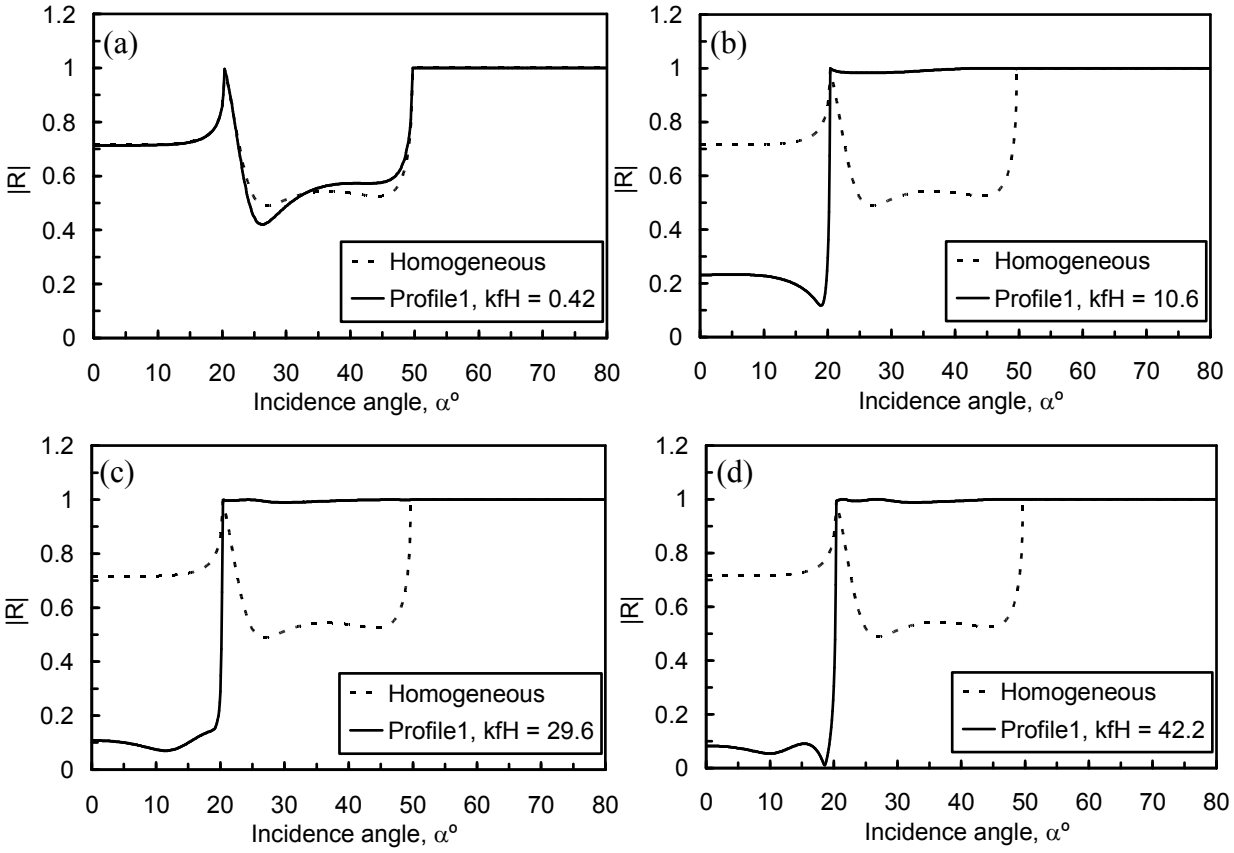


Figure 2.15 Amplitude of reflection coefficient as a function of incidence angle for $k^f H$ (a) 0.42, (b) 10.6, (c) 29.6 and (d) 42.2

reflectance function for the homogeneous substrate of Fig 2.14. Interestingly, at very low $k^fH$ numbers, the region before the longitudinal critical angle is less affected, while the region between the longitudinal and first Rayleigh angles is greatly affected. For higher $k^fH$ there is a significant reduction in the amplitude of the reflection coefficient before the longitudinal critical angle and the difference between the reflection coefficient amplitude at normal incidence becomes more prominent. The range between the longitudinal and the Rayleigh angles becomes almost indistinguishable. Material property quantification in conventional acoustic microscopy relies heavily on the generation of the acoustic surface waves, preferably Rayleigh waves, while the reflectance functions at small incidence angles are typically overlooked. However, even at small incidence angles, it is possible to discern differences that may reveal unique characteristics of a complex material.

In our subsequent discussion we show results up to angles of incidence within 18º, that are more relevant to the acoustic objectives used in this work. Three profiles of the elastic properties and density were considered for the graded-layer as shown in Fig 2.13. In Fig 2.16, we plot the amplitude of the reflection coefficients with respect to the non-dimensional number $k^fH$ for three angles of incidence, $\alpha$ = 0º, 10º and 18º. Under normal incidence, as shown in Fig 2.16(a), we observe that when the $k^fH$ is small, the amplitude of the reflection coefficient approaches that for the underlying substrate. However, for high $k^fH$ products, the amplitude of the reflection coefficient approaches that of the discontinuity between the fluid half-space and the top surface of the transition layer. This observation is consistent with theoretical considerations (Robins

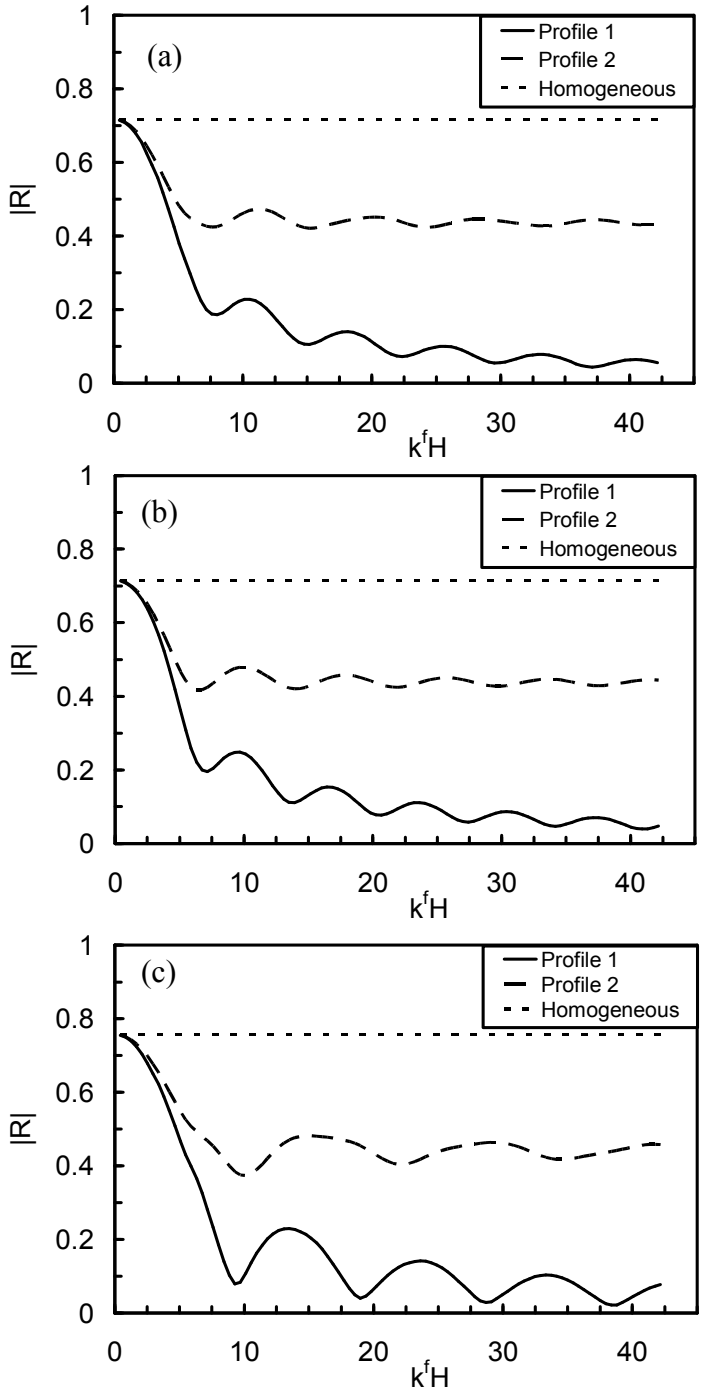


Figure 2.16 Amplitude of reflection coefficient as a function of $k^fH$ for angles of incidence (a) 0º, (b) 10º and (c) 18º

1990). The range over which the reflection coefficient varies with frequency is thus bounded. However, the greatest change in the reflection coefficient amplitude occurs at values of $k^f H$ between 1.5 and 6.28, which corresponds to thicknesses approximately 0.25 and 1 times the wavelength in the fluid half-space. As $k^f H > 6.28$ the behavior of the amplitude of the reflection coefficient becomes oscillating. At angles of incidence smaller than 18º (Figs 2.16b and c) the behavior with $k^f H$ is qualitatively similar as that of the normal incidence. However, the main lobe appears to have a change in its shape and becomes broader. Additionally, the oscillations become deeper while their repetition becomes slower which means that their minima occur at different $k^f H$. We note that the variation of density is limited from 1-2.1 $Mg/m^3$ and hence its effect is somewhat limited in contrast to the elastic properties where they are possible to have variations of an order of magnitude.

# 3.0 EXPERIMENT

## 3.1 SAM used in this work

A commercially available SAM (WINSAM 100, Kramer Scientific Instruments GmbH, Herborn, Germany) was used in this work. The ultrasonic objectives used included, a 30 MHz central frequency lens (KSI PT30-002) and a 110 MHz lens. The 30 MHz transducer specifications were as follows: nominal lateral resolution ≈ 100 µm, half aperture angle ≈ 13.4°, nominal focal length =12.7 mm and the -6dB amplitude bandwidth frequencies are 21.6 MHz and 38 MHz. Similarly, the 110 MHz transducer specifications were as follows: nominal lateral resolution ≈ 50 µm, half aperture angle ≈ 10°, nominal focal length =8.0 mm and the -6dB amplitude bandwidth frequencies are 28.9 MHz and 80.9 MHz. In the subsequent discussion we will refer to the KSI PT30-002 objective as "Transducer 1" and the 110 MHz transducer as "Transducer 2". The Fourier amplitude spectra for the two objectives used are shown in Fig 3.1.

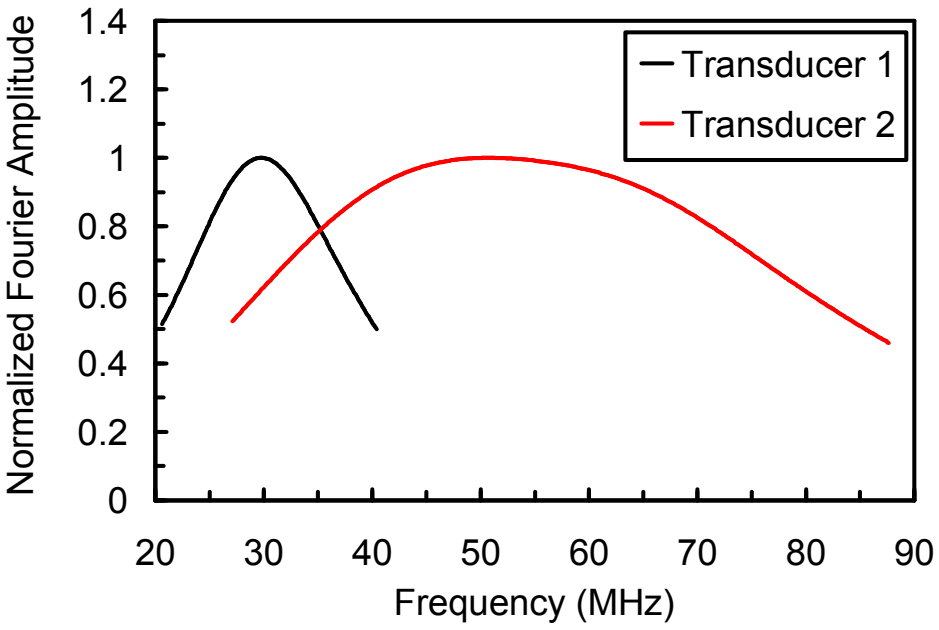


Figure 3.1 Transducer frequency spectra

## 3.2 SAM Calibration

Numerous researchers have used SAM in pulse-echo mode to directly measure material reflection coefficient and, consequently, acoustic impedance (Raum et al 2003, Hirsekorn et al 1995 and 1996, Prasad 2001, Katz et al 2001, 2003). The measurement of the reflection coefficient requires calibration of the received signal characteristics to the reflection coefficient of known materials. Theoretically, the received signal amplitude is a linear function of the material reflectance (Hirsekorn et al 1995 and 1996). However, it has been shown that the received signal may be significantly influenced by saturation effects due to system electronics at high amplifications (Raum et al 2003). The linear relationship between material reflectance and received signal characteristics may therefore lose validity. Furthermore, very often, higher amplification settings have to be used in order to obtain measurable signals from materials with very low reflection coefficients ($\sim<0.20$). In all these cases, the use of linear data fitting may greatly compromise the accuracy of the calculated micromechanical properties, especially when (1) the unknown material reflectance is outside the range of the calibration materials, and (2) the unknown material has heterogeneous reflectance varying over a wide range.

Furthermore the implicit assumption present in such calibration procedures is that the material reflection coefficient obtained independently (from literature or acoustic impedance measurements), and the reflection coefficient obtained from SAM measurements are identical. This is rarely the case since the scale of measurement using SAM is orders of magnitude smaller than bulk wave time of flight measurements and accurate volume displacement methods for density determinations require a sufficiently large sample. In the presence of non-linear amplification, any errors in estimating the reflection coefficients used for calibration may be amplified and that error will subsequently propagate to the determination of the "calibration-curves".

Therefore for accurate quantification of properties, conventional calibration methods with linear or nonlinear regression are not sufficient and a methodology is needed that can distinguish the effect of system electronics from the material response. Consequently, it is necessary to characterize the nonlinearity introduced by various system components. Since the characterization of nonlinearity emanating from each sub-system and component is highly intrusive, especially for commercial systems, we address the overall system behavior. In this work, the overall nonlinearity introduced by various system components is modeled using gain functions that are obtained for a variety of reference materials with reflection coefficients ranging from 0.21 to 0.97. Frequency domain methods are used to analyze the signals from SAM to obtain gain functions for various system amplification settings. These gain functions are found to depend upon both the material reflectance as well as the frequency at high amplification settings. These gain functions are then used to predict the relationships between reflection coefficients and Fourier amplitude. The advantage of the developed approach is that it is possible to separate the material effect from the system electronics effect. As a result, the errors in the measured reflection coefficient may be better defined. Moreover, the developed approach may be applied to detect frequency dependence of reflection coefficient due to material or surface properties. The developed gain functions are validated by comparison with independently measured reflection coefficient for two very low acoustic impedance materials: LDPE (reflection coefficient= 0.12) and TPX® (reflection coefficient= 0.09). These validated gain functions were then used to predict the reflection coefficients and acoustic impedance of unknown materials.

We represent the signal received by the piezoelectric element as

$$V(t) = \int_{-\infty}^{\infty} G(R,\omega) F_0(\omega) R(\omega) e^{-i\omega t} d\omega \tag{3.1}$$

where, $F_0$ (ω) is the incident wave-field's temporal frequency spectrum, and G(R, ω) is a amplification (or gain) function that is applied after the signal has been received by the piezoelectric element and R(ω) is the substrate's reflection coefficient which may be frequency dependent. Eq. 3.1 may alternatively be written in the frequency domain as a multiplication of the three functions as:

$$V(\omega) = G(R,\omega)F_0(\omega)R(\omega) \tag{3.2}$$

We note that in the case of an isotropic half-space, the reflection coefficient for normal incidence takes the form:

$$R = \frac{Z_B - Z_A}{Z_B + Z_A} \tag{3.3}$$

where $Z_A$ = acoustic impedance of coupling fluid (= $\rho_A c_A$), $Z_B$ = acoustic impedance of the specimen (=$\rho_B c_B$).

### 3.2.1 Calibration materials

The following materials were used in order to provide a wide range of reflection coefficients and acoustic impedances: tungsten, copper, brass, aluminum, vitreous carbon, silica glass, polyvinyl chloride (PVC), polyethylene terephthalate glycol (PETG), polycarbonate, polypropylene, high density polyethylene (HDPE), low density polyethylene (LDPE) and polymethylpentene (TPX®). For this set of materials, the acoustic impedance was determined by independently measuring longitudinal wave velocity and material mass density. The longitudinal speed of sound, c, in each of the materials was measured by the time of flight method using a 5 MHz contact transducer. Material density, ρ, was measured by Archimedes principle. The value of the theoretical reflection coefficient ($R^{th}$) of each material was then determined from Eq 3.3.

The speed of sound in water, $c_A$, was used as 1490 m/s for distilled water which corresponded to the average temperature of the water tank for a temperature range of 22-24ºC (Del Grosso and Mader 1972). Materials LDPE and TPX® were not part of the calibration, but their independently measured reflection coefficients were used to validate the calibration procedure. The reflection coefficients and impedances for the calibration materials are shown in Table 1.

Table 3-1 Calibration materials

| Material | | ρ (g/cm³) | c (m/s) | Z = ρ.c (MRayl) | $R_{th}$ |
|---|---|---|---|---|---|
| Calibration Materials | Tungsten (W) | 19.07 | 5222 | 99.58 | 0.97 |
| | Copper (Cu) | 8.72 | 4662 | 40.7 | 0.93 |
| | Brass | 8.37 | 4195 | 35.1 | 0.92 |
| | Aluminum (Al) | 2.76 | 6268 | 17.3 | 0.84 |
| | Quartz Glass | 2.20 | 5369 | 11.8 | 0.77 |
| | Vitreous Carbon | 1.48 | 4565 | 6.7 | 0.64 |
| | PVDF | 1.77 | 2047 | 3.6 | 0.41 |
| | PVC | 1.41 | 2366 | 3.3 | 0.38 |
| | PETG | 1.27 | 2325 | 2.9 | 0.33 |
| | Polycarbonate | 1.19 | 2270 | 2.7 | 0.29 |
| | Polypropylene | 0.90 | 2640 | 2.4 | 0.23 |
| | HDPE | 0.95 | 2439 | 2.3 | 0.21 |
| Validation Materials | LDPE | 0.91 | 2071 | 1.9 | 0.12 |
| | TPX® | 0.82 | 2180 | 1.7 | 0.09 |
| Couplant | Distilled Water | 1.00 | 1490 | 1.5 | - |

### 3.2.2 Data acquisition and analysis

The SAM and transducers described in 3.1 were used. In the pulse-echo mode, A-scan signals were recorded at different amplification (gain) settings. All the samples were placed at the focal plane of the transducer and the A-scan signals were recorded at the same location of a sample for different gain settings. The gain settings for transducer 1 were varied from -10 dB to 8 dB. For this range of gain settings measurable signals were obtained for all the calibration materials (materials with reflection coefficients > 0.21). For the transducer 2, gain settings ranged from 10 dB to 30 dB by increments of 2 dB. For the validation materials, LDPE and

TPX®, measurable signals were possible for gain settings of 0 dB and higher. For each calibration material, 32 waveform signals were captured, gated and averaged in order to increase signal to noise ratio. Same gate size was used for all the calculations. A Fast Fourier Transform (FFT) was used to obtain the frequency spectrum of the averaged signal for the frequency domain analysis.

The main objective is to characterize the gain function G(R, ω) of Eq 3.2. We note that each amplification setting has a different gain function. Additionally, each transducer will have different set of gain functions. We may think of G(R, ω) as a mapping or transfer function that modifies an input signal $F_0(\omega)R(\omega)$. To determine the gain function of the amplifier, we use the calibration materials whose reflection coefficients have been independently measured. We represent the received reflected signal amplitude, $V_i^m$ ,modified, in general, by the gain function G(R,ω), in the frequency domain as:

$$V_i^m(\omega) = R_i G(R,\omega) F_o(\omega) \tag{3.4}$$

where $F_o(\omega)$ is the Fourier transform of the incident signal, ω=cyclic frequency (=2πf), f = frequency, and $R_i$ is the reflection coefficient of the i-th material. If the gain function G(R,ω) is independent of the material reflectance and frequency, then the reflection coefficient of an unknown material, $R_{unkn}$, may be obtained through straightforward de-convolution using an independently characterized reference material of reflectance, $R_{ref}^{th}$ , as follows:

$$\left|R_{unkn}\right| = \frac{V_{unkn}^m(\omega)}{V_{ref}^m(\omega)}\left|R_{ref}^{th}\right|, \tag{3.5}$$

where, superscript m refers to the measured spectra. However, due to the non-linear behavior of system electronics at high amplifications, the gain function is likely to be dependent upon the frequency and material reflectance. To illustrate the effect of system non-linearity, we determine

the theoretical signal amplitude of the calibration materials using tungsten (W) as the known reference material and the theoretical reflection coefficients, $R_i^{th}$, given in Table 1 as:

$$V_i^{th}(\omega) = \frac{\left|R_i^{th}\right|}{\left|R_W^{th}\right|} V_W^m(\omega) \tag{3.6}$$

In Fig 3.2, we plot the measured Fourier amplitude at the central frequency ($f_c$) as the abscissa and the theoretical reflection coefficient from Table 1 as the ordinate for different gain settings.

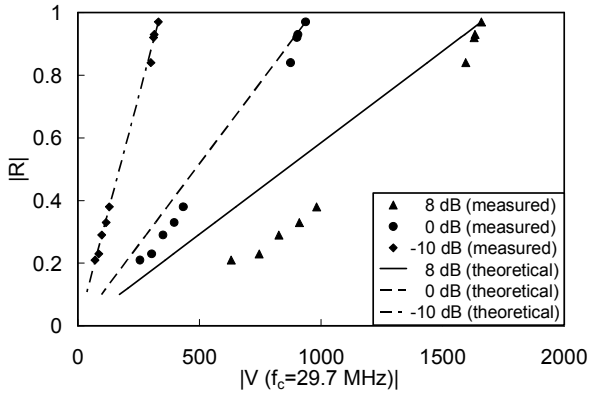


Figure 3.2 Reflection coefficient versus Fourier amplitude for transducer 1 at its central frequency

We see that the measurements exhibit increasing non-linearity as the gain settings are increased from -10 dB to 8 dB. This measured non-linearity reflects the saturation effects induced by the system electronics (Raum et al 2003). At 8 dB gain setting, the percentage deviations range from -90% to -3% for low to high reflectance material, while at 0 dB gain settings, the percentage deviations range from -37% to -1% for low to high reflectance material. At -10 dB, the deviations range from +1% to -10% and do not show any trend from low to high reflectance materials. The deviations at -10 dB are, therefore, considered to be a result of local variations in material properties, rather than the effect of system electronics.

To further illustrate the effect of system nonlinearity over the -6dB frequency bandwidth, we show the deconvolution of the measured spectra of the various materials with respect to the reference tungsten spectra in Fig 3.3. For materials with frequency independent reflectance, the deconvolution should yield a constant value of the normalized Fourier amplitude over the frequency range. From Fig 3.3, we see that at 0 and 8 dB gain settings, the normalized Fourier amplitudes show significant variations away from the central frequency for all the samples. At -10 dB, the normalized Fourier amplitudes show minor variations over the frequency range. The deviation from the constant value could be caused by local variations in material/surface properties, or

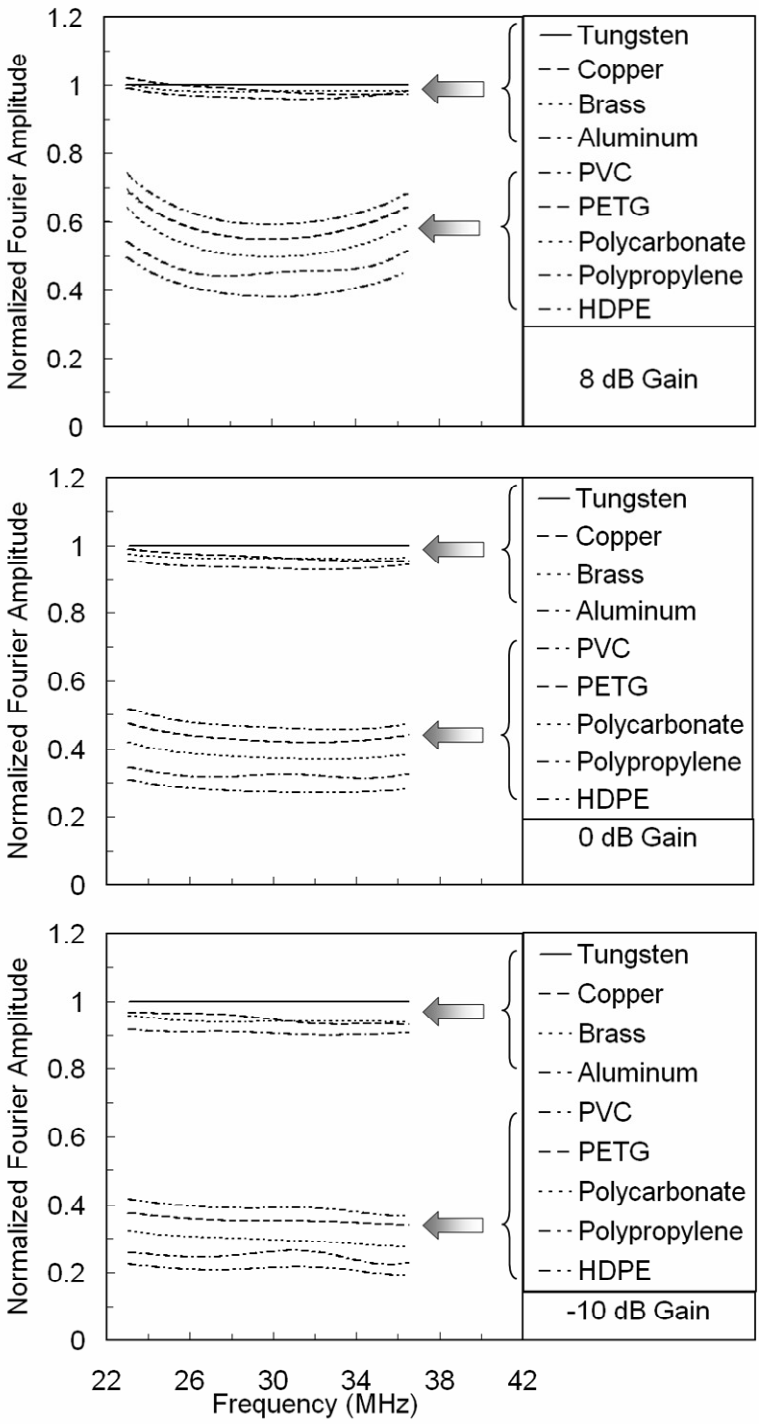


Figure 3.3 Deconvolution of measured frequency spectra with respect to tungsten spectra

effects of system electronics. As discussed previously, at -10 dB, we expect minimal effects of system electronics. Therefore, the deviations seen at -10 dB are expected to be from local variations in material properties. However, there is a limited range of material reflection coefficients over which we can utilize -10 dB gain setting. At this low gain setting, materials with very low reflection coefficients (~<0.2) provide a weak signal which falls within the noise floor. The problem becomes more acute for cases in which the unknown material has heterogeneous reflectance varying over a wide range; a case very often seen in biological samples. We illustrate the problem in Fig 3.4 which shows a caries affected tooth imaged at -10, 0 and 8 dB gain settings.

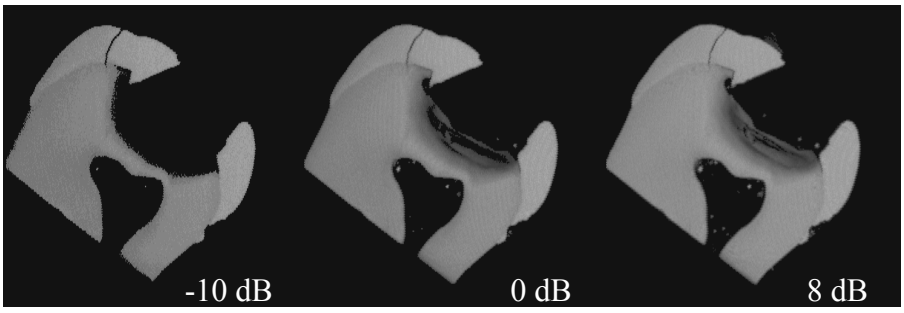


Figure 3.4 Caries affected tooth imaged at -10, 0 and 8 dB gain settings

The high reflectance regions of dentin and enamel are seen in all the 3 images, however the low reflectance caries affected regions are not visible at lower gain settings. Therefore for imaging low reflectance materials or material with heterogeneous reflectance, higher gain settings have to be used in order to obtain a measurable signal and a realistic image. Thus, the system electronics effects have to be considered in order to utilize the measured signal to accurately calculate the reflection coefficient. Consequently, a set of independently characterized calibration materials has to be used to establish the gain function, $G(R,\omega)$, for accurate determination of the unknown

reflection coefficient. In the past work using SAM, linear fits have been often used to relate the reflection coefficient and signal amplitude (Hirsekorn et al 1995 & 1996, Prasad 2001, Katz et al 2001, 2003). The linear fits or piecewise linear fits could lead to erroneous results when 1) the linear fit does not agree with the theoretical linear relationship, such as the measured data shown in Fig 3.2 for 0 and 8 dB gain settings, 2) the target material reflectance is outside the range of the calibration materials, and 3) the target material has heterogeneous reflectance varying over a wide range. Furthermore, the rationale for the choice of appropriate functional forms for nonlinear regression is unclear.

### 3.2.3 Gain Functions

For further development, we express the discrepancy between the measured Fourier amplitude spectra, $V_i^m$, at a given gain setting for the i-th calibration material and the theoretical Fourier amplitude obtained from Eq.3.4 as a sum of two parts:

$$V_i^m - V_i^{th} = \left(\Delta V_i^s + \Delta V_i^g\right) \tag{3.7}$$

where $\Delta V^s$ is the systematic discrepancy of the measured Fourier amplitude from the theoretical linear relationship due to local variations in material properties, and $\Delta V^g$ is the discrepancy from the theoretical linear relationship because of the system electronics. The systematic discrepancy, $\Delta V^s$, is obtained from the measurements at -10dB gain setting at which the system electronic effects are considered negligible (i.e. $\Delta V^g \approx 0$) using the following relationship:

$$\frac{\Delta V_i^s}{V_i^{th}} = \frac{\left|R_W^{th}\right|}{\left|R_i^{th}\right|}\left(\frac{\Delta V_i^s}{V_W^m}\right)_{-10dB} \tag{3.8}$$

We now define a scaled gain function, $\overline{G}_i^m$, obtained as the ratio of the measured Fourier amplitude corrected for the systematic discrepancy, $\Delta V^s$, and the theoretical Fourier amplitude written for the i-th calibration material as follows:

$$\overline{G}_i^m = \frac{V_i^m - \Delta V_i^s}{V_i^{th}} \tag{3.9}$$

The system electronics induced discrepancy, $\Delta V^g$, may then be obtained by combining (3.7) and (3.9) as follows:

$$\Delta V_i^g = V_i^{th}\left(\overline{G}_i^m - 1\right) \tag{3.10}$$

Fig 3.5 shows the plot of the scaled gain values versus the theoretical reflection coefficients for the central frequency, $f_c$, and -3dB bandwidth frequencies, $f_l$ and $f_h$, at 8, 0 and -10 dB gain settings for transducer 1. Clearly, at a given gain setting, the scaled gain values have an inverse relationship with reflectance. Thus the gain function serves to saturate the signal for high reflectance materials. Since the gain functions are not known for the system electronics, we obtain these through non-linear regression for the data in Fig 3.5 as follows:

$$\overline{G}(R,\omega) = a_1(\omega)\left(\frac{|R|-1}{|R|+1}\right) + a_o(\omega) \tag{3.11}$$

where $a_o(\omega)$ and $a_1(\omega)$ are frequency dependent fitting parameters for a given gain setting. We note that the 110 MHz transducer also exhibits the same behavior.

(a)

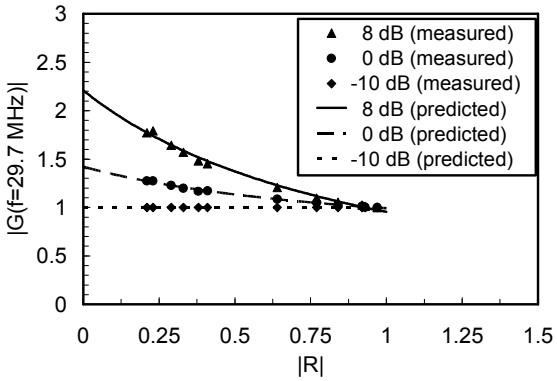


(b)

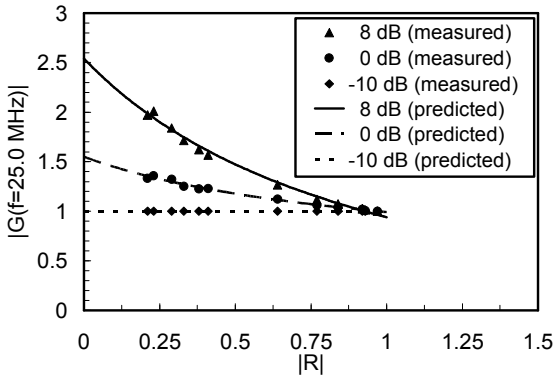


(c)

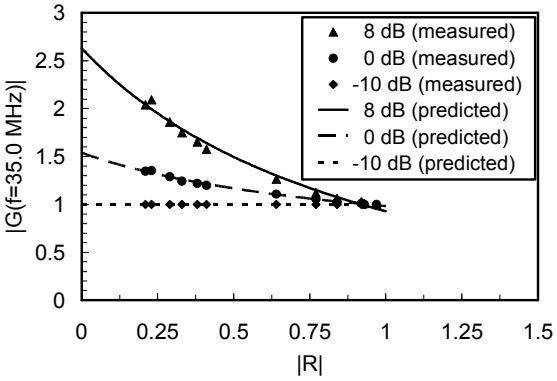


Figure 3.5 The gain function for (a) the -3 dB bandwidth frequency, $f_l$, (b) the central frequency, $f_c$, and, (c) the -3 dB bandwidth frequency, $f_h$ of transducer 1

### 3.2.4 Calibration curves

We utilize the obtained gain functions to predict the relationship between Fourier amplitude and reflection coefficient, given by combining Eqs 3.4 and 3.11 as follows:

$$V = |R|\overline{G}\frac{V_W^m}{|R_W|} = \left( a_1(\omega)\frac{|R|(|R|-1)}{(|R|+1)} + a_o(\omega)|R| \right)\frac{V_W^m}{|R_W|} \tag{3.12}$$

The predicted calibration curves for the transducer 1 are plotted in Figs 3.6 a, b and c, for the transducer central frequency, $f_c$, and the transducer -3dB bandwidth frequencies, $f_l$ and $f_h$, at 8, 0 and -10 dB gain settings. The calibration curves are shown by lines and the measured Fourier amplitudes are shown by symbols. Excellent agreement is obtained for gain settings of -10 and 0 dB. However, at 8 dB gain setting the predicted values slightly deviate for high reflectance materials. This deviation is a result of highly nonlinear behavior of gain function at such high gain settings. Similar plots are obtained for transducer 2 as shown in Figs 3.6 d, e and f at gain settings of 30, 20 and 10 dB.

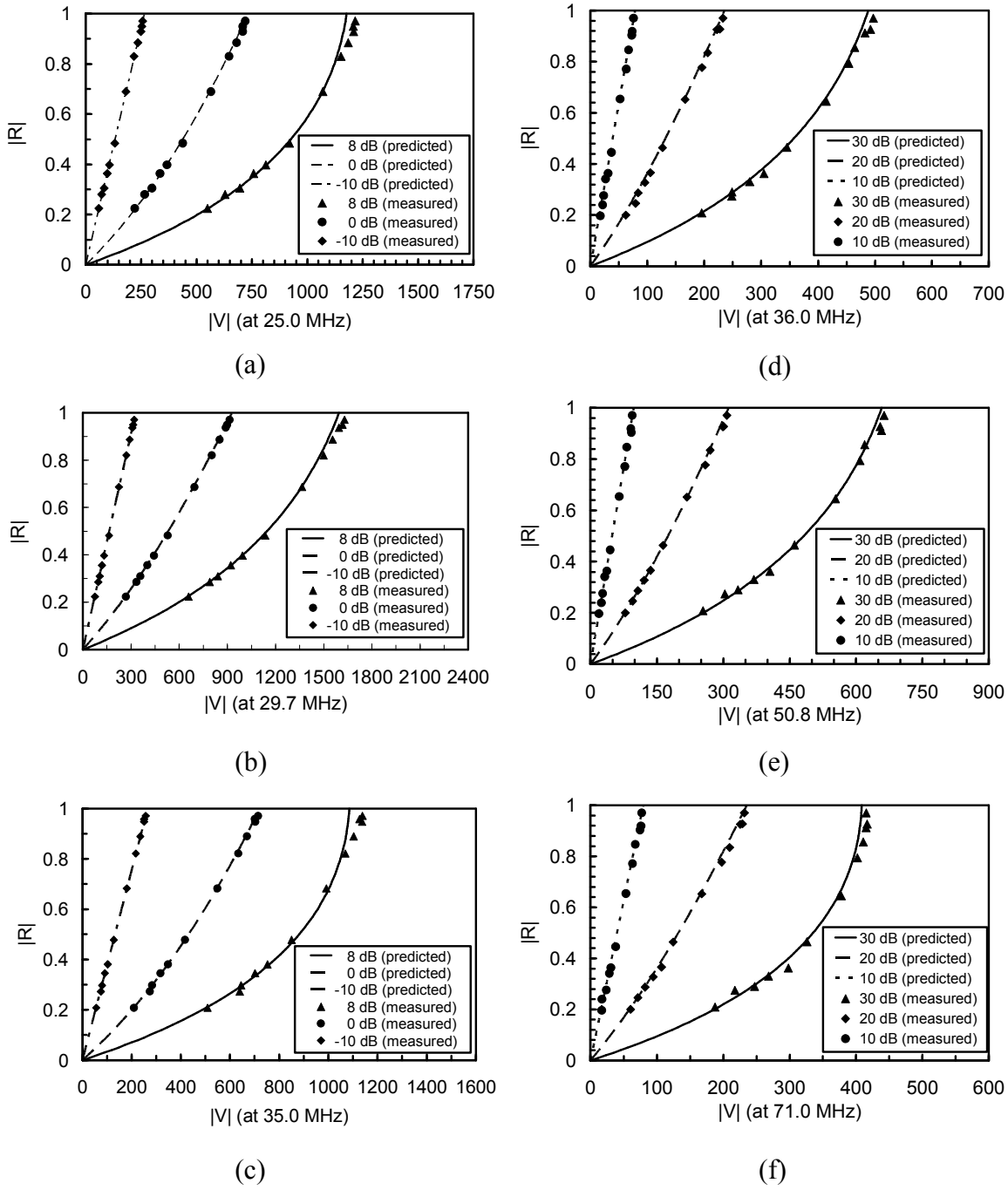


Figure 3.6 Predicted and measured relationship between Fourier amplitude and reflection coefficient for 3 different gain settings at (a) the -3 dB bandwidth frequency, $f_l$, (b) the central frequency, $f_c$, and, (c) the -3 dB bandwidth frequency, $f_h$. of transducer 1 and (d) the -3 dB bandwidth frequency, $f_l$, (e) the central frequency, $f_c$, and, (f) the -3 dB bandwidth frequency, $f_h$. of transducer 2

### 3.2.5 Prediction of LDPE and TPX® reflection coefficients

To validate the above relationships, we determine the reflection coefficient of LDPE and TPX® using the calibration curves and compare these with the theoretical reflection coefficients given in Table 1. These materials were chosen for validation because their reflection coefficients are smaller than those used to develop the calibration curves and these do not provide measurable signals at -10 dB gain setting. Thus, we can assess the applicability of the calibration curves for predicting reflection coefficients outside the range of the calibration materials. In Fig 3.7, we plot the reflection coefficients as a function of frequency over approximately the -6dB transducer bandwidth calculated using the calibration curves given by Eq. 3.12. For comparison, the independently determined theoretical reflection coefficients from Table 1 are shown as colored horizontal lines in Fig 3.7. Clearly, the developed calibration curves provide a closer prediction of unknown material whose reflection coefficient lies outside the range of calibration materials. Therefore, these validated calibration curves may be used to predict the reflection coefficients of unknown materials.

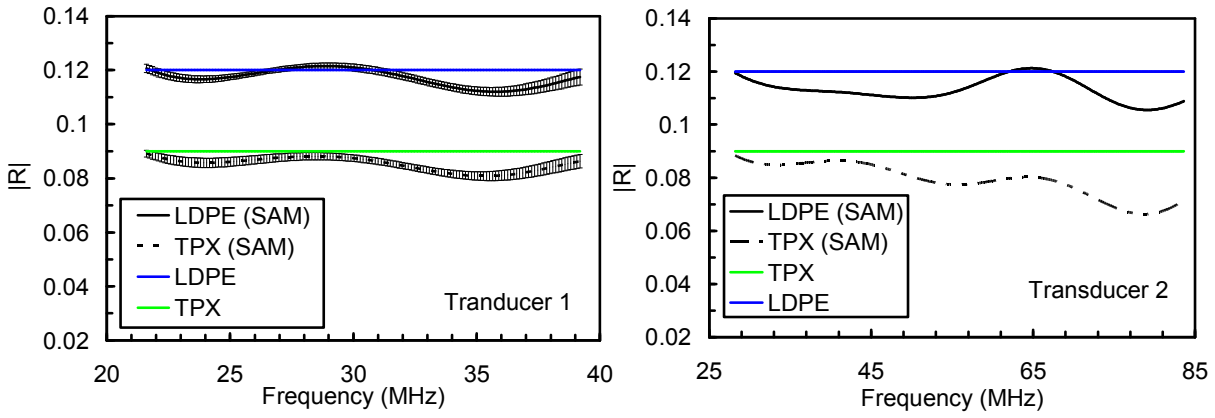


Figure 3.7 Prediction of LDPE and TPX®

### 3.2.6 Repeatability

We assessed the repeatability of the system by performing the calibration two consecutive days. In Fig 3.9, we show the results on the calibration curves obtained for transducer 2 at the central frequency. At the lower gain settings the change is undetectable and at higher gain settings the higher reflectance materials have a small error.

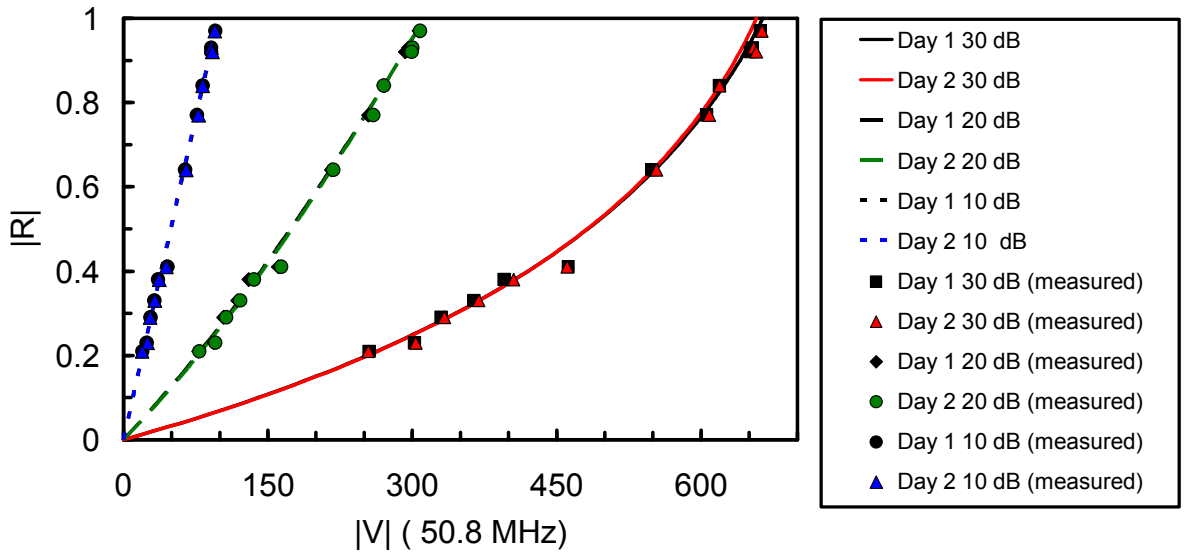


Figure 3.8 Calibration repeatability for transducer 2 shown at its central frequency

### 3.2.7 Error analysis

To determine the uncertainty on the reflection coefficient, we return to the calibration relationship given in Eq. 3.12. Solving for R (reflection coefficient of the unknown substrate) we end up with the solution for predicting R from the measured Fourier amplitude at a particular frequency as:

$$R = \frac{1}{2(a_0 + a_1)}\left[\left(\frac{V}{V_w}\right)R_W - a_0 + a_1 + \sqrt{\left(\frac{V}{V_w}\right)^2 R_W{}^2 + 2\left(\frac{V}{V_w}\right)R_W(a_0 + 3a_1) + (a_0 - a_1)^2}\right] \tag{3.13}$$

where absolute value signs are implied. Based on the 32 A-scan signals at the same location of each calibration material, the standard deviation of the Fourier amplitude was found to be 3 units and it is normally distributed about the mean Fourier amplitude. In addition, the standard deviation of the Fourier amplitude was also not changing for all the reference materials over the useful transducer bandwidth and as different amplification settings were applied. The uncertainty of the measured Fourier amplitude was therefore 3 units and can therefore be attributed to random noise. Since we use tungsten (W) as the reference material, the measured Fourier amplitude of tungsten also has the same uncertainty of 3 units.

We may treat V and $V_w$ as two separate variables which are independent and whose uncertainty is random. By that assumption, the error on the reflection coefficient can be given as (Taylor 1997):

$$\varepsilon_R = \sqrt{\left(\frac{\partial R}{\partial V}\varepsilon_V\right)^2 + \left(\frac{\partial R}{\partial V_w}\varepsilon_{V_w}\right)^2} \tag{3.14}$$

Carrying the partial differentiations we obtain:

$$\frac{\partial R}{\partial V}=\frac{R_w}{2V_w(a_0+a_1)}\frac{\left(\left(\frac{V}{V_w}\right)R_w+(a_0+3a_1)+\sqrt{\left(\frac{V}{V_w}\right)^2R_W{}^2+2\left(\frac{V}{V_w}\right)R_W(a_0+3a_1)+(a_0-a_1)^2}\right)}{\sqrt{\left(\frac{V}{V_w}\right)^2R_W{}^2+2\left(\frac{V}{V_w}\right)R_W(a_0+3a_1)+(a_0-a_1)^2}} \tag{3.14a}$$

$$\frac{\partial R}{\partial V_w}=-\frac{VR_w}{2V_w{}^2(a_0+a_1)}\frac{\left(\left(\frac{V}{V_w}\right)R_w+(a_0+3a_1)+\sqrt{\left(\frac{V}{V_w}\right)^2R_W{}^2+2\left(\frac{V}{V_w}\right)R_W(a_0+3a_1)+(a_0-a_1)^2}\right)}{\sqrt{\left(\frac{V}{V_w}\right)^2R_W{}^2+2\left(\frac{V}{V_w}\right)R_W(a_0+3a_1)+(a_0-a_1)^2}} \tag{3.14b}$$

Therefore, the error on the reflection coefficient may be written as:

$$\varepsilon_R=\frac{R_w\sqrt{1+\left(\frac{V}{V_w}\right)^2}}{2(a_0+a_1)}\frac{\left(\left(\frac{V}{V_w}\right)R_w+(a_0+3a_1)+\sqrt{\left(\frac{V}{V_w}\right)^2R_W{}^2+2\left(\frac{V}{V_w}\right)R_W(a_0+3a_1)+(a_0-a_1)^2}\right)}{\sqrt{\left(\frac{V}{V_w}\right)^2R_W{}^2+2\left(\frac{V}{V_w}\right)R_W(a_0+3a_1)+(a_0-a_1)^2}}\left[\frac{\varepsilon_V}{V_w}\right] \tag{3.15}$$

In Figs 3.10 and 3.11 we plot Eq. 3.15 with respect to the ratio $V/V_w$, for a value of $\varepsilon_v=3$ for both transducer 1 and 2. For each objective, three frequencies are considered, the two lower -3 dB

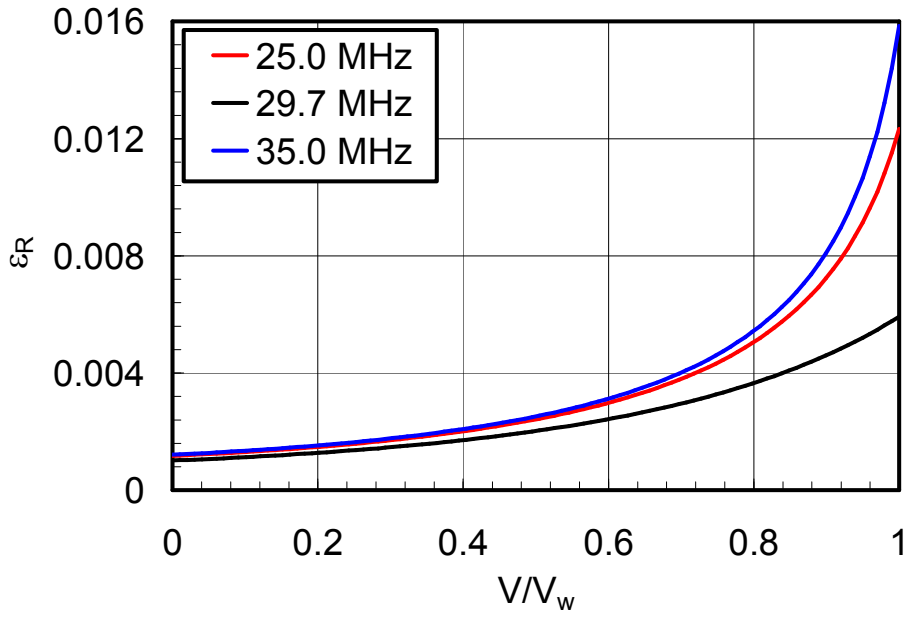


Figure 3.9 Reflection coefficient error analysis for transducer 1 at 6dB gain setting

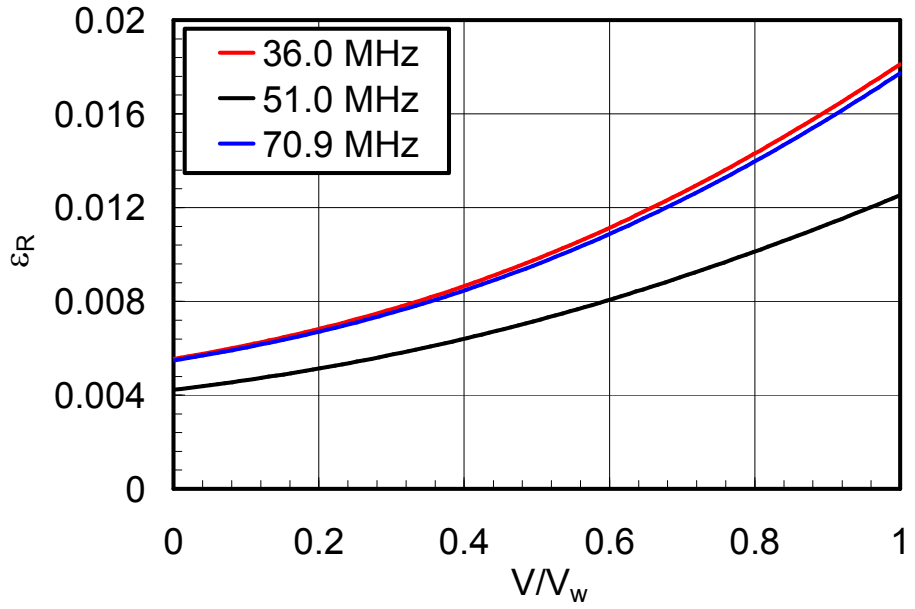


Figure 3.10 Reflection coefficient error analysis for transducer 2 at 24 dB gain setting

frequencies and the central frequencies which were, 25.0 MHz, 29.7 MHz and 35.0 MHz for transducer 1, and 36.0 MHz, 51 MHz 70.9 MHz for transducer 2. The corresponding gain settings were 6 dB gain setting for transducer 1 and 24 dB for transducer 2. The parameters $a_0$ and $a_1$ for transducer 1 were, 0.96 and -1.27 at 25.0 MHz, 0.97 and -0.98 at 29.7 MHz, 0.95 and -1.32 at 35.0 MHz. Similarly for transducer 2, parameters $a_0$ and $a_1$ are given as, 0.97 and -0.59 at 36.0 MHz, 0.99 and -0.54 at 51 MHz, 1.01 and -0.63 at 70.9 MHz.

We observe that the error on the reflection coefficient becomes larger at the edge frequencies than the central frequencies, which is consistent between the two transducers. This is explained by observing the bracketed term of Eq. 3.15. This term may be represented as a signal to noise ratio with respect to the tungsten Fourier amplitude. Amplitudes close to the central frequency are higher and noise amplitude remains constant, then the signal to noise ratio is higher. Furthermore we observe that error on the reflection coefficient increases in a nonlinear

fashion as the measured Fourier amplitude becomes closer to tungsten. This is an implication of the specific nonlinear behavior of the amplifier close to saturation. However, we note that for the Fourier amplitudes measured from the dentin substrate, the error on the reflection coefficient is approximately 0.01.

## 3.3 Homotopic Measurement

With recent advances in experimental methods, the characterization of biological tissues and biomimetic materials has been made possible at increasingly high spatial resolutions. For elucidating the interrelationship between physical, chemical and mechanical properties, complementary high resolution methods are required. However, when complementary methods are applied on highly heterogeneous materials, such as calcified tissues, it is especially important that the measurements are performed at the same location. Recently, we have introduced the term homotopic *(Greek homos = identical and topos = place)* (Marangos et al 2009) to describe the measurement of physico-mechanical properties performed at the same location of the same sample.

Relatively few attempts have been made to perform homotopic measurement of the micro-scale elastic moduli, composition and density of calcified tissues. Most of these investigations have used destructive indentation techniques for the micromechanical property determination. In the past decade, some investigators have combined ultra-micro or nanoindentation with backscattered scanning electron microscopy (BSEM) to study the relationship between mechanical properties and mineral content of a variety of calcified tissues (Angker et al 2004, Bembey et al 2005, Ferguson et al 2003, 2004). Nanoindentation has also been used in combination with atomic force microscopy (AFM), Fourier-transform infrared

microspectroscopy (FTIR), small angle x-ray scattering and BSEM to relate hardness and elastic modulus to a variety of structural and compositional properties of dentin (Tesch et al 2001, Gupta et al 2005). More recently, nanoindentation has been used with time-of-flight secondary ion mass spectroscopy to image same regions of *in vitro* carious lesions in human dental enamel (Dickinson et al 2007).

Non-destructive methods as an alternative to nanoindentation, have rarely been used in homotopic measurement for the correlation of mechanical properties, composition and density of calcified tissues. The advantage of non-destructive methods is that sample is preserved in its natural state for analysis with other complementary techniques. Among the earliest efforts to use non-destructive methods is the work by Katz and Meunier (1993) in which the same regions of human and canine osteons were imaged using backscattered scanning electron microscopy (BSEM) and scanning acoustic microscopy (SAM). The contrast in the SAM images was explained upon the basis of mineral density variations observed in the BSEM images. More recently, Turner et al (1999) have measured elastic moduli using SAM and compared it to nanoindentation measurements at similar locations on adjacent sections. SAM has also been used in conjunction with synchrotron radiation micro computed tomography (Raum et al 2006a, b) and in combination with Raman micro-spectroscopy and nanoindentation (Hofmann et al 2006) to obtain site matched mechanical and compositional properties.

Furthermore, multi-scale measurements require to be performed with multiple resolution instruments. Since natural materials have properties that vary from location to location or respond in a heterogeneous manner to surface treatments, it becomes extremely important that complementary measurements are performed at the same location. Moreover, for multiple

resolution determinations, the lower resolution measurement is necessary to contain the same ensemble of material points measured at the higher resolution.

In this work, the research protocol requires the specimen to be imaged in SAM before and after acid-etching treatment. Since the etching process cannot be performed in situ, it is necessary that the specimen be moved and placed back in the measuring system. As part of this requirement, a prototype device was developed that ensures tracking of the same locations that were measured before etching. Such device was necessary for meaningful comparison of pre and post acid-etching states.

### 3.3.1 Specimen holder for homotopic measurement

A prototype device was designed to obtain homotopic measurements the SAM described in 3.2.3. It consists of a steel block, with a circular depression on which the specimen will be mounted as shown in Fig 3.11a. A perforated sheet with a regular array of 400 μm openings was

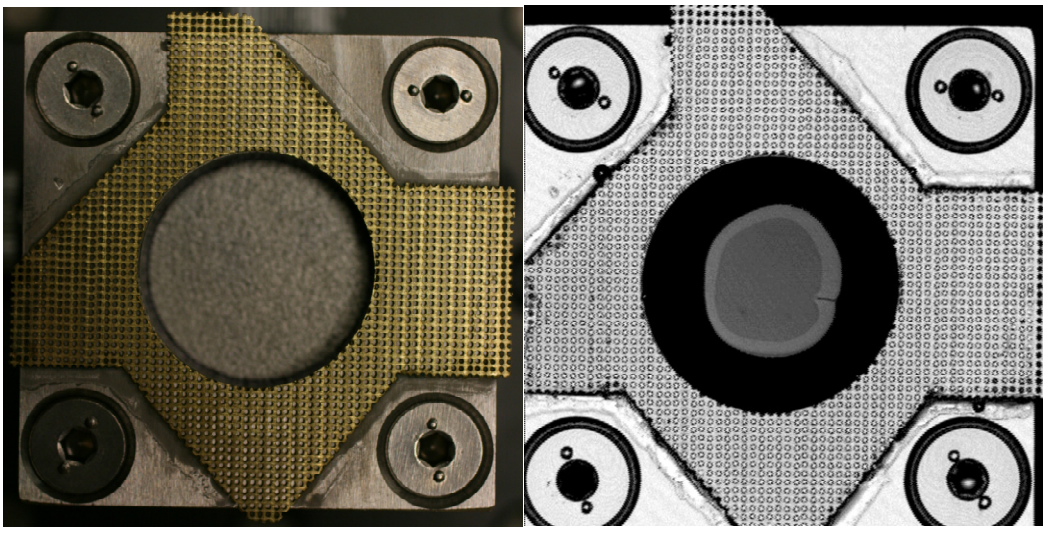

(a) (b)

Figure 3.11 Device for homotopic measurements (a) optical image (b) SAM image

fixed on the surface of the block. The size of the openings was chosen such that it would be resolved by the SAM transducers used in this study. A SAM image of the assembly with the specimen mounted is shown in Fig 3.11b. The specimen is rigidly mounted on the device and remains so throughout the testing schedule.

### 3.3.2 Principles

During the movement and re-placement of the specimen/device assembly, it is reasonable to assume that there is no relative movement between material points and the specimen may experience a rigid body displacement and rotation. In Fig 3.12 we show two placements of the

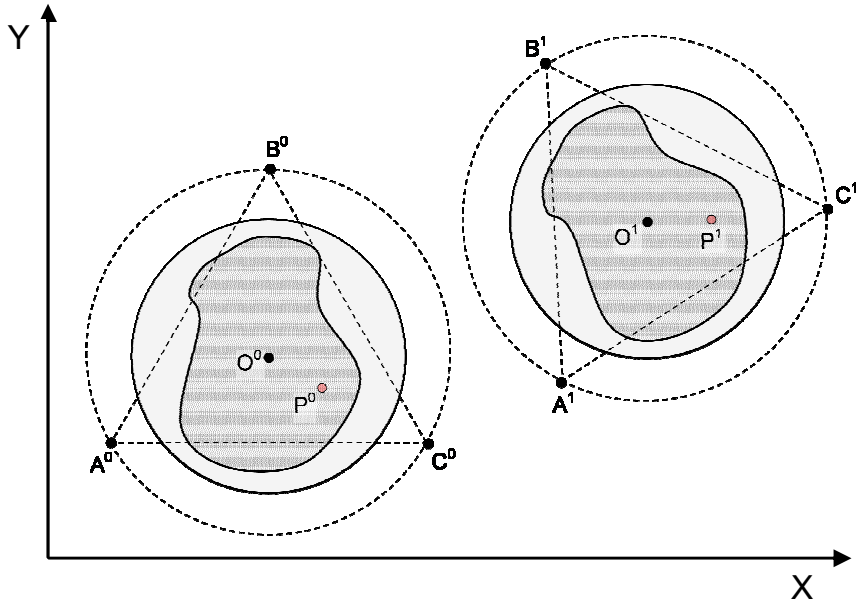


Figure 3.12 Initial and final placements of specimen in SAM

sample-holder. We use superscripts *0* and *1* to distinguish between initial and final placements. Point P denotes the location of interest on the specimen and our goal is to return to P with the highest accuracy in the subsequent measurements. Our goal is to be able to identify $P^0$ with the

highest accuracy in the subsequent measurements. To establish the final position of any location P on the specimen, we need to know the initial and final positions only of a few selected locations. These locations correspond to the vertices of an equilateral triangle A, B and C which are tracked throughout the experiment. At the initial placement, the spatial coordinates of vertices, $A^0$ ($X^0_A$, $Y^0_A$), $B^0$ ($X^0_B$, $Y^0_B$), $C^0$ ($X^0_C$, $Y^0_C$) as well as those of $P^0$ ($X^0_P$, $Y^0_P$) on the specimen are known with respect to a global coordinate system [X, Y]. This is the case as the SAM used is equipped with a positioning stage that provided the spatial coordinates of all the measured locations with respect to the stage's global coordinate system. The vertex positions are associated with the A, B and C were determined by acquiring an image. By sizing the feature to be slightly larger (~4 times) than the resolution of the imaging modality, it was possible to resolve the boundary of the opening and the locations within it.

For convenience, we define a local right-handed coordinate system. This local system moves with the specimen/device assembly. The local y-axis is aligned with the triangle edge AB with the positive direction pointing towards B. The origin of the local coordinate system is placed at A. The coordinates of a location P with respect to the local coordinate system may be found through a coordinate transformation as:

$$\{\mathbf{x_P}\} = \left[\mathbf{T^0}\right]^T \left\{\mathbf{X}^0{}_P - \mathbf{X}^0{}_A\right\} \tag{3.16}$$

The components of matrix [$\mathbf{T^0}$] are functions of the vertex coordinates at the initial placement and are given as:

$$\left[T^0\right] = \frac{1}{\sqrt{(X^0_B - X^0_A)^2 + (Y^0_B - Y^0_A)^2}} \begin{bmatrix} Y^0_B - Y^0_A & -(X^0_B - X^0_A) \\ X^0_B - X^0_A & Y^0_B - Y^0_A \end{bmatrix} \tag{3.17}$$

At the final placement, the new global coordinates of vertices $A^1$ ($X^1_A$, $Y^1_A$), $B^1$ ($X^1_B$, $Y^1_B$), $C^1$ ($X^1_C$, $Y^1_C$) are established by again identifying the corresponding features in a similar fashion.

With the new vertex coordinates established, and since we already know the local positions of P with respect to the local coordinate system, we then seek the new global coordinates of location $P^1$ ($X^1_P$, $Y^1_P$). The process may be described as a coordinate transformation from the local coordinate system, to the new global coordinate system as:

$$\{\mathbf{X^1_P}\} = [\mathbf{T^1}]\{\mathbf{x_P}\} + \{\mathbf{X^1_O}\} \tag{3.18}$$

The components of the transformation matrix $[\mathbf{T^1}]$ and circumcenter vector $\{\mathbf{X^1_O}\}$ are now functions of the vertex coordinates at the final placement.

Combining Eqs. 3.13 and 3.15 we may obtain the global coordinates of location P in the final placement as a function of the global coordinates of location P in the initial placement and the vertex coordinates in the initial and final placements as:

$$\{\mathbf{X^1_P}\} = [\mathbf{T^1}][\mathbf{T^0}]^T \{\mathbf{X^0}_P - \mathbf{X^0}_O\} + \{\mathbf{X^1_O}\} \tag{3.19}$$

## 3.4 Dentin Structure, Composition and Mechanical Properties

Dentin is a mineralized tissue that forms a bulk of a tooth body. Dentin composition is approximately 30-35% organic material, 45-50% inorganic material, and 20% fluid by volume. The organic component is predominantly type I collagen with minor contribution from other proteins, while inorganic component is a carbonate rich, calcium deficient apatite mineral deposited within collagen fibril (Marshall et al 1997, Gage et al 1989, Linde 1989, Butler 1992, Arsenault 1989). The interactions between collagen and nanocrystalline mineralite gives rise to the stiffness of the dentin structure. The consequent dentin elasticity is an important feature that determines the mechanical behavior of the tooth structure.

The structural characteristics of sound dentin are well known at the micro-scale (100 μm). Dentin is described as a system of dentinal tubules surrounded by a collar of highly mineralized peritubular dentin (Wang and Weiner 1998) as shown in Fig 3.13. The tubules traverse the structure from the pulp cavity to the region just below the dentin-enamel junction

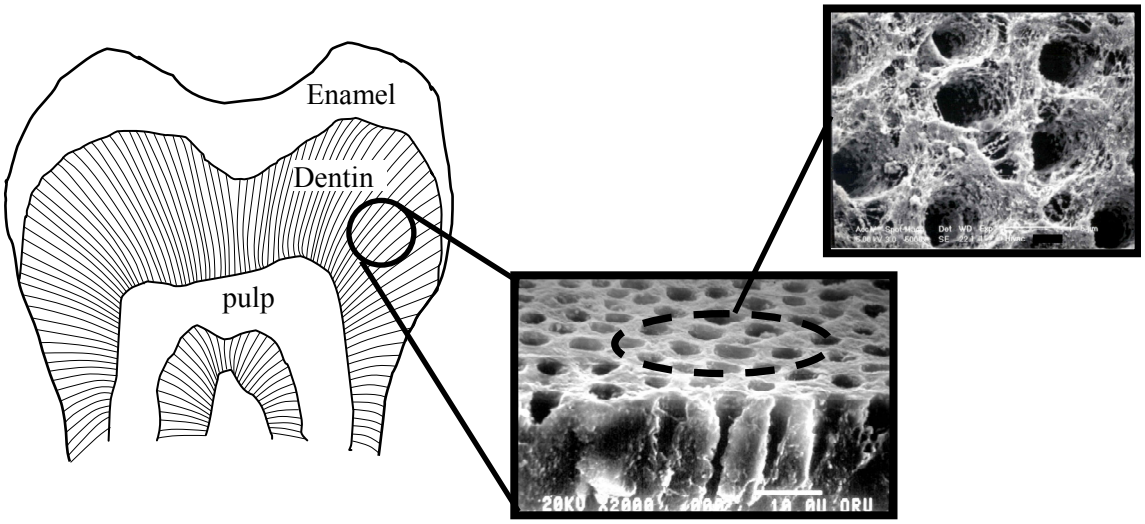


Figure 3.13 Dentin microstructure (adapted from Misra et al 2005)

(DEJ) or the dentin-cementum junction (CEJ). Tubule density, size and orientation vary from location to location. The density and size are lowest close to the DEJ and highest at the predentin surface at the junction to the pulp chamber. Thus, the porosity of dentin varies from 0.5% to 25% from the DEJ to the pulp (Manly and Deakins 1940, Sumikawa et al 1999, Koutsi et al 1994). The composition of the peritubular dentin is carbonated apatite with very small amounts of organic matrix whereas intertubular dentin, i.e., the dentin separating the tubules, is type I collagen matrix reinforced with apatite. Water in dentin may be classified as either free or bound. Water is present within the dentinal tubules as pulpal fluid and within the interstitial spaces between collagen fibrils. Based upon experimental chemical microanalyses, bound water

is likely present as hydroxyl groups bound to the mineral component (Gruner et al 1937, Bird et al 1940, LeFevre et al 1937).

Beginning in 1960s, macro-scale elastic moduli of dentin have been measured by a variety of methods as reviewed by Kinney et al. (2003). Using nanoindentation methods, Kinney et al. (1999), have measured the elastic modulus of peri-tubular dentin and inter-tubular dentin. At somewhat larger, unspecified micrometer scales, Katz et al. (2001) measured similar values of dentin elastic modulus using SAM. At even higher scales, Lees and Rollins (1972) used longitudinal and shear wave velocity measurements, Kinney et al (2004) used resonant ultrasound spectroscopy to determine elastic moduli of millimeter scale samples, and John (2006) used longitudinal velocity measurements on approximately millimeter thick slices to find location dependent elastic moduli.

## 3.5 Characteristics of Acid-Etched Dentin

Since the replacement of the amalgam by acrylic composite fillings, the problem of bonding composite restorations to dentin has become the "Lernaean Hydra". As it is well known, the native tooth surface, is supposed to provide the foundation that supports composite fillings. A necessary step to complete the bond between the dentin surface and the filling, is the application of polymeric adhesives. During cavity preparation, the exposed tooth surface is left with a layer of debris known as the "smear layer" (Kramer and McLean 1952, Eick 1992). The presence of this smear layer, proved to be the culprit for the premature failure of early resin composite restorations, as it occluded the dentinal tubules with smear plugs and prohibited bonding of the adhesive to the native tooth structure. Buonocore (1955), in order to improve composite restorations on enamel, suggested exposing the dentin surface to a phosphoric acid

treatment for a short time (a few seconds) as a conditioning step before adhesive application. The addition of this step proved very successful in enamel bonding, but when it was later attempted for bonding on dentin, did not perform quite as well. Although the phosphoric acid etching step served its intended purpose of removing the smear layer from the dentin surface, it also completely altered the near-surface of the exposed dentin creating a new and unknown substrate, different from the native tissue. The unexpected outcome of the etching regime was the removal of the mineral from the first few micrometers of dentin leaving behind a porous collagen scaffold (Pashley et al 1993, Kinney et al 1995). Consequently, the interface resulting from subsequent application of the adhesive system was a highly heterogeneous composite of collagen, mineral and adhesive monomer, known now as the "hybrid layer" (Nakabayashi et al 1982). Since then, researchers in clinical dentistry have been working to understand the effects that acid etching imposes on dentin and its relationship to bonding efficiency and to develop alternative conditioning techniques and adhesive formulations compatible with the etched substrate.

To evaluate the sub-surface structural alterations that acid-etching imposes on dentin Scanning and Transmission Electron Microscopy (SEM and TEM) studies have been performed. Van Meerbeek et al (1993) through high resolution SEM and TEM observations showed that the near-surface of acid-etched inter-tubular dentin was separated into three distinct sub-layers. The first layer was comprised of collapsed disorganized collagen. Below it, the collagen showed partial structure with sparse instances of residual mineral. The third layer was a partially de-mineralized zone that transitioned to the deeper native dentin. There has been concern (Eick 1992, Nakabayashi et al 1992, Spencer and Swafford 1999) that the top denatured collagen layer could inhibit to the subsequent infiltration of adhesive. Kinney et al (1995) using Atomic Force

Microscopy (AFM) and X-ray tomography attempted to quantify the dimensional changes that occur in fully hydrated dentin during demineralization with lactic acid and to relate them to the mineral density distribution as a function of depth. Their work, suggested that the tubule orifices become wider by removal of the more mineralized peritubular dentin. Their work also indicates, that the mineral density distribution is affected by two different rates of de-mineralization, one related to the fast transport of acid through the tubule orifices, and one associated with the slower diffusion of the acid through the de-mineralized collagen layer. However, the extent of demineralization of the acid-etched zone as well as the effects on the tubule orifice widening has been shown to vary with the conditioner used, the concentration of the conditioner, time of exposure and technique (Oliveira et al 2002, Susin et al 2008, Wang and Spencer 2004). Furthermore, the extent of demineralization has been shown to depend on the substrate as dentin may be sclerotic or affected by caries (Marshall et al 2000, 2001).

The profile and extent of inter-tubular dentin de-mineralization under short-term clinically relevant exposure to acid etching has been most effectively shown using infrared and micro-Raman Spectroscopy (Suzuki et al 1991, Wieliczka et al 1997, Lemor et al 2000, Spencer et al 2000, Wang and Spencer 2003, Santini and Miletic 2008). Results from these studies, have shown clearly that the adhesives were unable to completely infiltrate the dentin etched-surface. From these studies the extent of the de-mineralized zone was approximately 20 μm.

Topographical effects of acid-etching on dentin such as roughness and surface recession have been observed by AFM and profilometry. Oliveira et al (2002) has shown that after etching, the surface recession after few seconds of etching was found to be less than 1 micron, provided that dentin remains fully hydrated. AFM based roughness measurements of de-mineralized dentin (Rosales et al 1999, Oliveira et al 2002, Shuyean et al 2009) show an increase

in roughness and are consistent with profilometric studies (Toledano et al 1999). However, roughness measurements depend upon the exposed surface with regards to tubule orientation. Mechanical property measurements of etched dentin are very scarce. Balooch et al (1998) used AFM-based indentation under small deformations reported the visco-elastic and elastic values of de-mineralized dentin. According to their work, hydrated dentin had a very low Young's modulus of elasticity ~0.2 MPa whereas de-hydrated was ~2 GPa. However, indentation studies are very challenging for substrates such as etched dentin and the interaction of the indent with a graded substrate is not well defined. Pashley et al (2003) through miniature compressive and tensile stress-relaxation and creep tests concluded that completely de-mineralized dentin exhibited non-linear viscoelastic effects. Quantitative characterization techniques have increased our understanding of the morphological and ultra-structural characteristics of the near-surface of acid-etched dentin. However, there is still a big gap in our knowledge of the mechanical properties of acid-etched dentin as well as how these properties influence the interpretation of the experimental measurements of mechanical and physical properties.

## 3.6 Application of SAM to dental materials

In one of the earliest efforts in application of SAM in dental materials (Peck and Briggs 1987, Peck et al. 1989) carious enamel lesions were imaged at a spatial resolution of approximately 4 μm. Even though the work was largely qualitative, they recognized the sensitivity of SAM in detecting small changes in elastic properties of enamel and the existence of an intimate relationship to the level of de-mineralization. Kushibiki et al. (1987) in an attempt to investigate the visco-elastic properties of dental hard tissues, performed SAM measurements on human enamel and dentin using line focus (cylindrical lens) at 225 MHz and point focus

(spherical lens) at 400 MHz at a resolution of ~ 3 μm. They came to the conclusion that the surface acoustic wave velocities and attenuations in both enamel and dentin had a marked variation with frequency, position and direction. More recently, Zheng et al (2000) used acoustic microscopy at 25, 50 and 100 MHz for obtaining acoustic impedance images. In addition, Maev et al (2002) used acoustic microscopy at frequency of 50 MHz in reflectance mode to obtain images and time of flight at 25 μm resolution. In the same study they used transmission mode with contact transducers to measure time of flight at 20 MHz. Acoustic wave velocities in mantle dentin near the enamel were 7% to 8% less than in bulk dentin at approximately 100 μm resolution. Katz et al. (2001 and 2003) used SAM at 400 MHz and inferred the mechanical properties of mineralized, partially de-mineralized and completely de-mineralized dentin through a series of calibration curves. More recently, Raum et al. (2007) used acoustic microscopy at 50 MHz (23 μm resolution) to study the effect of storage media on the acoustic properties of enamel and dentin. This work pointed out the need for understanding how the microstructure affects the interpretation of the acoustic measurement.

## 3.7 Dentin Specimen Preparation

For the experimental component of this work, a human unerupted 3rd molar with no visual caries was used under an IRB approved protocol. The specimen preparation proceeded as follows: the cervical third, right below the neck of the tooth, was sectioned perpendicular to its long axis by means of a $H_2O$-cooled low-speed diamond saw (Buehler, Lake Bluff, IL). Subsequently, the occlusal crown was removed resulting to an approximately 5 mm slab of mid-coronal dentin as shown in Fig 3.14.

Figure 3.14 Dentin specimen

To remove surface irregularities such as saw marks and the smear layer caused by the diamond saw the specimen was polished successively by 600 and 1200 grit size abrasive papers followed by a few passes with a polishing cloth (Buehler, Lake Bluff, IL). An alternative protocol for removing the smear layer was evaluated which included micro-toming approximately a 5 μm section from the surface. Micro-toming was evaluated as previous researchers have suggested that polishing has a tendency to alter the surface microstructure by smearing the collagen and mineral (Ho et al 2004). We found that micro-toming generally resulted in some damage of the dentin structure and even more at the vicinity of the DEJ. The damage was especially evident in SAM as shown in Fig 3.15. In contrast, hand polishing using 600 to 1200 grit paper produced uniform and smooth surfaces for SAM analysis. We also found that the results from SAM were not affected provided the polishing was done by applying a light pressure and the surfaces are sonicated and rinsed clean promptly after polishing. For the acid-etching studies, the tooth was etched for 20 seconds using 35% phosphoric acid ($H_3PO_4$). The phosphoric acid was thoroughly rinsed with distilled water and the specimen lightly sonicated. When the specimen was not used, it was stored in phosphate buffered saline solution with 0.002% sodium azide, thus keeping it constantly hydrated.

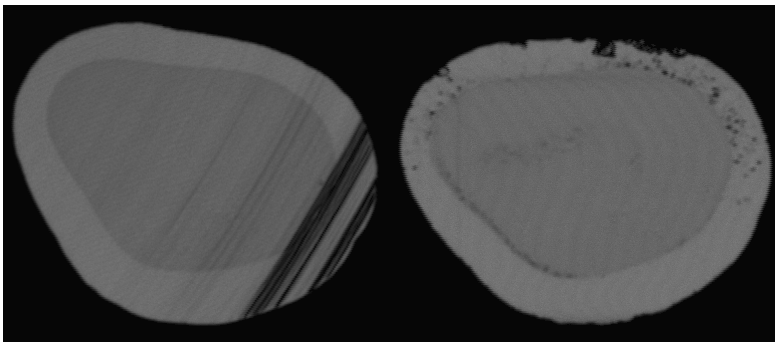

(a) (b)

Figure 3.15 SAM images (a) before and (b) after microtoming of dentin specimen

## 3.8 Measurement Protocols

### 3.8.1 Acquisition protocol

In order to compare between the pre and post-acid etched states of the specimen, we developed the following acquisition protocol. The acquisition was completed in 2 phases

*Phase 1 - Pre-acid etching phase*

The specimen, before acid-etching, was mounted on the specimen holder described in 3.3.1 and imaged in SAM with transducer 1 (30 MHz objective). The vertices A, B and C were selected and 64 locations of interest were identified as shown in Fig 3.16. At each of the 64 locations, 32 A-Scans were acquired. Care was taken such the acoustic field was focused on all the selected locations. The global coordinates of these 64 locations were input into an in-house MATLAB software to find their local coordinates as described in 3.3.2. Transducer 1 was then replaced by transducer 2 (110 MHz objective), and a C-scan image acquired. Subsequently, vertices A, B

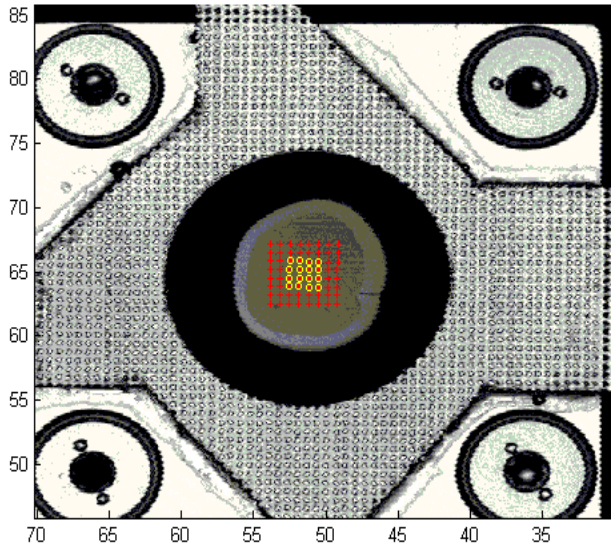


Figure 3.16 Measurement locations (units in mm)

and C were identified and their new global coordinates were input in our software to perform the transformation in Eqn 3.19 and find the locations of the 64 points of interest. This step was necessary because we could not assume that transducer 2 was centered exactly over the same location. Out of the 64 locations, a subset of 16 locations was selected and 32-A-Scans were acquired over each of these locations.

*Phase 2 - Post acid-etching*

At completion of phase 1 the specimen, always rigidly attached to the specimen holder, was removed from SAM and acid-etched as described in 3.7. After etching, the specimen was placed again in SAM and the same procedure as phase 1 was followed.

### 3.8.2 Data processing

Following the data acquisition, the 32 A-Scans acquired at each location were averaged, gated and Fourier transformed. The amplification setting for the A-Scans acquired transducer 1 was 6 dB whereas for transducer 2 the amplification setting was set to 24 dB. The calibration curves corresponding to those gain settings were retrieved and using Eqn. 3.19, the measured Fourier amplitudes were converted to reflection coefficients over the useful frequency band of each transducer.

## 3.9 Results from SAM Measurements of Etched Dentin

We begin by presenting qualitative SAM results of the effect of acid etching on the dentin surface. The C-Scans for the pre and post-acid etching states for both transducers are compared in Fig 3.17. It is observed that before acid-etching, the dentin surface is fairly homogeneous in terms of grayscale values. However, after acid etching many differences may be observed. The etching process has clearly changed the reflectance of the substrate in a location dependent manner, where different regions appear to have varying grayscale values. However, the C-Scan images tell only part of the story. Representative A-scans, acquired with transducer 1 before and after etching, are compared in Fig 3.18. We

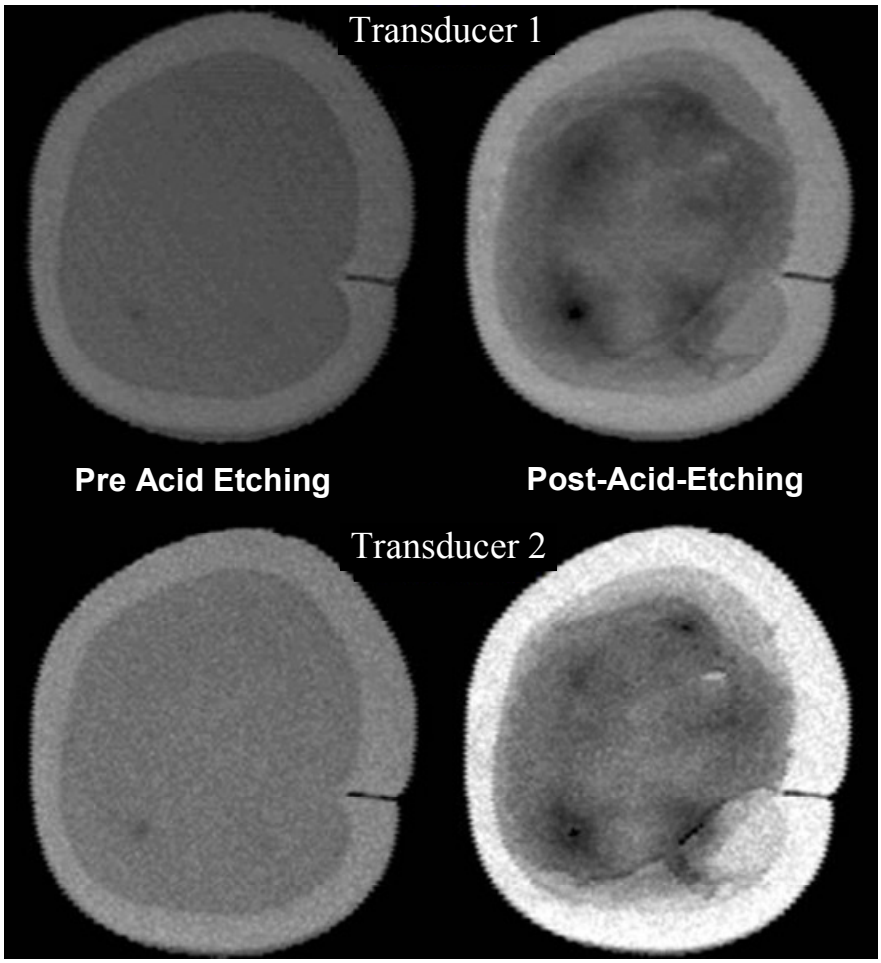


Figure 3.17 C-Scan images of before dentin substrate before (left) and after (right) acid etched dentin for the transducer 1 (top) and transducer 2 (bottom)

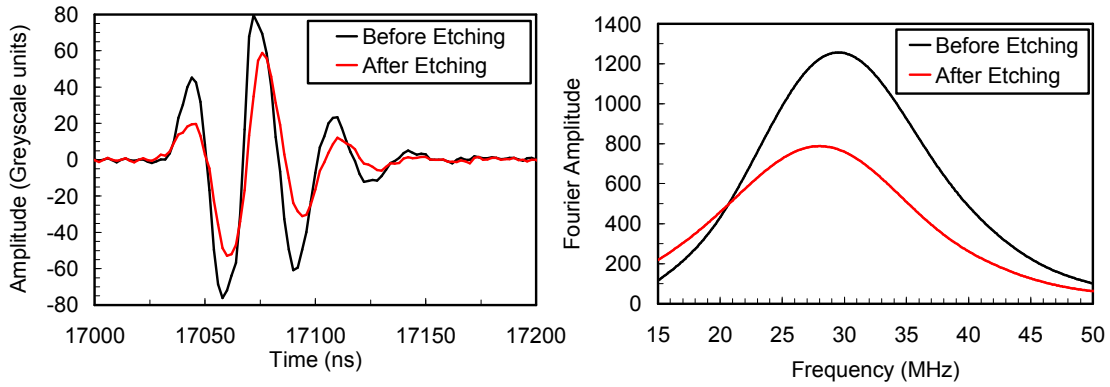


(a) (b)

Figure 3.18 Representative A-Scans (a) and their Fourier amplitude spectra (b) for transducer 1 before and after acid etching of the dentin substrate

observe that the signal amplitude after acid-etching is lower than before acid etching at the same location. To further draw attention to the differences between locations within the dentin before and after acid-etching, we plot the Fourier amplitude spectra of the subset of the sixteen locations where we have obtained waveforms from both transducers as shown in Figs 3.19-3.22. The Fourier amplitude spectra from transducer 1, before etching show minor differences at all sixteen locations. After etching however, we observe a general reduction in the overall amplitude that differs depending on the location. Additionally, a downshift of the peak frequency was observed and the location of the peak frequency was dependent on location. For transducer 2, the results revealed remarkable differences. While before etching the Fourier amplitudes were almost identical at all locations, after etching each location showed a completely different frequency behavior. Although, a reduction of the Fourier amplitudes was consistently observed, the frequency shift behavior differs between locations. For example, in location 1, the peak frequency is up-shifted while locations 5 and 8 exhibit a plateau over a large range of frequencies (35-60 MHz) and the other locations show downshifts of the peak frequency.

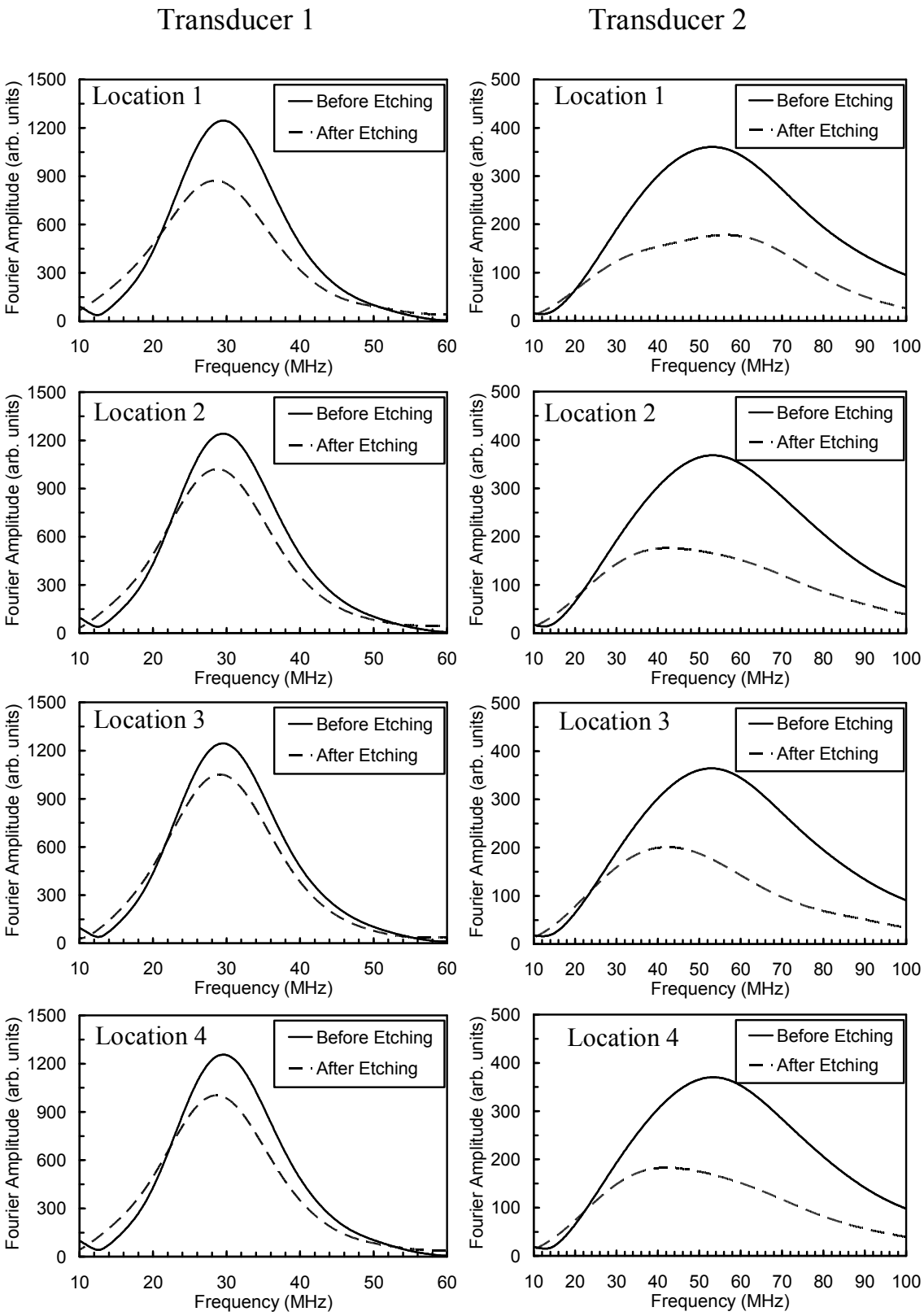


Figure 3.19 Fourier amplitude spectra for locations 1-4

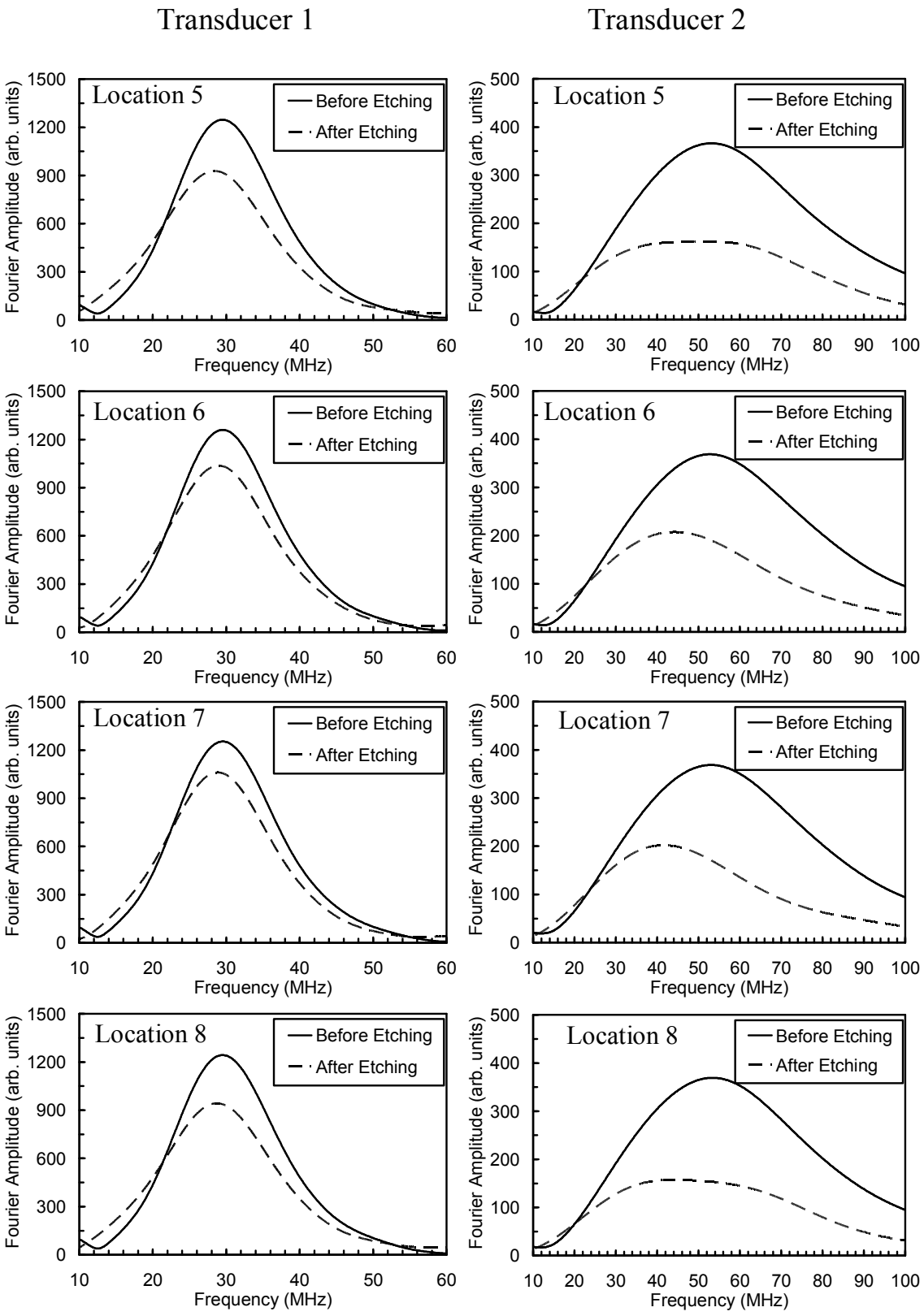


Figure 3.20 Fourier amplitude for locations 5-8

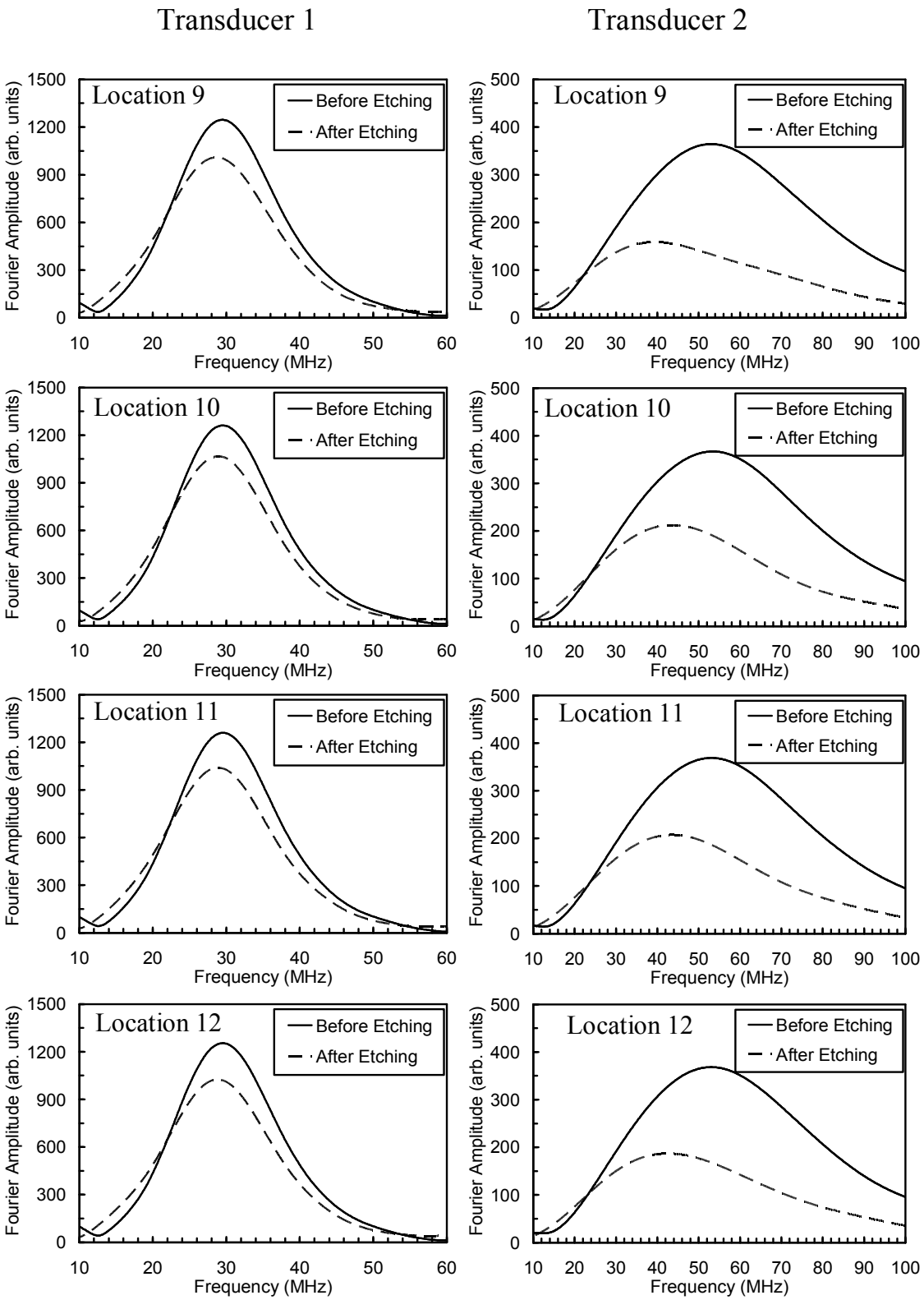


Figure 3.21 Fourier amplitude spectra for locations 9-12

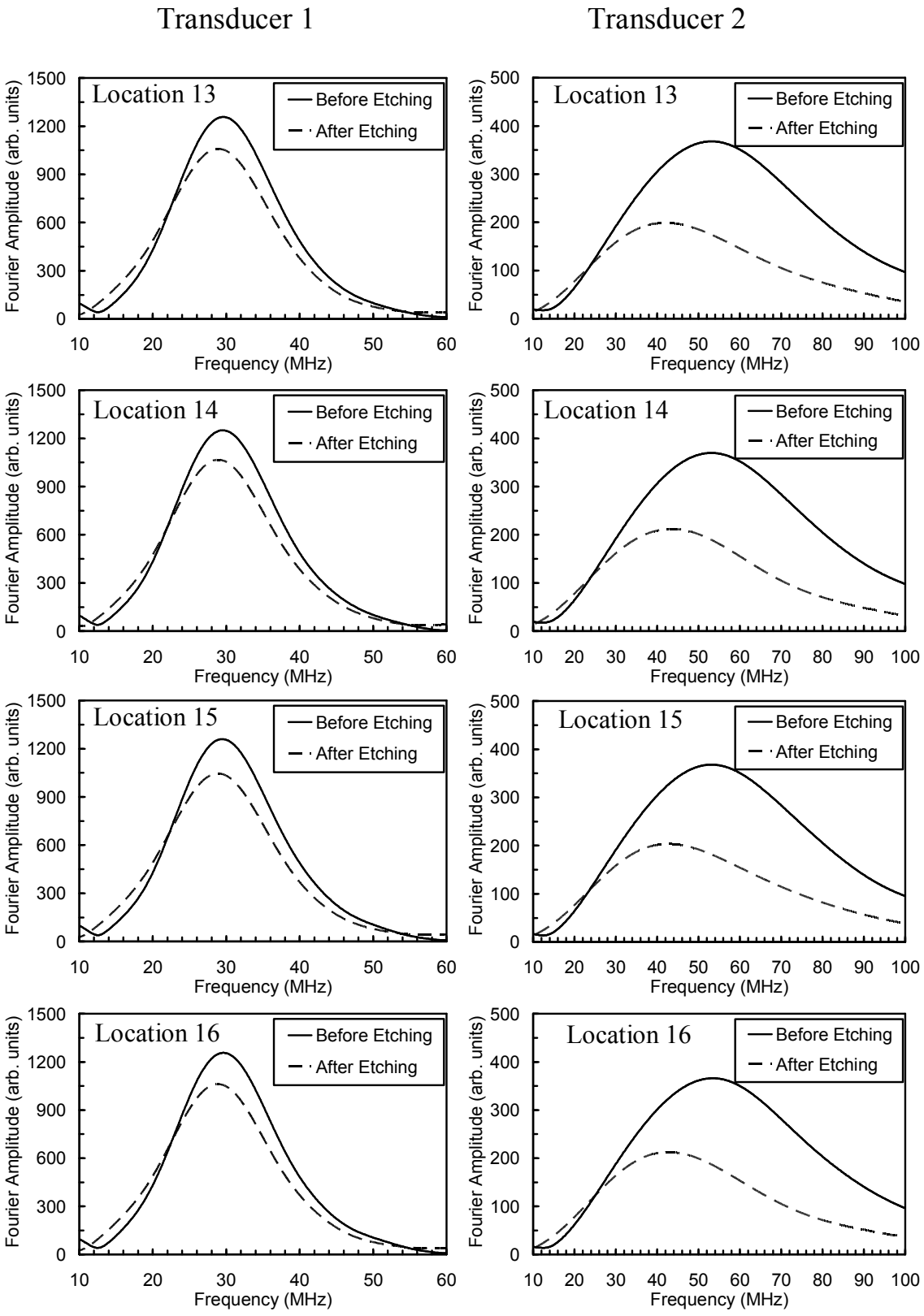


Figure 3.22 Fourier amplitude spectra for locations 13-16

For quantitative comparison, we obtained the amplitude of the reflection coefficients for the subset of the sixteen locations. Since the useful band-widths of each transducer overlapped, the reflection coefficients for all sixteen locations were plotted as a function of frequency for both transducers on the same graph as shown in Fig 3.23. As a result, reflection coefficients over a frequency ranging from 25 MHz to 70 MHz were obtained. Fig 3.23 shows that all the locations after etching are different in terms of their reflectance. For example, at a frequency of approximately 25 MHz, the reflection coefficient ranges between 0.49 and 0.65. This is definitely a significant difference especially since the measurement error in the mean reflection coefficient is approximately 0.01 as derived in section 3.2.7. Similar ranges of the reflection coefficient amplitude are observed over all the frequencies of the combined result. Interestingly, in the range between 40 and 70 MHz, several locations show a non-monotonic behavior in the amplitude of the reflection coefficient.

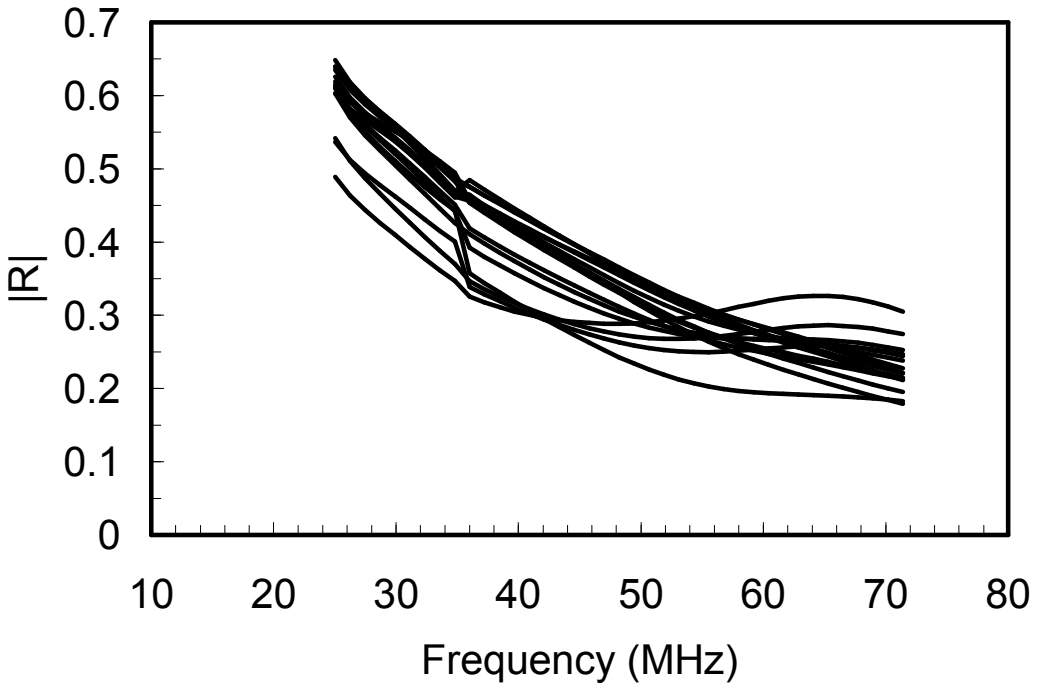


Figure 3.23 Reflection coefficient amplitude for the subset of 16 locations

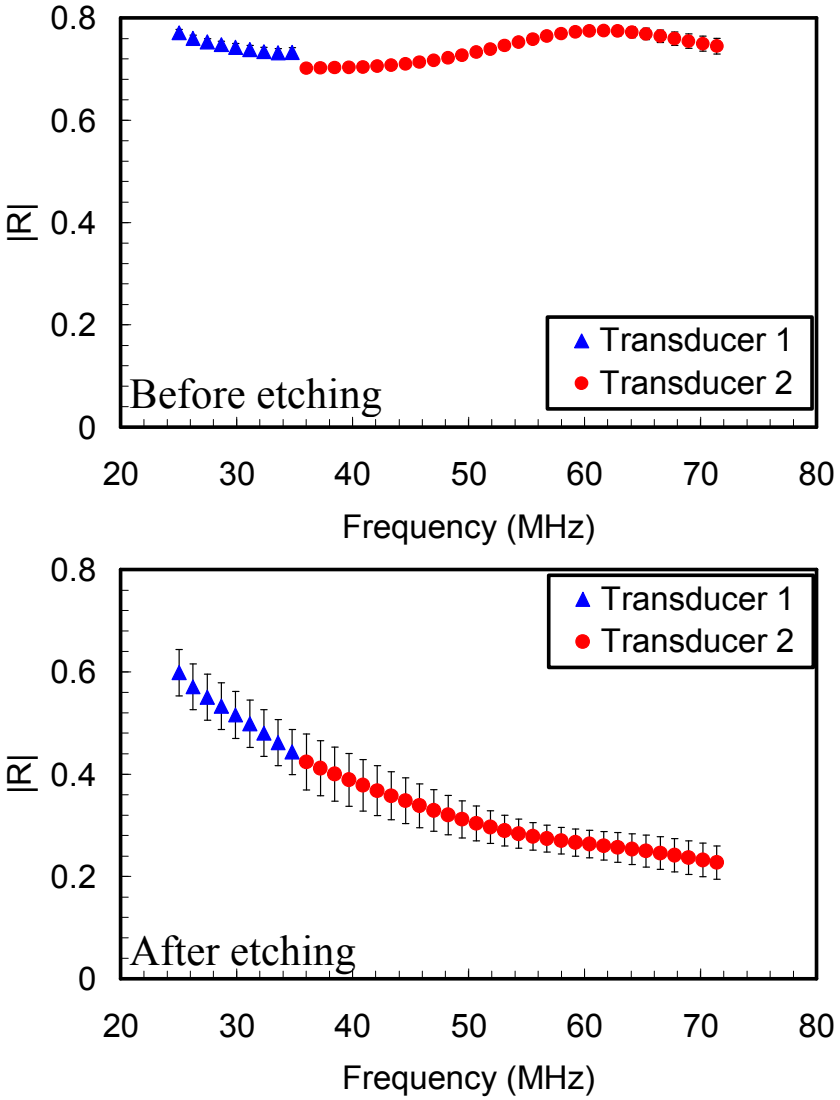


Figure 3.24 Average reflection coefficients as functions of frequency before etching (top) and after etching (bottom) for the subset of 16 locations

In Fig 3.24, we plot the average of the result shown in Fig 3.23. Each data point, corresponding represents the spatial average of the 16 locations and the error bars shows their spatial standard deviations. The average reflection coefficients confirm our previous observations. Before etching, over the frequency band between 20-70 MHz the reflection

coefficient varies slightly between 0.7 and 0.8. The standard deviation at each frequency is less than 0.01. However after etching, the average reflection coefficient showed a gradual reduction and ranged between 0.6 and 0.2. At the same time, the spatial standard deviation increased to approximately 0.04 which confirms the location dependent reflectance.

It is noteworthy that the average behavior can be very misleading, since it obscures the phenomena that are location specific. If each location is examined independently, we find that the reflection behavior suffers a frequency dependent attenuation of wavefield induced by the acid etching process. Since we know that acid etching results in a near-surface graded-layer, we utilize the theoretical approach developed in Chapter 2 in order to explain the phenomena observed.

## 3.10 Theoretical Prediction of Reflection Coefficients

For each transducer, the theoretical angular spectra of the incident wave-field were computed using the methodology presented in 2.2.1 for a range of frequencies within each transducer's bandwidth (25-38 MHz for transducer 1 and 35-74 MHz for transducer 2). For the same range of frequencies, the reflectance function of the substrate was computed by the methodology presented in 2.2.4. Subsequently, the incident angular spectra are multiplied by the reflectance functions at the corresponding frequencies and propagated back to the aperture plane through a phase factor. At the aperture plane, an inverse two dimensional Fourier transform of the reflected angular spectrum is performed, resulting to the reflected pressure distribution at that plane. The pressure distribution is then integrated over the aperture domain to yield the average reflected pressure at the aperture plane $\overline{p}_{rec}(\omega)$. Since the average reflected pressure has been evaluated for a range of frequencies, we regard it as a spectrum.

From Eq. 2.2, we may define the temporal Fourier transform V(ω) of the average reflected pressure as:

$$V(\omega) = v(\omega)\overline{p}_{rec}(\omega) \tag{3.20}$$

Since the frequency spectrum of the normal velocity v(ω) is not known *a priori*, it is back-computed by using the experimentally measured Fourier amplitude spectrum for tungsten, $V_W(\omega)$ at the gain setting where the effects of system electronics are negligible (-10 dB for transducer 1 and 10 dB for transducer 2) as:

$$v(\omega) = \frac{V_W(\omega)}{\int_{-a}^{a}\int_{-a}^{a} p(\omega, x, y, 0)dxdy} \tag{3.21}$$

where the quantity $\int_{-a}^{a}\int_{-a}^{a} p(\omega, x, y, 0)dxdy$ is the spectrum of the average pressure at the aperture plane , computed using Coulouvrat's method in section 2.2.2. The predicted reflected frequency spectrum is then written as:

$$V(\omega) = \frac{V_W(\omega)\int_{-a}^{a}\int_{-a}^{a}\left[\int_{-\infty}^{\infty}\int_{-\infty}^{\infty} P(k_x, k_y, z_0)R(k_x, k_y)e^{i(k_x x + k_y x)}e^{ik_z z_0}dk_x dk_y\right]dxdy}{\int_{-a}^{a}\int_{-a}^{a} p(\omega, x, y, 0)dxdy} \tag{3.22}$$

In addition, the Fourier amplitude V(w) may also be written as:

$$|V(\omega)| = |V_W(\omega)||R_{eff}(\omega)| \tag{3.23}$$

where we have defined $R_{eff}$ as the effective reflection coefficient of the system given by

$$R_{eff} = \frac{\int_{-a}^{a}\int_{-a}^{a}\left[\int_{-\infty}^{\infty}\int_{-\infty}^{\infty} P(k_x, k_y, z_0)R(k_x, k_y)e^{i(k_x x + k_y x)}e^{ik_z z_0}dk_x dk_y\right]dxdy}{\int_{-a}^{a}\int_{-a}^{a} p(\omega, x, y, 0)dxdy} \tag{3.24}$$

To demonstrate the methodology for predicting the experimental reflection coefficient amplitudes shown in Fig 3.23, we considered locations 1, 5 and 11, which are representative examples of frequency dependent behavior observed from the etched dentin substrate. The ultrasonic fields and angular spectra were computed using the geometric parameters in section 2.2.3, which are pertinent to transducer 1 and 2 used in our experiment. For computing the reflectance function, a graded surface layer of etched dentin of depth H, over a homogeneous dentin half-space was considered. Furthermore, the etched layer transitions with no discontinuity to the underlying dentin half-space C so that $\rho^h = \rho^s$, $C_{11}^h = C_{11}^s$ and $C_{44}^h = C_{44}^s$. The material density of the dentin substrate was taken as $\rho^s$=2.1 Mg/m$^3$, while the elastic moduli are taken as, $C_{11}^s$=38.6 GPa, and $C_{44}^s$=8.03 GPa. For the water half-space, the bulk modulus, $C_{11}^f$ was considered as 2.22 GPa, and density $\rho^f$ = 1.0 Mg/m$^3$. The material gradation for the graded surface layer was considered as linear and the parameters used for predicting the experimental frequency spectra and reflection coefficients locations 1, 5 and 11 are given in Table 2.

Table 3-2 Properties of etched layer for the three locations used for prediction

| **Location** | **$C_{11}^0$ (GPa)** | **$C_{44}^0$ (GPa)** | **$\rho^0$ (Mg/m$^3$)** | **H ($\mu$m)** |
|---|---|---|---|---|
| **1** | 6.44 | 0.59 | 1.0 | 36 |
| **5** | 5.91 | 0.54 | 1.0 | 32 |
| **11** | 3.31 | 0.30 | 1.0 | 27 |

The predicted angular spectra for location 1 are shown in Fig 3.24 for transducers 1 and 2 at their edge and central frequencies. These figures demonstrate the process of obtaining the reflected angular spectrum by multiplication of the incident angular spectrum with the reflectance function. We highlight the fact that the incident angular spectra are different for each frequency.

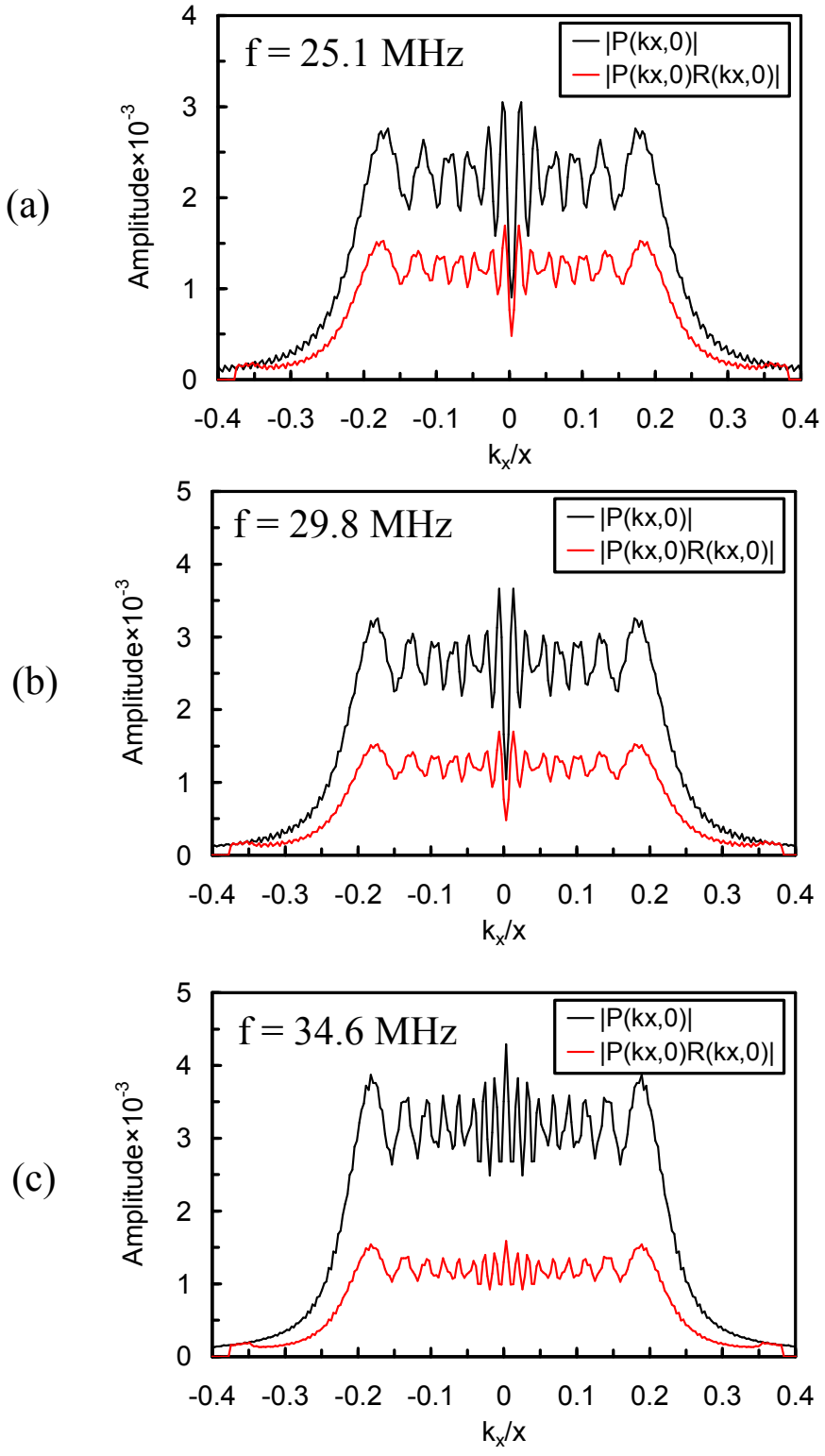


Figure 3.25 Incident and reflected angular spectra for transducer 1 at location 1 at (a) 25.1 MHz, (b) 29.8 MHz and (c) 34.6 MHz

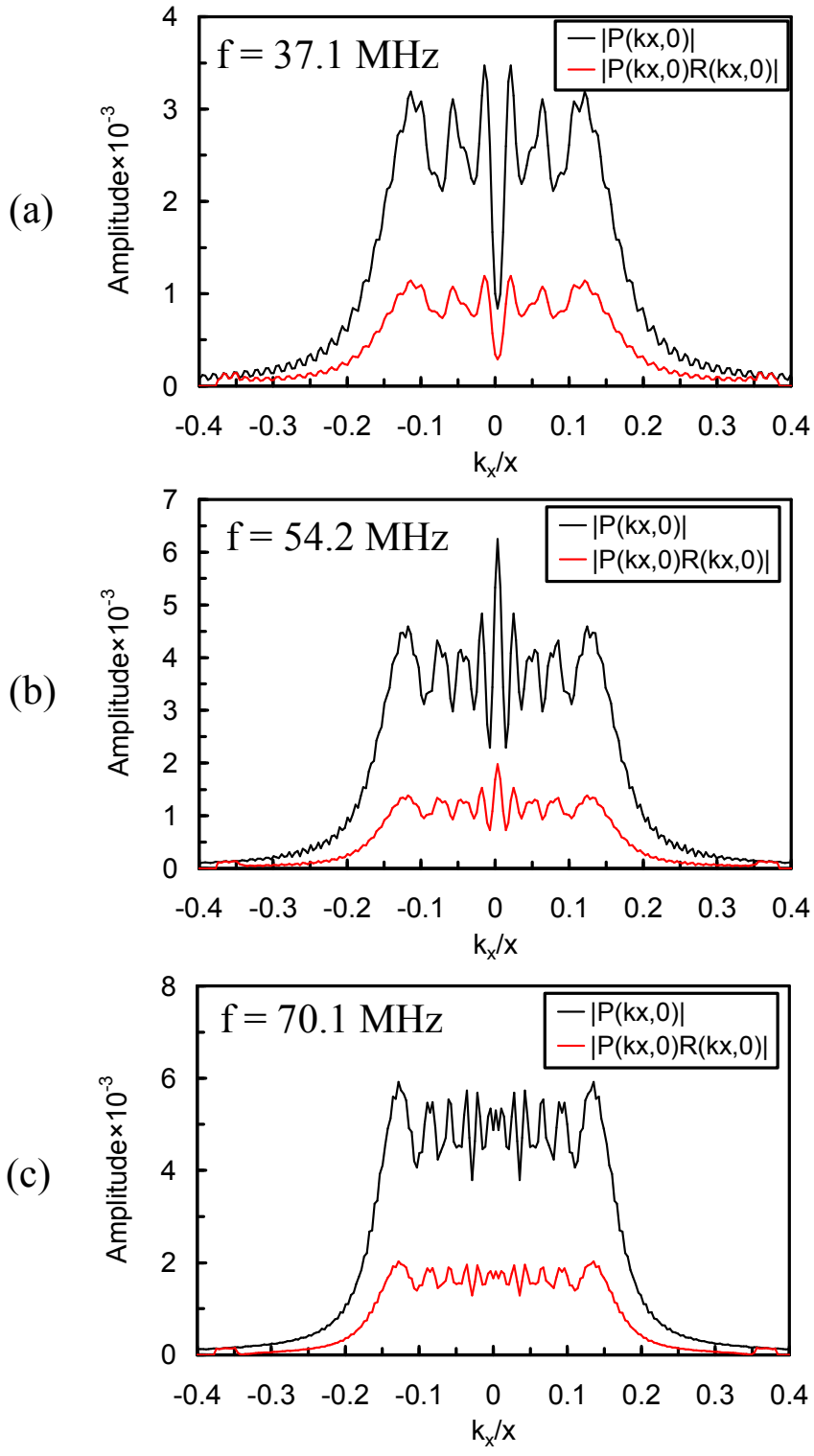


Figure 3.26 Incident and reflected angular spectra for transducer 2 at location 1 at (a) 37.1 MHz, (b) 54.2 MHz and (c) 70.1 MHz

Additionally, Fig 3.25 and Fig 3.26 show that the effect of angles larger than ~14° for transducer 1 and ~10° for transducer 2 have a negligible contribution to the reflected spectrum. In Fig 3.27 we plot the reflected angular spectra for the three locations 1, 5 and 11 at the central frequencies of transducers 1 and 2.

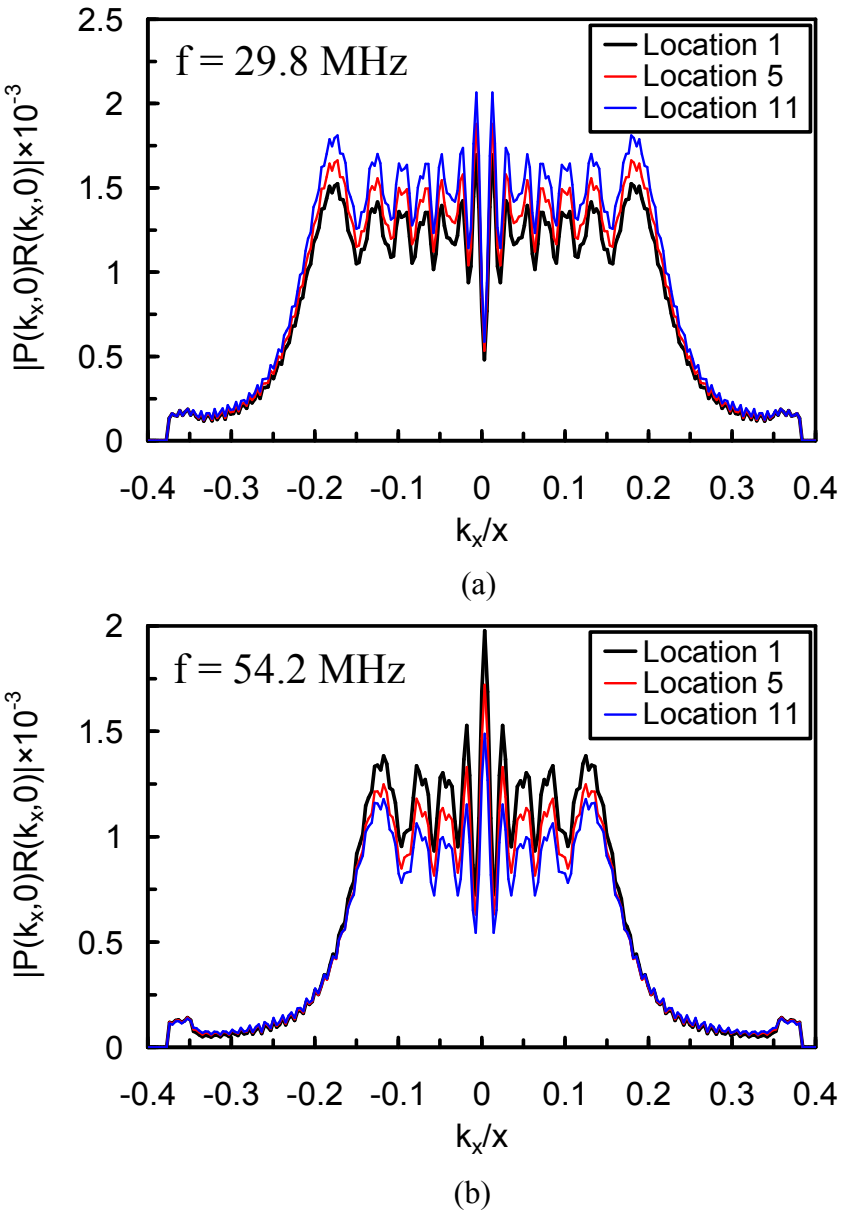


Figure 3.27 Reflected angular spectra for locations 1,5 and 11 for (a) transducer 1 at f=29.8 MHz and (b) transducer 2 at f=54.2 MHz

Finally, the predicted effective reflection coefficients at the three locations are plotted in Figs 3.28-3.30. We observe that for each of the three locations, the theoretical model is able to capture the main attenuation effects with a reasonable set of parameters assumed for the acid etched layer. In order to establish an appropriate set of parameters for the theoretical model that can match the experimental reflection coefficients and spectra ideally the inverse problem needs to be solved formally through optimization. However, since this was not the scope of this dissertation, the model parameters were obtained by trial and error.

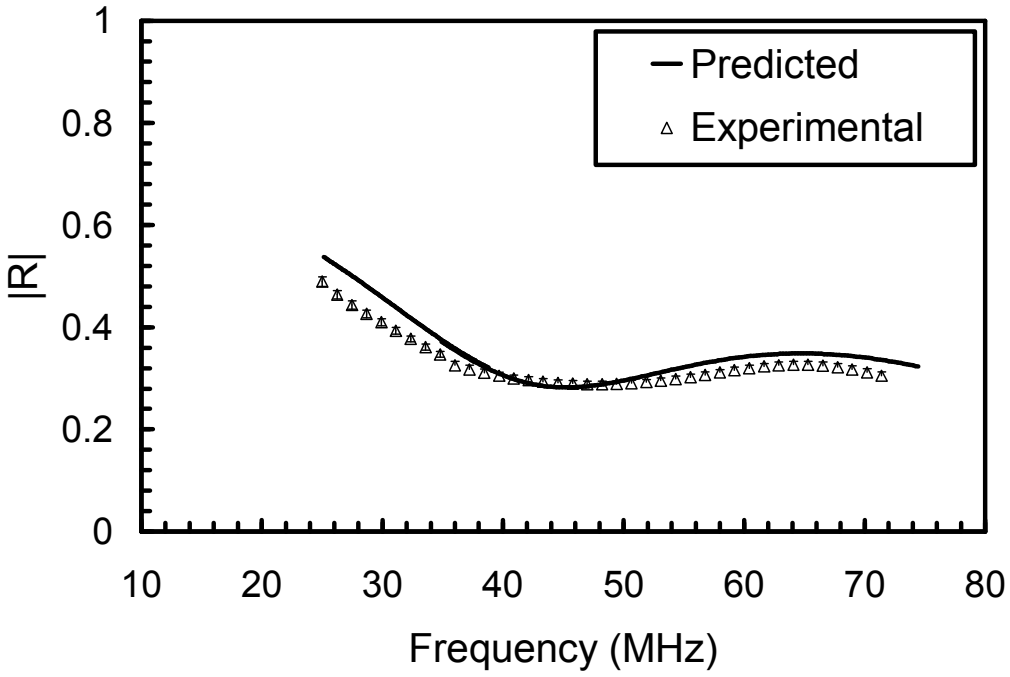


Figure 3.28 Comparison between theoretical and experimental reflection coefficient amplitude for location 1

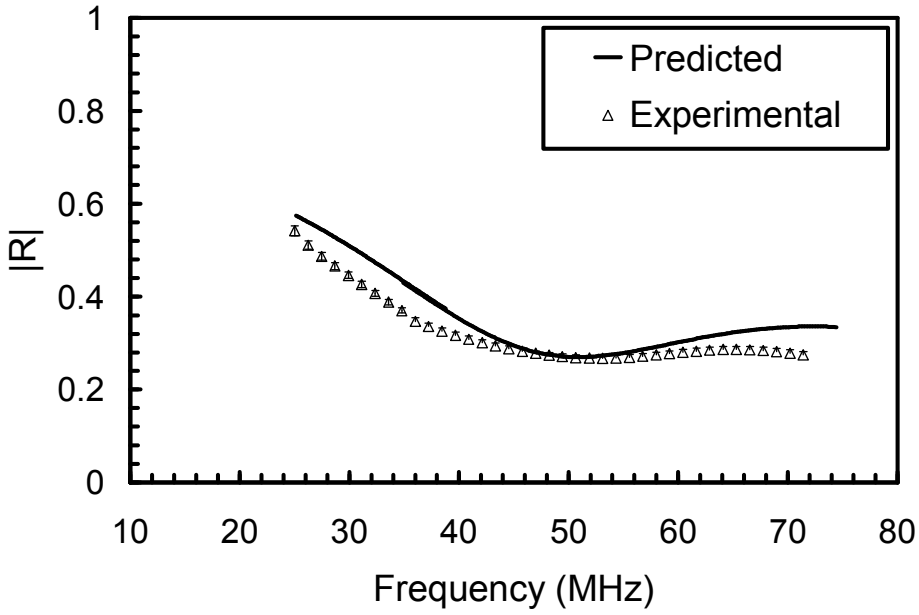


Figure 3.29 Comparison between theoretical and experimental reflection coefficient amplitude for location 5

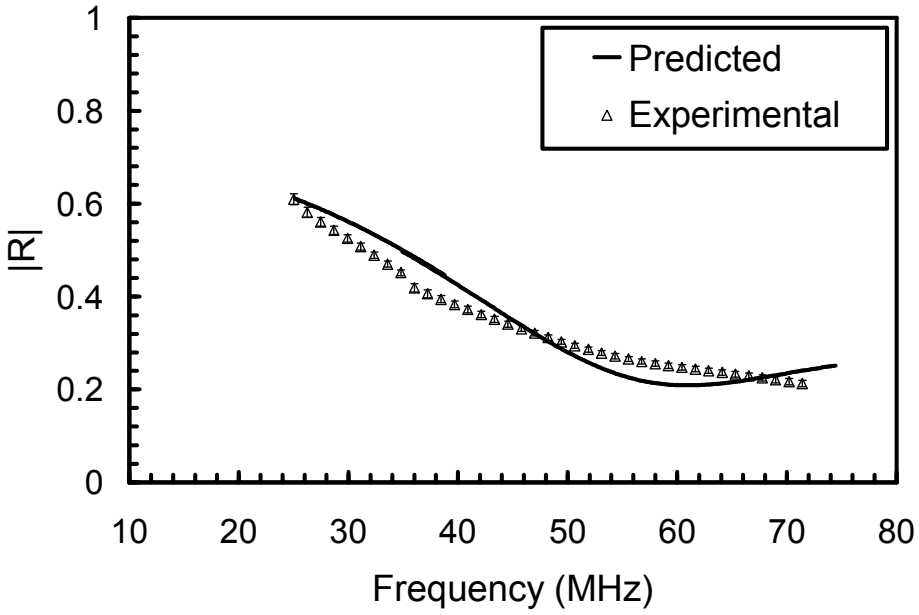


Figure 3.30 Comparison between theoretical and experimental reflection coefficient amplitude for location 5

Nevertheless, the predicted results from our theoretical model provide valuable insights to the effects of etching on the dentin substrate. The close match between the model prediction and experimental data suggests that acid etching induces a near-surface layer of graded material properties. The elastic property variation predicted by the model indicates that the topmost part of this layer is very soft (3-6 GPa) and becomes stiffer as it transitions to the dentin substrate. The density variation in this layer should also follow a similar pattern. Furthermore, the etching depth is likely not uniform as the best-fit graded layer thickness for the three locations were 36, 32 and 27 microns. There are clinical implications of this finding as the dental literature suggests that only the first few microns of the etched dentin surface are eventually infiltrated by the dentin adhesive. Thus, the dentin-adhesive bonding is a near-surface interaction of the adhesive and the etched adherent, which is mostly de-mineralized dentin. Our results would then suggest that a soft graded layer is present underneath the composite restoration. The contribution of such a layer to the eventual failure of the composite restoration remains unknown and deserves to be studied in the future. Finally, we note that the theoretical methodology presented is necessary in order to interpret results from reflection acoustic microscopy of materials with near-surface graded layer.

# 4.0 SUMMARY AND CONCLUSIONS

The work accomplished in this dissertation is summarized as follows:

1. *Modeling of focused ultrasonic field* – An extensive literature review of methods for calculation acoustic field from concave lenses was performed. Based upon this literature review, a method proposed by Coulouvrat (1993) for computing the field produced by a concave lenses using Legendre polynomial expansions and boundary collocation while satisfying the exact radiation condition at infinity was adopted. The above method was implemented for numerical calculations in a computer program. A normalization procedure was developed for accurate solution of the matrix system resulting by this method. To that end, the system matrix was recast in terms of ratios and products of spherical Bessel and Hankel functions. An algorithm based upon continued fraction expansions was developed for computing these ratios and products in an efficient manner.
2. *Modeling of interaction of the ultrasonic field with a complex substrate* – A methodology was developed for computing the angular spectrum of the pressure field generated by the lens. This methodology was used to compute the angular spectrum at the plane of the substrate surface, such that the incident field can be expressed in terms of plane waves with different directions of propagation. The incident field obtained from the angular spectrum was then used as input to the wave propagation model for the substrate. In addition, a multilayered stiffness method was implemented in a computer program to model the wave propagation in a substrate with a layer of graded material properties. An iterative criterion for solution convergence was established to reduce the effect of layer discretization.

3. *Parametric studies to assess model capabilities* – The above models were applied to investigate the interaction of focused acoustics fields with substrates possessing near-surface graded layer. The effect of material mechanical and physical property gradation and layer thickness on the frequency dependence of the reflection coefficients was studied by parametric variation.
4. *Calibration of SAM* – A commercial acoustic microscope was utilized in this work to characterize a dentin substrate subjected to acid etching. For accurate quantification using the commercial SAM, a calibration methodology was developed to determine substrate reflection coefficients that compensates for the nonlinearities in the amplification system. A suite of calibration materials was utilized to develop calibration curves for a variety of instrument amplification setting. Furthermore, an error analysis was performed to define the measurement errors with this instrument.
5. *SAM measurement protocol* – A homotopic measurement protocol was developed in order to acquire the acoustic microscopy data from the same locations pre and post-etching of the dentin sample. Consequently, a prototype sample holder was developed for performing homotopic measurements. In addition, protocols for etched dentin specimen preparation and data acquisition were developed and utilized to obtain A-scan data from several locations on pre- and post-etched dentin sample. Customized software was developed to aid data acquisition and perform data post processing to obtain time signal FFT and reflection coefficients in the frequency domain.
6. *Comparison of measured results with theoretical prediction* – The theoretical model developed in this dissertation was used to predict the frequency dependent reflection coefficients of a substrate with near-surface graded layers. The predicted results were used to explain the frequency dependent attenuation effects exhibited by the measured data.

A synopsis of the main findings is as follows:

1. *Ultrasonic field modeling* – The method for computing the ultrasonic field adopted in this dissertation is rigorous and elegant. It does not suffer from any approximations stemming from the geometry of the ultrasonic objective and it is expected to have a greater range of applicability in modeling more complicated acoustic objective geometries. Theoretical computation of the pressure fields at focal regions provides direct information about the area of the specimen that interacts with the ultrasonic field. For multiple frequency SAM measurements on complex substrates, such as near-surface graded layers considered in this work, the received signal contains a richness of information from ultrasonic field interactions from multiple scales. In order to understand the material characteristics, it is extremely important to have an accurate representation and understanding of the "probe" with which we are interrogating the material.
2. *Modeling of interaction of the ultrasonic field with a complex substrate* – An important aspect of SAM modeling is the mix of two coordinate descriptions. While the pressure field that is generated from the spherical lens is best described using spherical coordinates, the ultrasonic field interacting with the planar specimen surface is described in Cartesian coordinates. The angular spectrum approach provides an excellent means to interface the solutions of acoustic and elastic wave propagation from spherical to Cartesian geometries. Modeling a near-surface layer with continuously graded material properties by a discretely layered system was successful however it requires a convergence criterion in order to minimize the effect of discretization since the number of layers required for accurate approximation depends both on the angle of incidence and the temporal frequency considered, as well as the steepness of the gradation profiles.

3. *Parametric studies* – Parametric studies show that near-surface graded layers exhibit profound frequency dependence of their reflectance functions. This behavior is characteristic to the material property gradation profiles as well as the depth of the property gradations and it is detectable even at near-vertical incidence angles.
4. *Calibration of SAM* – It is important in quantitative SAM measurements that the linearity of the amplification system is assessed. Near saturation effects at high amplification settings hamper the accuracy of the reflection coefficient measurement. Additionally, excessive nonlinearity of the amplification electronics generates higher order harmonics that contaminate the amplitude spectra and mask any frequency dependent material response. In such cases, the calibration methodology developed in this work is able to compensate for the effects of the amplification electronics. Performing error analysis on the measured reflection coefficients based on signal to noise ratio is essential for assessing the precision of the reflection coefficient measurements.
5. *SAM measurement protocol* – Homotopic measurements are essential in SAM. The measurements carried out in SAM are high resolution and for meaningful comparison between two different states of the same substrate, as the example of acid-etching of dentin these measurements have to be carried out at the same location. Additionally by sequencing the measurement protocol, we are able to have knowledge of the initial condition of the material.
6. Comparison of experimental data with theoretical prediction – The theoretical model is able to capture the frequency dependent effects observed by the experiment. It thus provides valuable insights about the effects of acid etching on the dentin substrate. The theoretical model suggests that the etching process creates a graded surface layer of non-uniform depth.

In addition, the close fit between the experimental results and the model, suggest that the dimensions of the near-surface layer induced by acid-etching on dentin and the frequency range used are such that the frequency dependence of the reflection coefficient is prominent.

Possible future work to advance the methods developed in this dissertation are as follows:

1. *Parameter identification and inverse problem implementation* – The method developed in this dissertation focused upon the computation of the reflection coefficient for a substrate whose parameters are pre-assigned, i.e. the method solves the forward problem. In order to establish an appropriate set of parameters for an unknown substrate, the inverse problem needs to be solved formally through optimization. Future development along these lines will eliminate the need for trial and error procedure for parameter identification.
2. *Further parametric study to evaluate the effects of non-linear property gradations* – In this dissertation, a linear variation of material properties with depth was assessed. Near-surface graded layers could have various grading profiles depending upon their genesis. How non-linear profiles affect the attenuation of the reflected fields needs further investigation.
3. *Further develop the theoretical model* – The current theoretical model addresses axi-symmetric problems and substrates with vertical heterogeneity. Additionally, uniform discretization of the layer profile was performed to approximate the continuous vertical inhomogeneity. Further development of the model is desired to address: (i) non-axi-symmetric problems, (ii) lateral heterogeneities, (iii) the coupling medium attenuation (iv) non-uniform discretization of the vertical inhomogeneity.

# 5.0 REFERENCES


[1] Achenbach JD Wave propagation in elastic solids. Amsterdam: North Holland 1973

[2] Aki K and Richards PG Quantitative seismology. San Francisco: Freeman 1980

[3] Angker L, Nockolds C, Swain MV, Kilpatrick N Correlating the mechanical properties to the mineral content of carious dentine--a comparative study using an ultra-micro indentation system (UMIS) and SEM-BSE signals. Arch Oral Biol 2004;49(5):369-78

[4] Ardebili VS A new angular spectrum approach for modelling the acoustic microscope response with high attenuation coupling fluids. IEEE Ultrasonics Symposium 1995;2:873-76

[5] Arfken GB and Weber HJ Mathematical methods for physicists. Boston: Elsevier 2005

[6] Arsenault AL A comparative electron microscopic study of apatite crystals in collagen fibrils of rat bone, dentin and calcified turkey leg tendons. Bone Miner 1989;6(2):65-77

[7] Atalar A An angular-spectrum approach to contrast in reflection acoustic microscopy. J Appl Phys 1978;49(10):5130-39

[8] Babenko VA, Astafyeva LG, Kuzmin VN Electromagnetic scattering in disperse media: Inhomogeneous anisotropic particles. New York: Springer-Praxis 2003

[9] Baker BB and Copson ET The mathematical theory of Huygens' principle. Chelsea: New York 1987

[10] Balooch M, Wu-Magidi I-C, Balazs A, Lundkvist AS, Marshall SJ, Marshall GW, Siekhaus WJ, Kinney JH Viscoelastic properties of demineralized human dentin measured in water with atomic force microscope (AFM)-based indentation. J Biomed Mater Res 1998;40:539-44

[11] Barnett AR The calculation of spherical Bessel functions and Coulomb functions. In: Bartschat K, editor. Computational Atomic Physics: Springer 1996. Chapter 9

[12] Bell WW Special functions for scientists and engineers London: Van Nostrand 1968

[13] Bembey AK, Oyen ML, Ko C-C, Bushby AJ, Boyde A Elastic modulus and mineral density of dentine and enamel in natural caries lesions. In: Fratzl P, Landis WJ, Wang R, Silver FH, editors. Structure and Mechanical Behavior of Biological Materials. Warrendale: MRS 2005. p 125-130

[14] Berezovski A, Engelbrecht J and Maugin GA Numerical simulation of two-dimensional wave propagation in functionally graded materials. Eur J Mech A-Solid 2003;22(2):257-65

[15] Bertoni HL Ray optical evaluation of V(z) in the reflection acoustic microscope. IEEE Trans Ultrason Ferroelect Freq Contr 1984;(31):105-16

[16] Bird MJ, French EL, Woodside MR, Morrison MI, Hodge HC. Chemical analyses of deciduous enamel and dentin. J Dent Res 1940;19(4):413-23

[17] Born M and Wolf E Principles of optics Cambridge: Cambridge 1999

[18] Bourbié T and Nur A Effects of attenuation on reflections: Experimental test J Geophys Res 1984;89(B7):6197-202

[19] Briggs GAD Acoustic Microscopy Oxford: Clarendon 1992

[20] Brekhovskikh LM Waves in layered media Academic: New York 1960

[21] Buonocore MG A simple method of increasing the adhesion of acrylic filling materials to enamel surfaces. J Dent Res 1955; 34:849-53

[22] Butler WT Dentin extracellular matrix and dentinogenesis. Oper Dent 1992; Suppl 5:18-23

[23] Canumalla S Resolution of broadband transducers in acoustic microscopy of encapsulated ICs: Transducer selection. IEEE Trans Compon Pack Technol 1999;22(4):582-92

[24] Cathignol D and Sapozhnikov OA On the application of the Rayleigh integral to the calculation of the field of a concave focusing radiator. Acoust Phys 1999;45(6):735-42

[25] Chou C-H Kino GS The evaluation of V(z) in a type II reflection microscope IEEE Trans Ultrason Ferroelect Freq Contr 1987;34(3):341-45

[26] Corbató FJ and Uretsky JL Generation of spherical Bessel functions in digital computers. J ACM 1959;6(3):366-75

[27] Coulouvrat F Continuous field radiated by a geometrically focused transducer: Numerical investigation and comparison with an approximate model. J Acoust Soc Am 1993;94(3):1663-75

[28] Del Grosso VA, and Mader CW Speed of sound in pure water J Acoust Soc Am 1972;52(5): 1442-6

[29] Dickinson ME, Wolf KV, Mann AB Nanomechanical and chemical characterization of incipient in vitro carious lesions in human dental enamel. Arch Oral Biol 2007;52(8):753-60

[30] Dunkin JW Computations of modal solutions in layered elastic media at high frequencies. Bull Seism Soc Am 1965;55:335-58

[31] Eick JD Smear layer-materials surface. Proc Finn Dent Soc 1992;88(Suppl 1):225-242

[32] Ferguson VL, Bushby AJ, Boyde A Nanomechanical properties and mineral concentration in articular calcified cartilage and subchondral bone. J Anat 2003;203(2):191-202

[33] Ferguson VL, Boyde A, Bushby AJ Elastic modulus of dental enamel: effect of enamel prism orientation and mineral content. MRS: Warrendale 2004

[34] Feng F, Mal A, Kabo M, Wang JC, Bar-Cohen Y The mechanical and thermal effects of focused ultrasound in a model biological material. J Acoust Soc Am 2005;117(4):2347-55

[35] Gage JP, Francis MJO, Triffitt JT. Collagen and Dental Matrices. Boston: Wright 1989

[36] Gautchi W Computational aspects of three-term recurrence relations. SIAM Rev 1967;9(1):24-82

[37] Gilbert F and Backus GE Propagator matrices in elastic wave and vibration problems. Geophysics 1966;31:326-32

[38] Goodman JW Introduction to Fourier optics NewYork:McGraw-Hill 1996

[39] Gruner JW, McConnell D, Armstrong WD. The relationship between crystal structure and chemical composition of enamel and dentin. J Biol Chem 1937;121(2):771-81

[40] Gupta HS, Schratter S, Tesch W, Roschger P, Berzlanovich A, Schoeberl T, Klaushofer K, Fratzl P Two different correlations between nanoindentation modulus and mineral content in the bone cartilage interface. J Struct BIol 2005;149(1):138-48

[41] Haïat G, Naili Grimal Q, Talmant M, Desceliers C, Soize C Influence of a gradient of material properties on ultrasonic wave propagation in cortical bone: Application to axial transmission. J Acoust Soc Am 2009:125(6):4043-52

[42] Haskell NA The dispersion of surface waves on multilayered media. Bull Seismol Am 1953;43:17-34

[43] Hirayama A, Yamada M, Miake K An electron microscopic study on dentinal tubules of human deciduous teeth. Shikwa Gakuho 1986;86(6):1021-31

[44] Hirsekorn S, Pangraz S, Weides G, Arnold W. Measurement of elastic impedance with high spatial resolution using acoustic microscopy. Appl Phys Lett 1995;67(6):745-47

[45] Hirsekorn S, Pangraz S, Weides G, Arnold W. Erratum: Measurement of elastic impedance with high spatial resolution using acoustic microscopy. Appl Phys Lett 1996;69(14):2138

[46] Ho SP, Balooch M, Marshall SJ, Marshall GW Local properties of a functionally graded interphase between cementum and dentin. J Biomed Mater Res 2004;70A:480-89

[47] Hofmann T, Heyroth F, Meihard H, Franzel W, Raum K Assessment of composition and anisotropic elastic properties of secondary osteon lamellae. J Biomech 2006;39(12):2282-94

[48] Hook JF Separation of the vector wave equation of elasticity for certain types of inhomogeneous, isotropic media J Acoust Soc Am 1961;33(3):302-13

[49] Hook JF Erratum: Separation of the vector wave equation of elasticity for certain types of inhomogeneous, isotropic media J Acoust Soc Am 1961;33(7):967

[50] Ilett C, Somekh MG, Briggs GAD Acoustic microscopy of elastic discontinuities. Proc R Soc Lond A 1984;393(1804):171-83

[51] John C. Lateral distribution of ultrasound velocity in horizontal layers of human teeth. J Acoust Soc Am 2006;119(2):1214-26

[52] Karal FC Jr. and Keller JB Elastic wave propagation in homogeneous and inhomogeneous media. J Acoust Soc Am 1959;31(6):694-705

[53] Katz JL and Meunier A Scanning acoustic microscope studies of the elastic properties of osteons and osteon lamellae. J Biomech Eng 1993;115(4B):543-41

[54] Katz JL, Bumrerraj S, Dreyfuss J, Wang Y, Spencer P. Micromechanics of the dentin/adhesive interface. J Biomed Mater Res B Appl Biomater 2001;58(4):366-71

[55] Katz JL, Spencer P, Nomura T, Wagh A, Wang Y. Micromechanical properties of demineralized dentin with and without adhesive infiltration. J Biomed Mater Res A 2003;66(1):120-28

[56] Kausel E and Roësset JM Stiffness matrices for layered soils. B Seismol Soc Am 1981;71(6) 1743-61

[57] Keller JB and Givoli D Exact non-reflecting boundary conditions. J Comput Phys 1989;82:172-92

[58] Kinney JH, Balooch M, Haupt DL, Marshall SJ, Marshall GW Mineral distribution and dimensional changes in human dentin during demineralization. J Dent Res 1995; 74(5):1179-84

[59] Kinney JH, Balooch M, Marshall GW, Marshall SJ A micromechanics model of the elastic properties of human dentine. Arch Oral Biol 1999;44(10):813-22

[60] Kinney JH, Marshall SJ, Marshall GW The mechanical properties of human dentin: a critical review and reevaluation of the dental literature. Crit Rev Oral Biol Med 2003;14(1):13-29

[61] Kinney JH, Gladden JR, Marshall GW, Marshall SJ, So JH, Maynard JD. Resonant ultrasound spectroscopy measurements of the elastic constants in human dentin. J Biomech 2004;37(4):437-41

[62] Knopoff L A matrix method for elastic wave problems. Bull Seism Soc Am 1964;54 431-38

[63] Koutsi V, Noonan RG, Horner JA, Simpson MD, Matthews WG, Pashley DH. The effect of dentin depth on the permeability and ultrastructure of primary molars. Pediatr Dent 1994;16(1):29–35

[64] Kramer IRH, McLean JW Alterations in the staining reactions of dentine resulting from a constituent of a new self-polymerizing resin. Brit Dent J 1952:92 150-3

[65] Kundu T, Mal AK, Weglein RD Calculation of the acoustic material signature of a layered solid. J Acoust Soc Am 1985;77(2):353-61

[66] Kundu T and Lee J-P Acoustic microscope lens modeling and its application in determining biological cell properties from single-and multi-layered cell models. J Acoust Soc Am 2006;120(3):1646-165

[67] Kushibiki J, Ha KL, Kato H, Chubachi N Application of acoustic microscopy to dental material characterization. IEEE Ultrasonics Symposium 1987:837-842

[68] Lee Y-C, Kim JO Achenbach JD V(z) curves of layered anisotropic materials for the line-focus acoustic microscope. J Acoust Soc Am 1993;94(2):923-30

[69] Lees S, Rollins FR. Anisotropy in hard dental tissues. J Biomech 1972;5(6):557-66.

[70] Lemons RA and Quate CF Acoustic microscope-scanning version Appl Phys Lett 1974;24(4):163-65

[71] LeFevre ML and Hodge HC Chemical analysis of tooth samples composed of enamel, dentine and cementum: II. J Dent Res 1937;16(4):279-87

[72] Lemor R, Kruger MB, Wieliczka DM, Spencer P, May T Dentin etch chemistry investigated by Raman and infrared spectroscopy. J Raman Spectrosc 2000; 31:171-76

[73] Lentz WJ Generating Bessel functions in Mie scattering calculations using continued fractions. Appl Optics 1976;15(3):668-71

[74] Li ZL, Achenbach JD, Kim JO Effect of elastic discontinuities on V(z) and V(z, x) for the line-focus acoustic microscope. Wave motion 1991;14:187-203

[75] Liang KK, Kino GS, Khuri-Yakub BT Material characterization by the inversion of V(z). IEEE Trans Son Ultrason 1985;32(2):213-24

[76] Liu GR, Achenbach JD, Kim JO, Li ZL A combined finite element method/boundary element method technique for V(z) curves of anisotropic-layer/substrate configurations. J Acoust Soc Am 1992;92(5):2734-40

[77] Linde A Dentin matrix proteins: Composition and possible functions in calcification. The Anatomical Record 1989; 224(2):154-166

[78] Lucas GL and Muir TG. The field of a focusing source. J Acoust Soc Am 1982;72(4):1289-96

[79] Miller JCP Bessel functions Part II, British Assn for the Adv. Sci, Mathematical Tables, Vol X Cambridge University Press 1952

[80] Maev RG, Denisova LA, Maeva EY , Denissov AA New data on histology and physico-mechanical properties of human tooth tissue obtained with acoustic microscopy. Ultrasound in Med & Biol, 2002; 28:131-136

[81] Manly RS, Deakins ML. Changes in the volume per cent of moisture, organic and inorganic material in dental caries. J Dent Res 1940;19(2):165-70

[82] Misra A, Spencer P, Marangos O, Wang Y, Katz JL Parametric study of the effect of phase anisotropy on the micromechanical behaviour of dentin-adhesive interfaces. J R Soc Interface 2005;2:145-57

[83] Marangos O, Misra A, Spencer P, Bohaty B, Katz JL Physico-mechanical properties determination using microscale homotopic measurements: Application to sound and caries-affected primary tooth dentin. Act Biomater 2009;5:1338-48

[84] Marshall GW, Marshall SJ, Kinney JH, Balooch M The dentin substrate: structure and properties related to bonding. J Dent 1997;25(6):441-58

[85] Marshall GW, Chang YJ, Saeki K, Gansky SA, Marshall SJ Citric acid etching of cervical sclerotic dentin lesions: An AFM study. J Biomed Mater Res A 2000;49(3):338–44

[86] Marshall GW, Chang YJ, Gansky SA, Marshall SJ Demineralization of caries-affected transparent dentin by citric acid: An atomic force microscopy study. Dental Mater 2001;17(1):45–52

[87] Nagy PB and Adler L Acoustic material signature from frequency analysis. J Appl Phys 1990;67(8): 3876-78

[88] Nagy PB and Adler LA Surface roughness induced attenuation of reflected and transmitted ultrasonic waves. J Acoust Soc Am 1987;82(1):193-97

[89] Nakabayashi N, Kojima K, Masuhara E The promotion of adhesion by the infiltration of monomers into tooth substances. J Biomed Mater Res 1982;16:265-73

[90] Nakabayashi N, Ashizawa M, Nakamura M Identification of a resin-dentin hybrid layer in vital human dentin created *in vivo*: durable bonding to vital dentin. Quint Int 1992;23:135-141

[91] Oliveira SSA, Hilton JF, Marshall SJ, Marshall GW Etching kinetics of a self-etching primer. Biomaterials 2003; 23:4105–112

[92] O'Neil HT. Theory of focusing radiators. J Acoust Soc Am 1949;21(5):516-26

[93] Ophir J and Jaeger P Spectral shifts of ultrasonic propagation through media with nonlinear dispersive attenuation. Ultrasonic Imaging 1982;4:282-89

[94] Orofino DP and Pedersen PC Efficient angular spectrum decomposition of acoustic sources – Part I: Theory. IEEE Trans Ultrason Ferroelect Freq Contr 1993(3):238-49

[95] Pashley DH, Ciucchi B, Sano H, Horner JA Permeability of dentin to adhesive resins. Quintessence Int 1993; 24:618-31

[96] Pashley DH, Kelli AA, Wataha JC, Rueggeberg F, Ceballos L, Itou K, Yoshiyama M, Carvalho RM, Tay FR Viscoelastic properties of demineralized dentin matrix. Dent Mater 2003;19:700-6

[97] Peck SD and Briggs GAD The caries lesion under the scanning acoustic microscope. Adv Dent Res 1987;1(1):50-63

[98] Peck SD, Rowe JM, Briggs GAD Studies on sound and carious enamel with the quantitative acoustic microscope. J Dent Res 1989;68(2):107-12

[99] Pecorari C and Briggs GAD Acoustic microscopy and dispersion of leaky Rayleigh waves on randomly rough surfaces: a theoretical study. IEEE Trans Ultrason Ferroelect Freq Contr 1996;43(3):428-33

[100] Prasad M. Mapping impedance microstructures in rocks with acoustic microscopy. The Leading Edge 2001;20(2):172-79

[101] Press WH, Flannery BP, Teukolsky SA, Vetterling WT Numerical recipes: The art of scientific computing New York: Cambridge University Press 1988

[102] Raum K, Jenderka KV, Klemenz A, Brandt J. Multilayer analysis: quantitative scanning acoustic microscopy for tissue characterization at a microscopic scale. IEEE Trans Ultrason Ferroelect Freq Contr 2003;50(5):507-16

[103] Raum K, Leguerney I, Chandelier F, Talmant M, Saïed A, Peyrin F, Laugier P. Site-matched assessment of structural and tissue properties of cortical bone using scanning acoustic microscopy and synchrotron radiation μCT. Phys Med Biol 2006;51(3):733-46

[104] Raum K, Cleveland R O, Peyrin F, Laugier P. Derivation of elastic stiffness from site-matched mineral density and acoustic impedance maps. Phys Med Biol 2006;51(3):747-58

[105] Raum K, Kempf K, Hein HJ, Schubert J, Maurer P. Preservation of microelastic properties of dentin and tooth enamel in vitro – A scanning acoustic microscopy study. Dent Mater 2007; 23:1221-28

[106] Rayleigh JWS The theory of sound II. Dover: New York 1945

[107] Rebinsky DA and Harris JG An asymptotic calculation of the acoustic signature of a cracked surface for the line focus scanning acoustic microscope. Proc R Soc Lond A 1992;436:251-65

[108] Rebinsky DA and Harris JG The acoustic signature for a surface-breaking crack produced by a point focus scanning acoustic microscope. Proc R Soc Lond A 1992;438:47-65

[109] Robins AJ Reflection of plane acoustic waves from a layer of varying density. J Acoust Soc Am 1990;87(4):1546-52

[110] Robins AJ Plane-wave reflection from a solid layer with nonuniform density, sound speed, and shear speed. J Acoust Soc Am 1998;103(3):1337-45

[111] Rokhlin SI and Wang L Stable recursive algorithm for elastic wave propagation in layered anisotropic media: Stiffness matrix method. J Acoust Soc Am 2002;112(3):822-34

[112] Rosales JI, Marshall GW, Marshall SJ, Watanabe LG, Toledano M, Cabrerizo MA, Osorio R Acid-etching and hydration influence on dentin roughness and wettability. J Dent Res 1999; 78(9):1554-59

[113] Santini A, Miletic V. Quantitative micro-Raman assessment of dentine demineralization, adhesive penetration, and degree of conversion of three dentine bonding systems. Eur J Oral Sci 2008; I 16: 177-83

[114] Sapozhnikov O and Sinilo Acoustic field produced by a concave radiating surface with allowance for the diffraction. Acoust Phys 2002;48(6):813-21

[115] Schmidt H Numerically stable global matrix approach to radiation and scattering from spherically stratified shells. J Acoust Soc Am 1993;94(4):2420-30

[116] Somekh MG, Briggs GAD Ilett C The effect of elastic anisotropy on contrast in the scanning acoustic microscope. Phil Mag A 1984;49(2):179-204

[117] Sommerfeld A Optics New York:Academic Press 1954

[118] Spencer P and Swafford JR Unprotected protein at the dentin/adhesive interface Quintessence Int 1999;30:501-507

[119] Spencer P, Wang Y, Walker MP, Wieliczka DM, Swafford JR Interfacial chemistry of the dentin/adhesive bond J Dent Res 2000;79(7):1458-63

[120] Stamnes JJ Waves in focal regions. Bristol: Adam Hilger 1986

[121] Sumikawa DA, Marshall GW, Gee L, Marshall SJ. Microstructure of primary tooth dentin. Pediatr Dent 1999;21(7):439-44

[122] Susin AH, Alves LS, De Melo GP, Lenzi TL. Comparative scanning electron microscopic study of the effect of different dental conditioners on dentin micromorphology. J Appl Oral Sci 2008;16(2): 100-5

[123] Suzuki M, Kato H, Wakumoto S (1991). Vibrational analysis by Raman spectroscopy of the interface between dental adhesive resin and dentin. J Dent Res 1991;70:1092-1097

[124] Taylor JR An introduction to error analysis Sausalito: University Science 1997.

[125] Tesch W, Eidelman N, Roschger P, Goldenberg F, Klaushofer K, Fratzl P Graded microstructure and mechanical properties of human crown dentin. Calcif Tissue Int 2001;69(3):147-57

[126] Thompson IJ and Barnett AR Coulomb and Bessel functions of complex arguments and order. J Comp Phys 1986;64:490-509

[127] Thomson WT J Transmission of elastic waves through a stratified solid medium. Appl Phys 1950; 21(89):89-93

[128] Toledano M, Osorio R, Perdigao J, Rosales JI, Thompson JY, Cabrerizo-Vilchez MA Effect of acid etching and collagen removal on dentin wettability and roughness. J Biomed Mater Res 1999;47:198-203

[129] Turner CH, Rho J, Takano Y, Ting YT, Pharr GM The elastic properties of the trabecular and cortical bone are similar: results from two microscopic measurement techniques. J Biomech 1999;32(4):437-41

[130] Van Meerbeek B, Dhem A, Goret-Nicaise M, Braem M, Lambrechts P, Vanherle G. Comparative SEM and TEM examination of the ultrastructure of the resin-dentin interdiffusion zone. J Dent Res 1993;72(2):495-501

[131] Vollmann J, Profunser DM, Bryner J, Dual J Elastodynamic wave propagation in graded materials: Simulations, experiments, phenomena, and applications Ultrasonics 2006;44:1215-21

[132] Wang L, Rokhlin SI Stable reformulation of transfer matrix method for wave propagation in layered anisotropic media. Ultrasonics 2001;39(6):413-24

[133] Wang L, Rokhlin SI Recursive geometric integrators for wave propagation in a functionally graded multilayered elastic medium. J Mech Phys Solids 2004;52:2473-506

[134] Wang R, Weiner S Human root dentin: structure anisotropy and Vickers microhardness isotropy. Connect Tissue Res 1998;39(4):269-279

[135] Wang Y and Spencer P Hybridization efficiency of the adhesive/dentin interface with wet bonding. J Dent Res 2003 82(2):141-5

[136] Wang Y, Spencer P Effect of acid etching time and technique on interfacial characteristics of the adhesive-dentin bond using differential staining. Eur J Oral Sci 2004;112: 293-99

[137] Weiner S, Veis A, Beniash E, Arad T, Dillon JW, Sabsay B, Siddiqui F Peritubular dentin formation: crystal organization and the macromolecular constituents in human teeth. J Struct Biol 1999;126(1):27-41

[138] Wickramasinghe HK Contrast and imaging performance in the scanning acoustic microscope. J Appl Phys 1979;50(2):664-72

[139] Wieliczka DM, Kruger MB, Spencer P Raman imaging of dental adhesive diffusion. Appl Spetcrosc 1997; 51(11):1593-96

[140] Williams EG Fourier acoustics: Sound radiation and nearfield acoustic holography. London: Academic 1999

[141] Winkler JR, Davies JB Accurate field analysis of the propagation of elastic waves through an acoustic microscope, Part I: Theory. IEEE Trans Ultrason Ferroelect Freq Contr 1986;33(6):644-56

[142] Winkler JR, Davies JB Accurate field analysis of the propagation of elastic waves through an acoustic microscope, Part II: Results. IEEE Trans Ultrason Ferroelect Freq Contr 1986;33(6):657-68

[143] Zhang Z, Paulino GH Wave propagation and dynamic analysis of smoothly graded heterogeneous continua using graded finite elements. Int J Solids Struct 2007;44:3601-26

[144] Zheng YP , Maev EY , Denisov AA , Maev RG Ultrasound imaging of human teeth using a desktop scanning acoustic microscope. Acoustical Imaging 2000;24:165-71

[145] Zinin P, Lefeuvre O, Briggs A, Zeller BD, Cawley P, Kinloch A, Zhou X, Thompson G Determination of density and elastic constants of a thin phosphoric acid-anodized oxide film by acoustic microscopy. J Acoust Soc Am 1999;106(5):2560-7